UNIVERSITAT DE BARCELONA

Assessment of the lipidomic effects of environmental pollutants on exposed organisms using chemometric and analytical methods

Eva Gorrochategui Matas

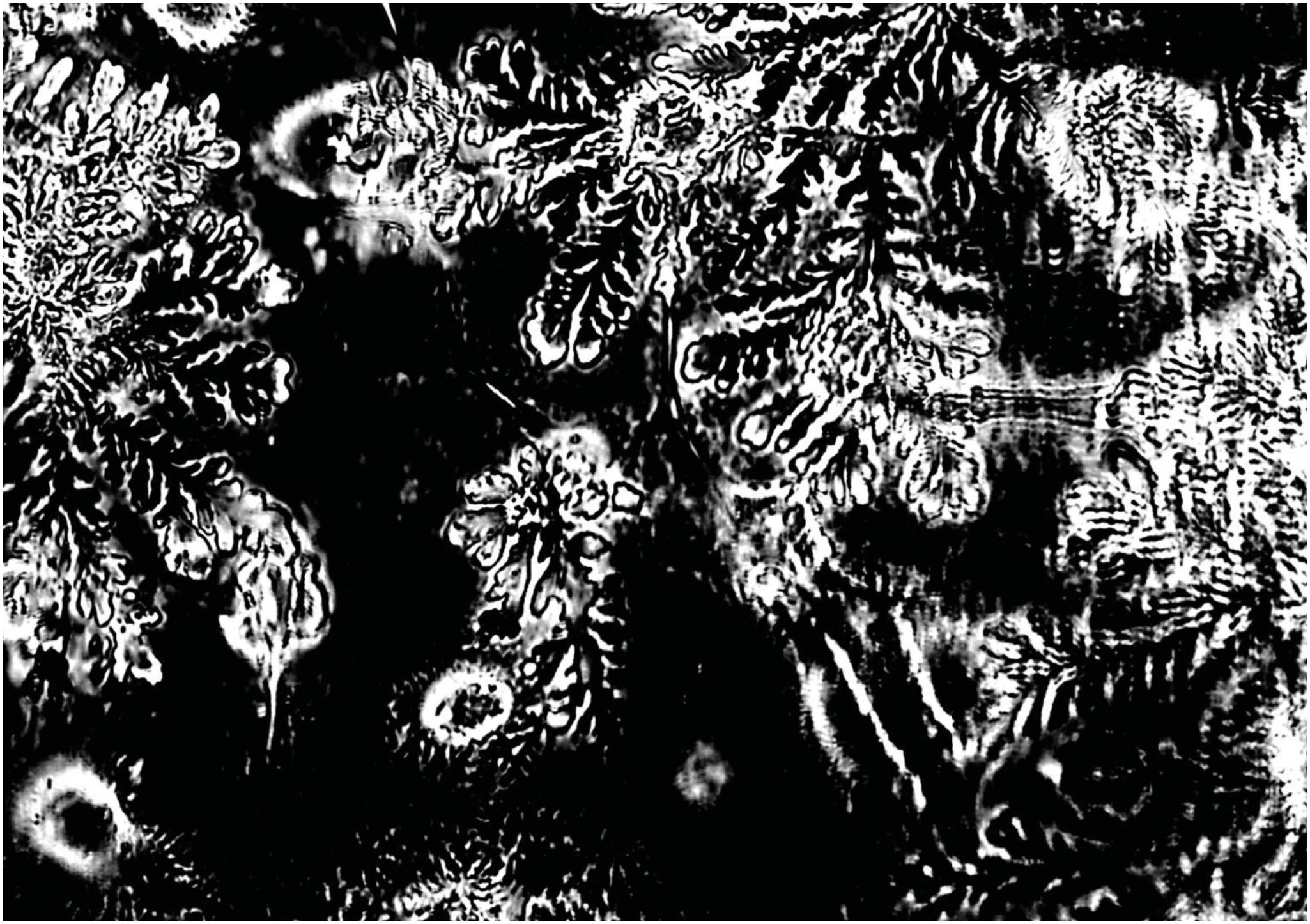

CHAPTER 4

IR, Raman and MS combined with chemometrics for environmental omic assessment

CHAPTER 4

Assessing the effects of pollutants in the environment is one of the main goals of environmental metabolomics (and lipidomics). To simulate the effects on environmental ecosystems, some animal models can be used. In this Thesis, the *Xenopus laevis* A6 kidney epithelial cell line was utilized to simulate the effects of four PFASs (*i.e.*, PFBS, PFOA, PFOS and PFNA) on amphibians. Also, zebrafish (*Danio rerio*) was used as a model organism to simulate the effects of four CBNs (*i.e.*, C_{60}, SWCNT, short-MWCNT and long-MWCNT) on fish. In order to perform such studies, two analytical techniques (*i.e.*, ATR-FTIR and LC-MS) combined with chemometric tools were used.

This Chapter of the Thesis is structured in the following manner: an introduction section, a scientific research section including the scientific articles containing *lipidomic and metabolomics data obtained from experiments performed with environmental model-biosystems exposed to chemical pollutants*, a discussion section and some specific conclusions.

4.1. INTRODUCTION

The study of organism-environment interactions is of vital importance and appears as the main goal of *environmental metabolomics*[486] (and lipidomics) field. Recently, the number of examples of the application of omics data in the context of ecological risk assessment has significantly grown.

Moreover, some of these omic datasets (including transcriptomics, metabolomics, lipidomics and proteomics) have been used in the development of adverse outcome pathways (AOP) frameworks[487]. The coordinated application of omics data and the AOP framework has successfully derived computational models that can support risk assessment, replacing other traditional approaches. However, the application of omics data in AOP framework has still three main challenges, as reported in the study of Brockmeier, E.K. *et al*.[488] : i) the need for a cohesive experimental design approach for favourably identifying relevant key events (KEs), ii) the integration of a framework for interpreting omics data to identify genes and pathways that are related to KEs and illustrative of a pathway or mode of action[489], and iii) the necessity of improved interpretation of the causal linkages among chemically induced molecular-level alterations to physiological and higher-level effects. In fact, in order for omics to have a future within risk assessment, the degree of uncertainty generated from omic data sets needs to be proved as a reasonable level for risk assessment applications[490].

In this Thesis, the study of the interaction of environment and organisms was focused on the evaluation of the effects that some chemical pollutants widely distributed in the environment can pose on two groups of vertebrate organisms: amphibians and fish. In order to simulate the effects on these two groups of animals, two model-biosystems were specifically chosen. On the one hand, the model biosystem selected to simulate effects on amphibians was the *Xenopus laevis* A6 kidney epithelial cell line. On the other hand, the model biosystem chosen to reproduce effects on fish was zebrafish (*Danio rerio*).

Xenopus laevis A6 kidney epithelial cells: model biosystem to simulate effects on amphibians

The A6 cell line is an epithelial cell line from a distal part of a nephron. Originally, the cell line was derived from African clawed frog *Xenopus laevis*, but it has been shown to display structural and functional properties of mammalian distal epithelium cells[491]. In FIGURE 4.1., five pictures of A6 cells experimentally obtained in this Thesis when using scanning electron microscopy (SEM) are presented. In the five figures, the characteristic architecture of A6 cells forming monolayers is shown. The A6 cell line exhibits contact inhibition of cell division, since further cell division stops after a confluent monolayer is formed. This cell line has a doubling time of around 20 hours. Dividing A6 cells usually have a fibroblast-like shape with characteristic membrane extensions. Another clearly visible characteristic of proliferating A6 cells is the presence of two or more light dots. These dots are not observed in confluent cell layer and are represented in FIGURE 4.2.

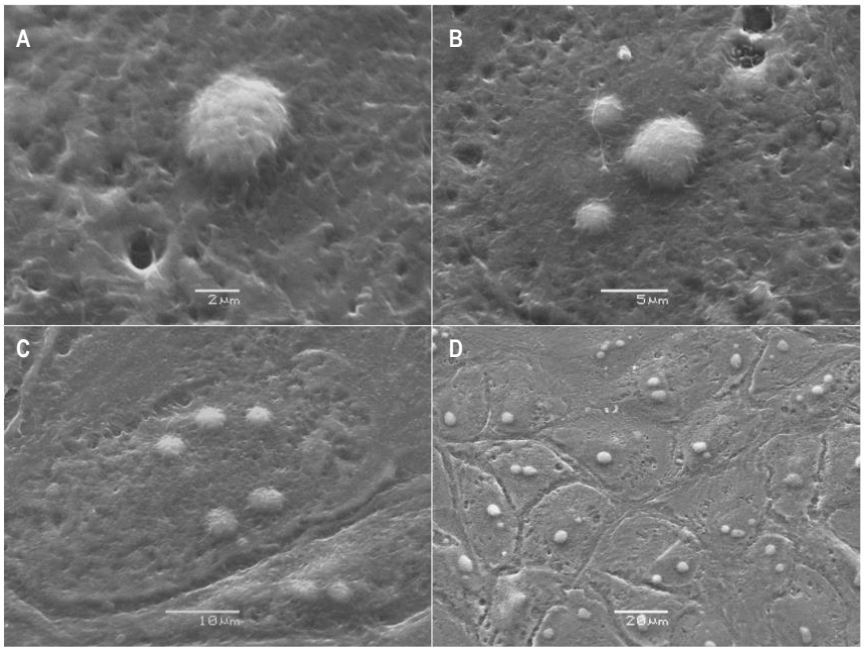

FIGURE 4.1

Scanning electron micrographs of *Xenopus laevis* A6 kidney epithelial cells. A) Scale bar= 2 µm; B) Scale bar= 5 µm; C) Scale bar= 10 µm and D) Scale bar= 20 µm. SEM equipment was a JEOL 5600 scanning electron microscope (JEOL, Tokyo, Japan).

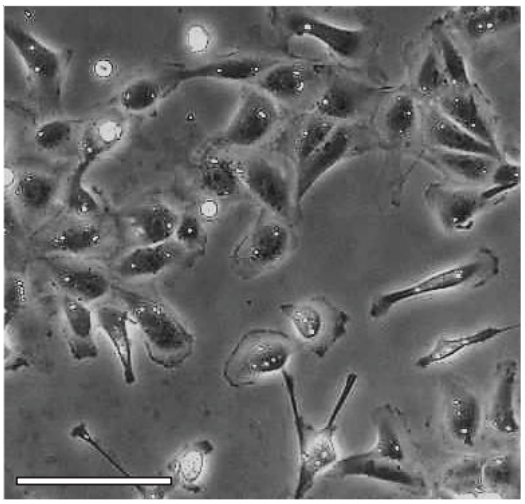

FIGURE 4.2

Phase contrast image of proliferating A6 cells with particular membrane extensions and light dots, indicating cell division. (Scale bar= 150 μM). Image obtained with Leica DMIRE2 inverted microscope, connected to a Leica TCS SP2 scan head.

In a confluent A6 cell monolayer, cells form tight junctions. The cellular membrane facing the culture media is referred to as the apical membrane. The membrane turned towards the bottom of the plastic culture flask is referred to as basal membrane. Differentiated A6 cells transport Na^+ and Cl^- ions across the membrane through ion channels. Active transport of Na^+ ions across the epithelium monolayer and subsequent diffusion of Cl^- ions results in water inflow into the area between the basal membrane and the culture flask. This process leads to an elevation of the cell layer and to the formation of *domes* which can be clearly seen through a light microscope, as observed in the images obtained in this Thesis (**FIGURE 4.3**).

The formation of domes is regarded as a sign of active transport processes and an intact epithelial barrier function due to functional tight junctional cell-cell contacts[492]. Since epithelial tissue is involved in the performance of many organs (in the case of A6 cells, the kidney), the presence of dome structures may have an influence on their performance. Moreover, dome structures show enhanced cell excretion function compared to cells forming monolayers. Thus, differential effects of environmental pollutants depending on cell status (*i.e.*, monolayers *versus* domes) may be expected, which offers high possibilities of study.

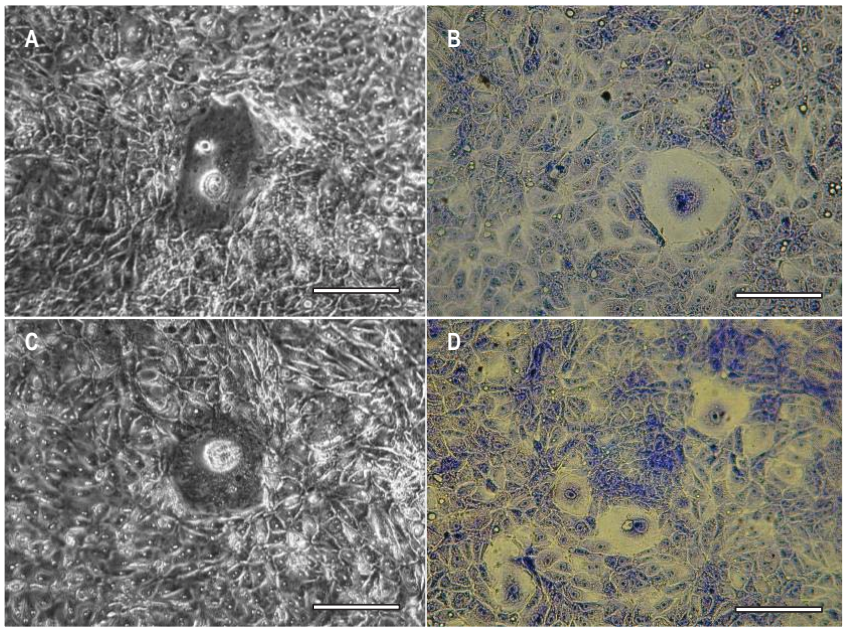

FIGURE 4.3

A6 cells forming domes. A and C) Direct inversion images of Giemsa-stained A6 cells using a Nikon Coolpix MCD lens 0.82-0.29X adapter to a Nikon Eclipse TE300 inverted microscope; B and D) Phase-contrast images of A6 cells using a Leica DMIRE2 inverted microscope, connected to a Leica TCS SP2 scan head. (Scale bars= 150 µm).

Another typical structure formed by A6 cells in a confluent monolayer is the elevated areas, which have a tube-like structure. These structures are referred to as "balloons". As many other epithelial cells, the A6 cells are covered with a cell coat, or glycoalyx, consistent of carbohydrates (mainly oligosaccharides) bound to the lipids and proteins of the membrane of cells. Sialic acid can be added to the oligosaccharide chains, giving them a negative charge. The role of this cell coat is to protect the cells against physical and chemical injuries, as well as enabling the cells avoid any undesirable protein-protein interactions[493]. *Xenopus laevis* A6 kidney epithelial cells, apart from providing an interesting topic of research due to the fact that they can form dome structures, they constitute a useful model to study the effects that environmental contaminants can have on lipids. This is special important, not only because the previously reported capacity of PFASs to disrupt lipid metabolism, but also due to the link that exists between kidney disorders and lipid accumulation. A search in the literature shows

that lipid accumulation in non-adipose tissues is increasingly recognised to contribute to organ injury through a process termed lipotoxicity. In fact, suggesting that renal lipid accumulation and lipotoxicity may lead to kidney dysfunction has mounted significantly over years[494]. Abnormal renal lipid content has been described in a number of animal models and has been successfully manipulated using pharmacologic or genetic strategies. There is some heterogeneity among studies with regard to the mechanisms, consequences, and localization of lipid accumulation in the kidney, explainable at least in part by inherent differences between animal models. The relevance of these findings for human pathophysiology remains to be established. Moreover, current knowledge on renal lipid physiology and pathophysiology is insufficient, but provides a strong foundation and incentive for further exploration. In FIGURE 4.4., four pictures obtained in this Thesis evidence that A6 cells can form lipid droplets in their structures, represented with green colour in the figure.

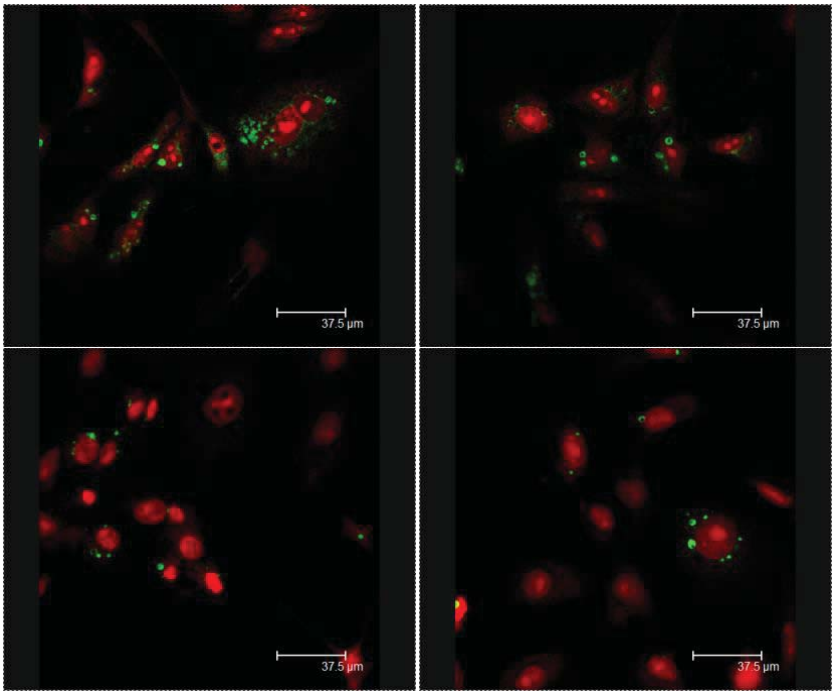

FIGURE 4.4

A6 cells forming lipid droplets (in green). Images correspond to stained A6 cells with BODIPY and are obtained using a Leica DMIRE2 inverted microscope, connected to a Leica TCS SP2 scan head and phase contrast settings. (Scale bars= 37.5 µm).

Zebrafish (*Danio rerio*): model organism to simulate effects on fish

Zebrafish (*Danio rerio*), a small tropical fish native to the rivers of India and South Asia[495], is considered one of the best-described and most attractive and popular vertebrate model species in developmental genetics, environmental risk assessment and (eco)toxicology. A number of unique features have contributed to its attraction, such as its fast development, easy maintenance in the laboratory, large number of offspring, transparency of embryos, access to experimental manipulation and possibility to perform with them small-scale and high-throughput analyses[495]. Moreover, beyond their application for determining the acute toxicity, fish embryos, which are representative species of freshwater fish, are also excellent models for studies aimed at the understanding of toxic mechanisms and the indication of possible adverse and long-term effects[495]. The basic body plan of zebrafish is laid out after 24 hpf (hours post-fertilisation) and embryos hatch approximately 2-3 dpf (days post-fertilization) (FIGURE 4.5). At 5 dpf- at the time of complete yolk consumption and start of external feeding- organogenesis of principal organs is fulfilled. The cycle of reproduction of zebrafish is very short since they are mature at the age of 3 months. Around 100 eggs can be spawned by one female per day, which can be then fertilised by sperm release of the male into the water. Under laboratory conditions several thousand embryos can simply be produced daily and used for parallel experimental treatments.

Thanks to the major similarities of vertebrates, the zebrafish is utilized as a model for human disease and development. As reported by the current European Union legislation for the protection of animals used for experimental and other scientific purposes, the use of embryonic stages of vertebrates is not controlled. Therefore, experiments with embryos are contemplated as substitutes to animal experiments. Moreover, in contrast to cellular fish cell lines the embryo model offers a complex, multicellular system integrating the interaction of various tissues and differentiation processes.

Despite the amount of genomic and transcriptomic data already available for zebrafish, few studies have used these laboratory-grown animals to perform metabolomic analyses. In fact, not until 2013, the ratio of scientific articles that used zebrafish for metabolomic purposes started exceeding fifty publications per year. The main drawback associated with the use of fish embryos for metabolomic purposes is the relative small size of zebrafish that requires the

use of highly sensitive methods such as NMR or LC-MS. However, important progresses are being made to cope with "size issues" causing that metabolomics is rapidly advancing for zebrafish.

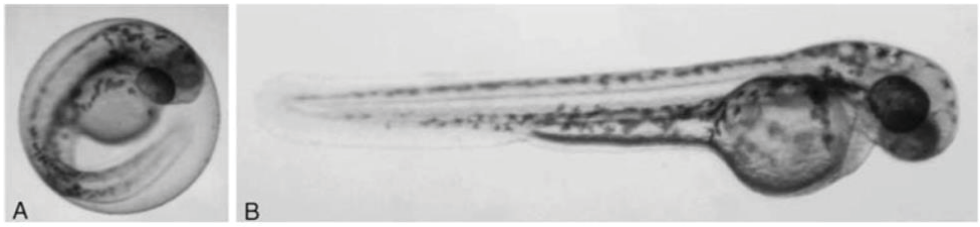

FIGURE 4.5

Image extracted from Figure 1 of the scientific article "The zebrafish embryo model in environmental risk assessment-applications beyond acute toxicity testing" published in Environ. Sci. Pollut. Res. (2008)[495]. In the figure, zebrafish embryos at 48 h post-fertilization (hpf) (A) and after manual removal of the chorion (B).

4.2. SCIENTIFIC RESEARCH

The effects of the four PFASs (*i.e.*, PFBS, PFOA, PFOS and PFNA) were assessed on *Xenopus laevis* A6 kidney epithelial cells, in two cell-differentiation states: monolayers versus dome structures. This study was performed using ATR-FTIR spectroscopy followed by chemometric analysis. The results of this research are included in the scientific article entitled "Perfluoroalkylated Substance Effects in *Xenopus laevis* A6 Kidney Epithelial Cells Determined by ATR-FTIR Spectroscopy and Chemometric Analysis" (Section 4.2.1). To continue with the evaluation of the effects of pollutants on the environment, further assessment of the effects of four CBNs (*i.e.*, C_{60}, SWCNT, short-MWCNT and long-MWCNT) on zebrafish (*Danio rerio*) was performed. Moreover, the effects of CBNs were determined in brain, gonads and intestinal tissue samples of male and female zebrafish species. In this case the evaluations were performed using LC-MS, SERS and chemometric analysis. The results of the latter research are included in the scientific article entitled "Diet-sourced carbon-based nanoparticles induce lipid alterations in tissues of zebrafish (*Danio rerio*) with genomic hypermethylation changes in brain" (Section 4.2.2.).

4.2.1. SCIENTIFIC ARTICLE VIII

Perfluoroalkylated substance efects in Xenopus laevis A6 kidney epithelial cells determined by ATR-FTIR spectroscopy and chemometric analysis

E. Gorrochategui, S. Lacorte, R. Tauler, F.L. Martin

Chemical Research in Toxicology (2016) **29 (5)**, 924-932

Chemical Research in Toxicology

Article

pubs.acs.org/crt

Perfluoroalkylated Substance Effects in *Xenopus laevis* A6 Kidney Epithelial Cells Determined by ATR-FTIR Spectroscopy and Chemometric Analysis

Eva Gorrochategui,[†] Sílvia Lacorte,[†] Romà Tauler,[†] and Francis L. Martin*[,‡,§]

[†]Department of Environmental Chemistry, Institute of Environmental Assessment and Water Research (IDAEA), Consejo Superior de Investigaciones Científicas (CSIC), Barcelona 08034, Catalonia, Spain

[‡]Centre for Biophotonics, Lancaster Environment Centre, Lancaster University, Lancaster LA1 4YQ, U.K.

[§]School of Pharmacy and Biomedical Sciences, University of Central Lancashire, Preston, U.K.

Supporting Information

ABSTRACT: The effects of four perfluoroalkylated substances (PFASs), namely, perfluorobutanesulfonate (PFBS), perfluorooctanoic acid (PFOA), perfluorooctanesulfonate (PFOS), and perfluorononanoic acid (PFNA) were assessed in *Xenopus laevis* A6 kidney epithelial cells by attenuated total reflection Fourier-transform infrared (ATR-FTIR) spectroscopy and chemometric analysis. Principal component analysis−linear discriminant analysis (PCA-LDA) was used to visualize wavenumber-related alterations and ANOVA-simultaneous component analysis (ASCA) allowed data processing considering the underlying experimental design. Both analyses evidenced a higher impact of low-dose PFAS-treatments (10^{-9} M) on A6 cells forming monolayers, while there was a larger influence of high-dose PFAS-treatments (10^{-5} M) on A6 cells differentiated into dome structures. The observed dose−response PFAS-induced effects were to some extent related to their cytotoxicity: the EC_{50}-values of most influential PFAS-treatments increased (PFOS < PFNA < PFOA ≪ PFBS), and higher-doses of these chemicals induced a larger impact. Major spectral alterations were mainly attributed to DNA/RNA, secondary protein structure, lipids, and fatty acids. Finally, PFOS and PFOA caused a decrease in A6 cell numbers compared to controls, whereas PFBS and PFNA did not significantly change cell population levels. Overall, this work highlights the ability of PFASs to alter A6 cells, whether forming monolayers or differentiated into dome structures, and the potential of PFOS and PFOA to induce cell death.

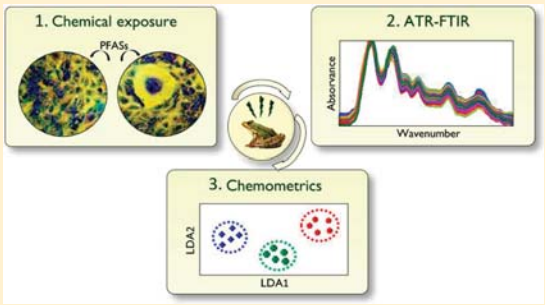

1. INTRODUCTION

Omic tools enable simultaneous and large-scale study of molecules of exposed organisms to extract underlying alterations caused by environmental stressors. State-of-the-art omic techniques include microarray-based and sequencing techniques,[1] nuclear magnetic resonance spectroscopy,[2] and mass spectrometry.[3] However, another technique valid for omics, providing rapid and nondestructive analyses, is IR spectroscopy.[4] Over the last few decades, IR has become a powerful methodology to study agriculture-related products and plant materials.[5−7] Recently, IR has provided excellent results both in clinical research [e.g., discriminating benign from malignant tumors in tissue samples such as the breast,[8] colon,[9] lung,[10] or prostate,[11] and examining biofluids, including urine, saliva, serum, or whole blood][12−14] and in the environmental field.[15−18] Because of its capacity to interrogate biochemical signals of stressed organisms, attenuated total reflection Fourier-transform IR (ATR-FTIR) spectroscopy shows great potential.

The use of ATR-FTIR spectroscopy to address biological questions is viable since biomolecules with chemical bonds having an electric dipole moment absorb in the mid-IR region through their vibrations, giving rise to a detailed biomolecular fingerprint in the form of an IR spectrum. The acquisition of such fingerprints allows subsequent spectral classification with computational methods and possibly permits biomarker detection.[19,20] Various chemometric methods are suitable for IR data sets, both for exploratory or modeling purposes, including principal component analysis (PCA) and linear discriminant analysis (LDA).[16,21,22] These methods allow data reduction to facilitate the identification of wavenumber-related spectral alterations associated with glycogen content, lipid content, conformational changes and phosphorylation characteristics in proteins or structural alterations in DNA/RNA.[23,24] Another chemometric technique suited for the analysis of IR data sets, especially for those obtained in multifactorial designs,

Received: March 4, 2016

DOI: 10.1021/acs.chemrestox.6b00076
Chem. Res. Toxicol. XXXX, XXX, XXX−XXX

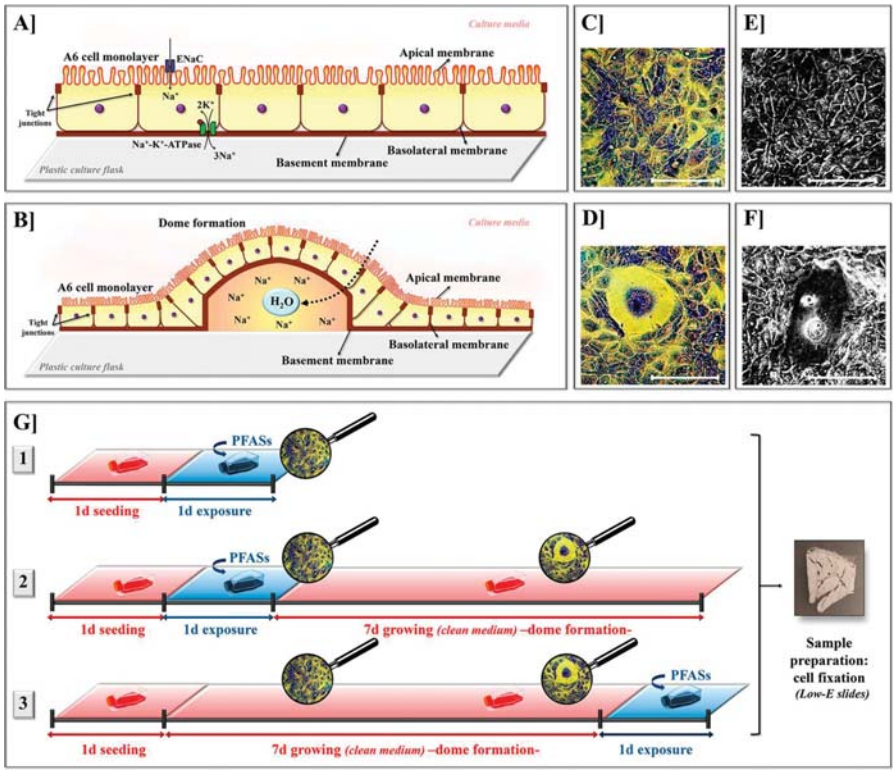

Figure 1. Schematic representation of *Xenopus laevis* A6 kidney epithelial cells forming a monolayer (A) and a dome (B). Direct inversion images of Giemsa-stained A6 cells disposed on a monolayer (C) and forming a dome (D). Phase-contrast images of A6 cells disposed on a monolayer (E) and forming a dome (F). (Scale bars = 150 μm). (G) Experimental design for the study of PFAS-induced effects (refer to section 2.3). (d = day).

such as that hereby presented, is ANOVA-simultaneous component analysis (ASCA).[25]

Omic experiments focused on molecules with high environmental persistence [e.g., perfluoroalkylated substances (PFASs)] permit the investigation of unknown effects of xenobiotics in target organisms. Preferred doses of exposure are usually in the nanomolar scale, so as to reproduce real-world low-doses. PFASs represent a large group of compounds highly used in a variety of consumer products, very resistant to degradation and with a high accumulation potential.[26,27] Concerns about PFASs have risen due to their widespread distribution and persistence in humans and the environment but also due to their toxicity and ability to act as endocrine-disrupting chemicals (EDCs)[28] and obesogens.[29] Some recent studies suggest a capacity of PFASs to alter cellular membrane lipids.[30−32] Other biosystems might be affected by the presence of PFASs, such as the A6 cell line.

The renal epithelial A6 cell line was produced in 1969 from the renal uriniferous tubule of the adult African clawed frog *Xenopus laevis*.[33] It expresses the properties of tight epithelium, renal distal tubules, and collecting ducts.[34] At confluence, A6 cells can form an epithelial monolayer (Figure 1A,C,E) and spontaneously differentiate into a dome structure (Figure 1B,D,F).[35] Renal epithelial cells are specialized for absorption or secretion, where the membrane facing the culture media is the apical membrane, the membrane attached to the plastic culture flask is the basement membrane, and the membrane lying along the basement surface is the basolateral membrane (Figure 1A,B). The apical membrane of A6 cells contains the epithelial Na^+ channel (ENaC), while Na^+/K^+-ATPase is in the basolateral membrane.[36] The incorporation of Na^+ ions by ENaC and their expulsion into the extracellular space by Na^+/K^+-ATPases causes an accumulation of Na^+ ions in the space between A6 cells and the plastic culture flask. Subsequent osmotic water inflow produces an elevation of the cell layer and results in a dome formation (Figure 1B),[37] a structure easily seen by the microscope (Figure 1D,F). A6 cells forming domes have distinct physiological and structural properties (e.g., changes in the cytoskeleton)[38] than A6 cells forming monolayers. Because it is easy to culture, the A6 cell line is commonly used in space studies, and several studies investigate the effects of gravitational forces on dome formation.[35,37,39] However, little research has been conducted into the effects of xenobiotics on A6 cells as a toxicological model to simulate the effects on amphibians.

Within this context, the aim of this study was to examine the alterations induced in A6 cells, forming monolayers or differentiated into domes, exposed to four PFAS substances [i.e., perfluorobutanesulfonate (PFBS), perfluorooctanesulfonate (PFOS), perfluorooctanoic acid (PFOA), and perfluorononanoic acid (PFNA)], using ATR-FTIR spectroscopy and chemometric analysis [i.e., PCA-LDA and ASCA; see Supporting Information (ESI) for a short description of these methods]. In addition, a growth-curve experiment was

DOI: 10.1021/acs.chemrestox.6b00076
Chem. Res. Toxicol. XXXX, XXX, XXX−XXX

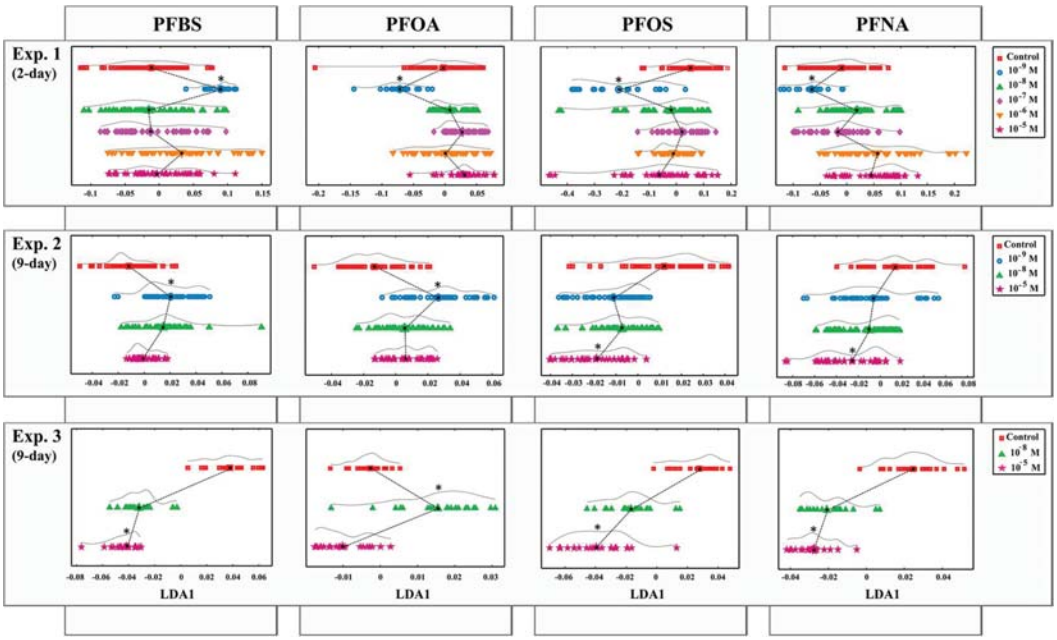

Figure 2. One-D PCA-LDA score plots showing dose−response effects of PFBS, PFOA, PFOS, and PFNA in the three experiments. *Most discriminant PFAS-treatment compared to the control.

developed to determine whether the four distinct PFAS-exposures differentially altered dose- and time-related cell number increases in culture.

2. MATERIALS AND METHODS

2.1. Chemicals and Reagents. PFBS and PFOS were obtained from Fluka (Austria), whereas PFOA and PFNA were purchased from Sigma-Aldrich (Steinheim, Germany). Stock standard solutions and serially diluted test solutions were prepared in DMSO. Cell culture consumables were obtained from Invitrogen Life Technologies (Paisley, UK), unless otherwise stated.

2.2. Cell Culture and Treatment. *Xenopus laevis* A6 kidney epithelial cells were obtained from American Type Culture Collection (ATCC CCL-102). They were cultured in modified L15 culture medium consisting of 70% Leibovitz media, 19% Milli-Q water sterile filtered through a 0.2 μM syringe filter, 10% fetal bovine serum (FBS), and 1% penicillin/streptomycin, at 5% CO_2 and 26 °C. Cells were trypsinized before the incorporation of cell aliquots for routine culture in T75 polystyrene flasks. Toward experiments, A6 cells were disaggregated, resuspended in complete medium, and then seeded in T25 flasks at a rate of 500,000 cells per flask whereupon they were grown for the time required depending on the experiment (see section 2.3). For PFAS-treatment, 25 μL of stock solutions were added to 5 mL of the culture medium so that final exposure-doses ranged from 0 to 10^{-5} M [considering 0 M as zero-dose control, in which cells were only exposed to the carrier solvent (DMSO)]. Following treatment, cells were disaggregated into cell suspensions and immediately fixed with 70% EtOH.

2.3. Experimental Design. The effects of the four PFAS substances were studied on A6 cells forming monolayers or domes in three distinct experiments [Figure 1G1,2,3]. In experiment 1 [Figure 1G1], PFAS-induced effects were evaluated in cells forming confluent monolayers. Toward this, cells were seeded for 1-day prior to PFAS-exposure for a further 1-day (2-day experiment) and final fixation. In this experiment, cells were exposed to chemicals at six concentrations (0, 10^{-9}, 10^{-8}, 10^{-7}, 10^{-6}, or 10^{-5} M). In experiments 2 and 3 [Figure 1G2,3, respectively], PFAS-effects were evaluated in cells forming domes (9-day experiment). However, the introduction of PFAS-treatment differed between them. In experiment 2 [Figure 1G2], following 1-day seeding and 1-day PFAS-exposure, the medium was aspirated and cells were grown for further 7 days in fresh medium, allowing dome formation, before final fixation. In contrast, in experiment 3 [Figure 1G3], cells were grown for 8 days to allow dome formation, followed by 1-day treatment exposure prior to fixation. In experiment 2, cells were PFAS-exposed at four concentrations (0, 10^{-9}, 10^{-8}, or 10^{-5} M), while in experiment 3, three concentrations (0, 10^{-8}, or 10^{-5} M) were tested.

Five independent experiments were performed for each treatment at conditions 1 and 2 (i.e., 5 samples per category). Thus, the total number of samples was 120 (i.e., 5 experiments × 4 PFASs × 6 doses) and 80 (i.e., 5 experiments × 4 PFASs × 4 doses) at conditions 1 and 2, respectively. In the third conditions, two independent experiments were performed, giving 2 samples per category. Hence, the total number of samples in the latter case was 24 (i.e., 2 experiments × 4 PFASs × 3 doses). Low number of replicates was performed in experiment 3, as the results obtained are used to extract tentative conclusions about long-term PFAS-induced effects considering the physiological conditions of cells forming domes.

2.4. ATR-FTIR Spectroscopy. Cellular material in 70% EtOH was applied to 1 cm × 1 cm Low-E-reflective glass microscope slides (Kevley Technologies, Chesterland, OH, USA) (Figure 1G) and allowed to air-dry prior to storage in marked 30 mm Petri dishes kept in a desiccated environment until analysis. IR spectra were obtained using a Bruker Vector 22 FTIR spectrometer with a Helios ATR attachment containing an ≈250 μm × 250 μm aperture diamond crystal (Bruker Optics Ltd., Coventry, UK). The ATR crystal was cleaned with sodium dodecyl sulfate (SDS; Sigma Chemical Co.); a new background was taken prior the analysis of each new sample. From each treatment flask (generating one slide), 10 IR spectra were acquired from different locations across each sample. The spectral resolution was 8 cm^{-1} giving data spacing of 4 cm^{-1}. Spectra were coadded for 32 scans; these were converted into absorbance units by Bruker OPUS software.

DOI: 10.1021/acs.chemrestox.6b00076
Chem. Res. Toxicol. XXXX, XXX, XXX−XXX

2.5. Spectral Preprocessing and Multivariate Data Analysis. Raw IR spectra obtained from exposed and control samples were preprocessed prior to chemometric analysis (see Figure S1). Initially, using OPUS software, IR spectra were individually cut to include only wavelengths between 1,800 and 900 cm^{-1} (235 wavenumbers at 4 cm^{-1} data spacing), the area associated with the biological spectral fingerprints. Then, the baseline of the resulting data set was corrected by applying Rubberband correction methods, and spectra were subsequently normalized to Amide I (i.e., 1,650 cm^{-1}). Afterward, spectra were mean-centered, and finally, the class of the sample was defined.

2.5.1. Principal Component Analysis Plus Linear Discriminant Analysis (PCA-LDA). PCA-LDA[15,16,21,22] was applied to the spectral data sets using MATLAB 8.3.0 R2014a (The Math Works, Natick, MA, USA) and the IrootLab toolbox (http://irootlab.googlecode.com).[40] As stated in the Theory section, PCA allows for the reduction of the number of variables in the spectral data set, whose small number of principal components (PCs) can capture 95% of the variance present in the original data set. In this study, the first 10 PCs were used. A total of 12 PCA-LDA analyses were performed, considering 4 PFASs and 3 experiments. For each model, the results of the analysis were visualized through one-dimensional (1-D) scores plots (Figure 2) and cluster vectors plots (see Figure S2). Scores plots were used to study dose−response effects of PFASs, by examining the proximity in multivariate distance between exposed and control samples. Primary wavenumbers important for such discrimination were visualized in cluster vectors plots.[22,24]

2.5.2. ANOVA-Simultaneous Component Analysis (ASCA). ASCA[25] (see ESI) was applied to three well-balanced spectral data sets (see Figure S3) by using PLS Toolbox 7.8 (eigenvector Research Inc., Wenatche, WA, USA) working in a MATLAB 8.3.0 R2014a environment (The Math Works, Natick, MA, USA). In these ASCA models, the effects of two categorical factors [i.e., type of chemical, with four levels (PFBS, PFOS, PFOA, or PFNA), and dose of exposure, with a number of levels differing among experiments (see section 2.3)] and interaction were studied. Statistical significances of the two factors and interaction were evaluated by a permutation test, using 10,000 permutations.[41]

2.6. Microscopic Images. *2.6.1. Cell Fixation.* A6 cells coming from 90% confluent T75 flasks were disaggregated, resuspended in complete medium, and seeded in plastic culture tissue coverslips (Sarstedt, USA) in 30 mm Petri dishes at a rate of 200,000 cells per Petri dish and allowed to attach overnight at 26 °C. Then, cells were grown for 2 days, when they formed a confluent monolayer, or for 9 days, when they formed domes. Finally, cells were fixed using 70% EtOH (40 min), washed twice with 70% EtOH, and kept at −4 °C until microscopy visualization.

2.6.2. Cell Staining. Cells fixed in the coverslips were air-dried for 24 h, transferred to new 30 mm Petri dishes containing 3 mL of a solution of 5% Giemsa (Sigma-Aldrich, UK), and left for 20 min. Then, the coverslips were washed twice with distilled water and allowed to air-dry. The coverslips were mounted directly onto the microscope.

2.6.3. Microscopy Instrumentation. A Nikon Coolpix 950 camera, mounted via a Nikon Coolpix MDC lens 0.82−0.29× adapter to a Nikon Eclipse TE300 inverted microscope, fitted with a Nikon Plan Apo 60×/1.20 water immersion objective was used to obtain images of Giemsa-stained cells (Figure 1C,D). Also, a confocal microscope, Leica DMIRE2 inverted microscope connected to a Leica TCS SP2 scan head and phase contrast settings, was used to obtain images of Figure 1E,F.

2.7. Determination of Cell Number. A6 cells were seeded at a ratio of 500,000 in T25 flasks in 5 mL of complete medium containing individual chemicals (PFBS, PFOS, PFOA, or PFNA) at concentrations of 10^{-9}, 10^{-5}, or 0 M (control). This point was taken as time zero (T_0), and duplicate cell counts in triplicate flasks were acquired. These T_0 cell counts (n = 6 per category) were averaged and normalized to 100%. Cells were washed, trypsinized, resuspended, and the cell number determined at indicated time points employing a hemocytometer. The acquired values for each experimental condition were averaged, and these contributed to the mean ± SD of the three separate experiments. Results were expressed as relative cell number [%; i.e., ratio of the cell number at the indicated time point relative to that determined at T_0 (normalized to 100%) × 100].

3. RESULTS

In the present study, IR data sets were first evaluated with 12 PCA-LDA models and further examined with 3 ASCA models. Initial PCA-LDA was performed to explore individual dose−response effects of each PFASs in the three experiments, whereas ASCA allowed data analysis considering the underlying experimental design. Results of both analyses are presented below.

3.1. Dose−Response Effects of Individual PFASs by PCA-LDA. Results of the 12 PCA-LDA (Figure 2) evidenced a distinct dose−response pattern in experiment 1 compared to experiments 2 and 3. In the first experiment, the highest distinction between treated and control cell populations was observed at the lowest concentration tested (10^{-9} M) in all PFAS-treatments. Conversely, higher PFAS concentrations were responsible for marked effects in experiments 2 and 3, especially in the latter conditions. A similar tendency was observed in the two last experiments: PFOS and PFNA caused in both conditions the highest alterations at 10^{-5} M, and PFOA produced the highest impact at low doses of 10^{-9} and 10^{-8} M in experiments 2 and 3, respectively. Only PFBS behaved inversely in these two experiments, producing major effects at the lowest dose tested (10^{-9} M) in experiment 2 and at the highest (10^{-5} M) in experiment 3. Primary wavenumbers important for discrimination of PFAS-treatments at the concentration producing more effects in the three experiments together with the molecular entities associated with them[42] are shown in Table S1 and can be visualized in the cluster vectors plots of Figure S2.

3.2. Assessment of the Effects of Experimental Factors by ASCA. *3.2.1. Split-Up of Variation.* A first impression of the amount of variation related to the design factors can be obtained by separating this variation into contributions from the different factors. In this study, the statistical significances of the two categorical factors (i.e., chemical and dose) and of their interaction were evaluated separately in the three experiments (Table 1). Results of this evaluation were attributed to the dominant part of variation to

Table 1. ASCA Modeling: Significance and Partitioning of the Total Variance into the Individual Terms Corresponding to Factors and Interaction[a]

experiment	factor	percentage of variation[b]	significance (p-value)
1	C	2	1×10^{-3}
	D	3	1×10^{-3}
	$C \times D$	7	1×10^{-3}
	residuals	89	
2	C	2	4×10^{-3}
	D	3	1×10^{-3}
	$C \times D$	3	3×10^{-1}
	residuals	93	
3	C	8	3×10^{-1}
	D	8	8×10^{-2}
	$C \times D$	12	8×10^{-2}
	residuals	85	

[a] C = chemical; D = dose. [b] Percentage of variation expressed as sums of squared deviations from the overall mean and not variances.

DOI: 10.1021/acs.chemrestox.6b00076
Chem. Res. Toxicol. XXXX, XXX, XXX−XXX

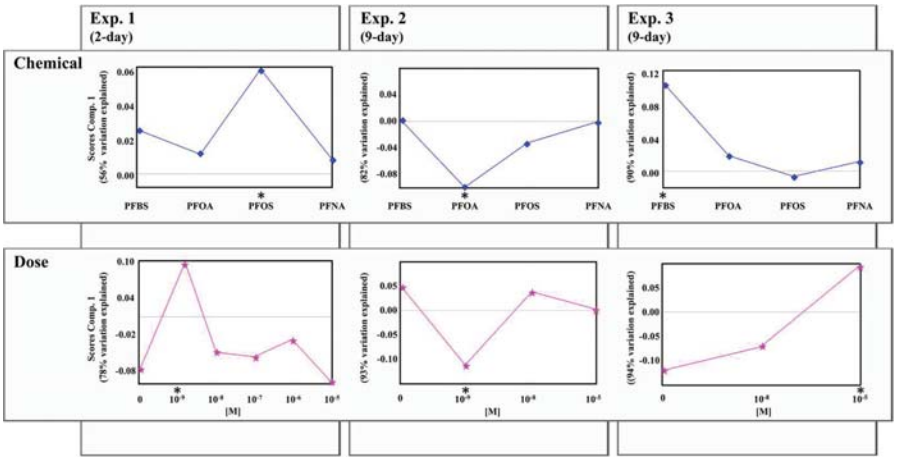

Figure 3. ASCA score plots of the first component for the factors "chemical" and "dose" of the three experiments. *Most discriminant factor levels.

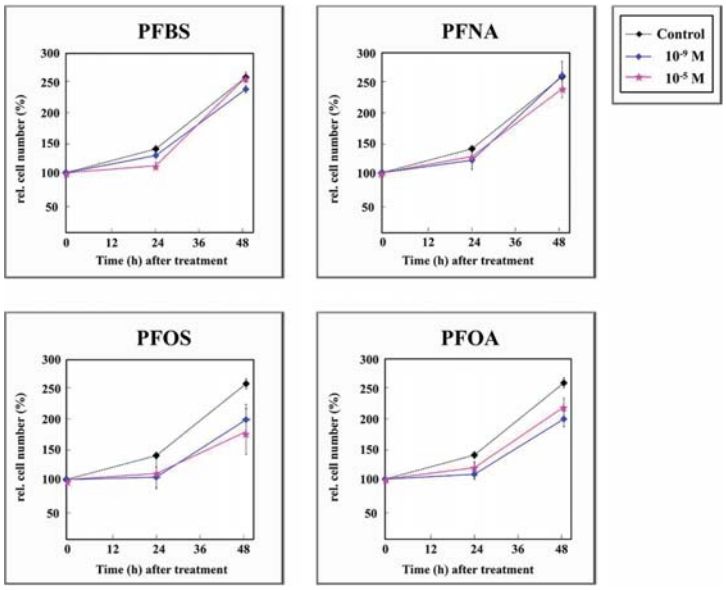

Figure 4. Effects of PFBS, PFNA, PFOS, and PFOA on dose- and time-related cell number increases in culture.

natural variability (residuals ≥85%) and the minor part to factors and interaction (≤12%), observing higher effects in experiment 3. Results of the permutation test showed larger significances (p-values ≤0.05) of factors in experiments 1 and 2. Despite the observed small PFAS-induced effects on A6 cells, the good reproducibility of the ATR-FTIR technique allows the extraction of reliable conclusions about their impact on A6 cells in the present study.

3.2.2. Factor "Chemical". Scores of the first component of factor "chemical" [T_c values of equation S2] shown in Figure 3 indicate that chemicals producing more effects were PFOS, PFOA, and PFBS in experiments 1, 2, and 3, respectively. For data sets 1, 2, and 3, the first component explains 56%, 82%, and 90% of variation, respectively. Factor "chemical" was significant in experiments 1 and 2 (p-values of 1×10^{-3} and 4×10^{-3}, respectively) but not significant in experiment 3 (p-value = 3×10^{-1}), according to the permutation test (Table 1).

3.2.3. Factor "Dose". Scores of the first component of factor "dose" are shown in Figure 3 for data sets acquired in experiments 1, 2, and 3, respectively [T_d values of equation S2]. For data sets 1, 2, and 3, the first component explains 78%, 93%, and 94% of variation, respectively. Scores of these figures indicate that concentrations of exposure producing more effects were 10^{-9}, 10^{-9}, and 10^{-5} M in experiments 1, 2, and 3, respectively. The results of the permutation test evidenced that the PFAS-dose was significant in experiments 1 and 2 with p-values of 1×10^{-3} and 1×10^{-3}, respectively, but not significant in experiment 3, with a p-value of 8×10^{-2} (Table 1).

3.2.4. Interaction "Chemical × Dose". Scores of the first component of the interaction showed no pattern related to the

DOI: 10.1021/acs.chemrestox.6b00076
Chem. Res. Toxicol. XXXX, XXX, XXX−XXX

interaction of factors: there was no increasing or decreasing trend of scores of the different doses of exposure respect to the chemical treatment. For this reason, the plot of these scores is not provided in this study.

3.3. Cell Number with Time in Culture with Exposure to PFASs. The effects of the four PFASs on the increases in A6 cell number are shown in Figure 4. The behavior observed was similar between pairs of chemicals PFBS and PFNA vs PFOS and PFOA. For the first two chemicals, following 24-h or 48-h treatment, no marked differences in cell population were observed with respect to the control. However, 24-h and 48-h treatments with PFOS and PFOA caused a significant decrease in cell number, which became higher with time and gave rise to maximum cell depletion after 48 h of exposure.

4. DISCUSSION

Our study evidenced a primary effect of low-dose (10^{-9} M) PFAS-treatment on A6 cells forming monolayers (experiment 1) (Figure 2). Predominant effects of environmental stressors at low-doses of exposure have often been reported in the literature,[43−46] especially for EDCs, such as PFASs. A review by Vandenberg et al.[47] reported two concepts associated with EDCs: first, "big effects at low doses", a theory primarily defined by the National Toxicology Program (http://ntp.niehs.nih.gov/), and second, the "nonmonotonicity" (i.e., nonlinear relationship between dose and effect) thus declaring the dogma "the dose makes the poison" open to question. It is important to stress that our findings in experiment 1 (cells forming a monolayer) followed this low-dose theory, while results of experiments 2 and 3 (cells differentiated into dome structures) showed an opposing tendency (major alterations at high doses). Such differences can be explained by the specific physiological status of cells forming monolayers or domes, the latter having enhanced cell excretion function and requiring higher PFAS-doses to produce an effect. Also, the differential dose−response effects of PFAS substances depending on cell differentiation status were to some extent related to the cytotoxicity of most influential chemicals (according to ASCA results) in each experiment. Considering the median effective doses (EC_{50}) of PFASs reported in a previous study on JEG-3 cells[30] [i.e., PFOS (107−125 μM) < PFNA (213−220 μM) < PFOA (594−647 μM) ≪ PFBS (n.d.)], it was observed that major effects in experiment 1 (primarily influenced by high-cytotoxic PFOS) occurred at low doses, whereas larger effects in experiments 2 and 3 (primarily influenced by less-cytotoxic PFOA and PFBS, respectively) were observed at higher doses. Considering overall effects, a greater impact of PFAS substances was evident in experiment 3, presenting the treated samples to maximum cluster segregation compared to that of the control in 1-D PCA-LDA score plots (Figure 2). The higher effects of PFAS substances in experiment 3 vs experiment 2 might be attributed to a cellular recuperation after the chemical stress possible in the second conditions since cells were allowed to grow for 7 days in fresh medium after PFAS-exposure, a time that cells might use to eliminate those PFAS substances previously incorporated.[48]

Interestingly, distinct spectral alterations were induced by PFAS substances in the three experiments, suggesting three mechanisms of action of the chemicals depending on cell differentiation (i.e., monolayer or dome), moment of exposure (i.e., pre- or postdome formation), and cell population. In experiment 1, all PFAS substances produced alterations associated with DNA/RNA (e.g., $\nu_s PO_2^-$) (see Figure S2 and Table S1). The observed alterations in DNA/RNA are suggestive of a genotoxic insult. In fact, PFOA and PFNA are suspected genotoxic carcinogens through induction of reactive oxygen species that are responsible for oxidative DNA damage. Recently, Yahia et al.[49] demonstrated that PFOA and PFNA induced DNA damage in TK6 cells, observing that PFNA produced high levels of 8-hydroxy-2′-deoxyguanosine (8-OhdG), a biomarker of oxidative DNA damage. In contrast, in experiment 2, all PFAS substances caused alterations associated with secondary structures of proteins (Amide I, Amide II, and Amide III) (see Figure S2 and Table S1). The alteration of proteins observed under conditions 2 (9-day experiment) might be attributed to a direct consequence of the effects produced on DNA in the first conditions (2-day experiment) since effects on DNA are ultimately expressed in the proteins that it encodes. In experiment 3, all PFAS substances produced alterations associated with fatty acids (see Figure S2 and Table S1). In this experiment, one could expect similar effects as in experiment 1 since in both cases cells are analyzed right after PFAS exposure. However, the observed differences might be attributed to the different numbers of cells between both experiments and their dissimilar physiological properties (i.e., monolayer vs domes). Continuing with the study of distinguishing features induced by PFAS treatments, special attention was focused on lipids, due to the reported capacity of PFAS substances to alter lipid species of cellular membranes. A previous study performed on human placental chroriocarcinoma JEG-3 cells exposed to a mixture of eight PFAS substances by LC-MS[32] revealed that increased levels of the major components of cell membranes [i.e., phosphatidylcholine (PC), lyso plasmalogen PC, and plasmalogen PC] and a relatively low increase in triacylglicerols (TAG) were induced by PFAS substances. Similarly, our findings showed some effects of PFAS on lipids of A6 cells. As observed in Table S1, in experiment 1 PFOS and PFOA produced effects at 1,736 cm^{-1} (C═O stretching lipids) and at 1,444 cm^{-1} (lipids), respectively, and in experiment 2 PFBS induced alterations at 1,750 cm^{-1}, associated with a C═C stretching in lipids, as occurred with cells exposed to PFNA in experiment 3. The findings of this study demonstrate that PFAS substances pose a significant effect on the metabolome and lipidome of *Xenopus laevis* A6 cells. However, more information is needed in order to detect and identify potential biomarkers of lipid and metabolite disruption and to find most altered biochemical pathways, and future studies should focus on this point. Liquid chromatography coupled to high resolution mass spectrometry (LC-HRMS) techniques, which enable the analysis of compounds at low doses with high accuracy mass determination, are highly suitable for such purposes. Moreover, the fusion of IR data with LC-MS data is also worthy since it can provide a more comprehensive knowledge of the effects of PFAS substances in this amphibian cell model.

Finally, results of the growth-curve experiment showed different responses of A6 cells exposed to PFBS/PFNA compared to PFOS/PFOA (Figure 4). PFBS and PFNA did not induce distinguishable A6 cell proliferation or depletion compared to those of the control. In contrast, PFOS and PFOA induced a decrease in A6 cell number compared to that of the control, in a time- and dose-specific manner: after 48 h of treatment, a time when the two PFAS substances presented maximum effects, high-dose PFOS produced the most profound cell decreases, whereas low-dose PFOA caused the maximum decline in cell population. The capacity of PFOS and

DOI: 10.1021/acs.chemrestox.6b00076
Chem. Res. Toxicol. XXXX, XXX, XXX−XXX

PFOA to inhibit cell proliferation has been reported in other studies. Recently, Cui et al.[50] found that 80% inhibitory concentration (IC_{80}) of PFOA (150.97 μg/mL) and 50% inhibitory concentration (IC_{50}) of PFOS (27.92 μg/mL) blocked cell cycle and proliferation of Zebrafish (*Danio rerio*) liver cells (ZFL). Also, other studies showed PFOA capacity to induce apoptosis in hepatoma HepG2 cells.[51,52]

Overall, this work contributes to the better knowledge of PFAS substance effects on *Xenopus laevis* A6 kidney epithelial cells indicating an overall interference with DNA/RNA, secondary structures of proteins, lipids, and fatty acids at concentrations well below those associated with other adverse effects, such as cytotoxicity or endocrine disruption. This work also highlights (a) the differential effects of PFAS substances depending on cell-differentiation, presenting a nonmonotonic-behavior on A6 cells forming monolayers and (b) the ability of PFOS and PFOA to induce cell death.

■ ASSOCIATED CONTENT

Supporting Information

The Supporting Information is available free of charge on the ACS Publications website at DOI: 10.1021/acs.chemrestox.6b00076.

Theory section including a short description of PCA-LDA and ASCA methods, supplementary figures showing spectral preprocessing, PCA-LDA cluster vectors plots, structure of ASCA data sets, and a table containing principal segregating wavenumbers derived from PCA-LDA (PDF)

■ AUTHOR INFORMATION

Corresponding Author

*Tel.: +44 0-1524 510206. E-mail: f.martin@lancaster.ac.uk.

Funding

The research leading to these results has received funding from the European Research Council under the European Union's Seventh Framework Programme (FP/2007-2013)/ERC Grant Agreement n. 320737. The research of the first author is supported by a predoctoral FPU scholarship (FPU13/04384) from the Spanish Government (Ministerio de Educación, Cultura y Deporte). Research in F.L.M.'s laboratory is supported by Rosemere Cancer Foundation.

Notes

The authors declare no competing financial interest.

■ ACKNOWLEDGMENTS

We thank Debbie Hurst for support with microscopy instrumentation, Rebecca Strong for cell culture assistance, and Kirsi Liimatainen for her contribution to the discussion.

■ ABBREVIATIONS

ASCA, ANOVA-simultaneous component analysis; ATCC, American Type Culture Collection; ATR-FTIR, attenuated total reflection Fourier-transform IR; EC_{50}, median effective dose; EDCs, endocrine-disrupting chemicals; ENaC, epithelial Na^+ channel; FBS, fetal bovine serum; IC_{50}, 50% inhibitory concentration; IC_{80}, 80% inhibitory concentration; LDA, linear discriminant analysis; 8-OhdG, 8-hydroxy-2′-deoxyguanosine; PC, phosphatidylcholine; PCA, principal component analysis; 1-D PCA-LDA, one-dimensional principal component analysis plus linear discriminant analysis; PCs, principal components; PFASs, perfluoroalkylated substances; PFBS, perfluorobutanesulfonate; PFNA, perfluorononanoic acid; PFOA, perfluorooctanoic acid; PFOS, perfluorooctanesulfonate; SDS, sodium dodecyl sulfate; TAG, triacylglicerols

■ REFERENCES

(1) Campos, B., Garcia-Reyero, N., Rivetti, C., Escalon, L., Habib, T., Tauler, R., Tsakovski, S., Piña, B., and Barata, C. (2013) Identification of metabolic pathways in Daphnia magna explaining hormetic effects of selective serotonin reuptake inhibitors and 4-nonylphenol using transcriptomic and phenotypic responses. *Environ. Sci. Technol. 47*, 9434−9443.

(2) Kim, H. K., Choi, Y. H., and Verpoorte, R. (2011) NMR-based plant metabolomics: where do we stand, where do we go? *Trends Biotechnol. 29*, 267−275.

(3) Griffiths, W. J., and Wang, Y. (2009) Mass spectrometry: from proteomics to metabolomics and lipidomics. *Chem. Soc. Rev. 38*, 1882−1896.

(4) Cozzolino, D. (2012) Benefits and Limitations of Infrared Technologies in Omics Research and Development of Natural Drugs and Pharmaceutical Products. *Drug Dev. Res. 73*, 504−512.

(5) Lobartini, J. C., Tan, K. H., Rema, J. A., Gingle, A. R., Pape, C., and Himmelsbach, D. S. (1992) The geochemical nature and agricultural importance of commercial humic matter. *Sci. Total Environ. 113*, 1−15.

(6) Stewart, D. (1996) Fourier Transform Infrared Microspectroscopy of Plant Tissues. *Appl. Spectrosc. 50*, 357−365.

(7) Kacuráková, M. (2000) FT-IR study of plant cell wall model compounds: pectic polysaccharides and hemicelluloses. *Carbohydr. Polym. 43*, 195−203.

(8) Walsh, M. J., Holton, S. E., Kajdacsy-Balla, A., and Bhargava, R. (2012) Attenuated total reflectance Fourier-transform infrared spectroscopic imaging for breast histopathology. *Vib. Spectrosc. 60*, 23−28.

(9) Kallenbach-Thieltges, A., Großerüschkamp, F., Mosig, A., Diem, M., Tannapfel, A., and Gerwert, K. (2013) Immunohistochemistry, histopathology and infrared spectral histopathology of colon cancer tissue sections. *J. Biophotonics 6*, 88−100.

(10) Bird, B., Miljković, M. S., Remiszewski, S., Akalin, A., Kon, M., and Diem, M. (2012) Infrared spectral histopathology (SHP): a novel diagnostic tool for the accurate classification of lung cancer. *Lab. Invest. 92*, 1358−1373.

(11) Theophilou, G., Lima, K. M. G., Briggs, M., Martin-Hirsch, P. L., Stringfellow, H. F., and Martin, F. L. (2015) A biospectroscopic analysis of human prostate tissue obtained from different time periods points to a trans-generational alteration in spectral phenotype. *Sci. Rep. 5*, 13465.

(12) Scaglia, E., Sockalingum, G. D., Schmitt, J., Gobinet, C., Schneider, N., Manfait, M., and Thiéfin, G. (2011) Noninvasive assessment of hepatic fibrosis in patients with chronic hepatitis C using serum Fourier transform infrared spectroscopy. *Anal. Bioanal. Chem. 401*, 2919−2925.

(13) Hands, J. R., Abel, P., Ashton, K., Dawson, T., Davis, C., Lea, R. W., McIntosh, A. J. S., and Baker, M. J. (2013) Investigating the rapid diagnosis of gliomas from serum samples using infrared spectroscopy and cytokine and angiogenesis factors. *Anal. Bioanal. Chem. 405*, 7347−7355.

(14) Gajjar, K., Trevisan, J., Owens, G., Keating, P. J., Wood, N. J., Stringfellow, H. F., Martin-Hirsch, P. L., and Martin, F. L. (2013) Fourier-transform infrared spectroscopy coupled with a classification machine for the analysis of blood plasma or serum: a novel diagnostic approach for ovarian cancer. *Analyst 138*, 3917−3926.

(15) Llabjani, V., Jones, K. C., Thomas, G. O., Walker, L. A., Shore, R. F., and Martin, F. L. (2009) Polybrominated Diphenyl Ether-Associated Alterations in Cell Biochemistry as Determined by Attenuated Total Reflection Fourier-Transform Infrared Spectroscopy: a Comparison with DNA-Reactive and/or Endocrine-Disrupting Agents. *Environ. Sci. Technol. 43*, 3356−3364.

DOI: 10.1021/acs.chemrestox.6b00076
Chem. Res. Toxicol. XXXX, XXX, XXX−XXX

(16) Llabjani, V., Trevisan, J., Jones, K. C., Shore, R. F., and Martin, F. L. (2010) Binary mixture effects by PBDE congeners (47, 153, 183, or 209) and PCB congeners (126 or 153) in MCF-7 cells: biochemical alterations assessed by IR spectroscopy and multivariate analysis. *Environ. Sci. Technol. 44*, 3992−3998.
(17) Pang, W., Li, J., Ahmadzai, A. A., Heppenstall, L. D., Llabjani, V., Trevisan, J., Qiu, X., and Martin, F. L. (2012) Identification of benzo[a]pyrene-induced cell cycle-associated alterations in MCF-7 cells using infrared spectroscopy with computational analysis. *Toxicology 298*, 24−29.
(18) Li, J., Strong, R., Trevisan, J., Fogarty, S. W., Fullwood, N. J., Jones, K. C., and Martin, F. L. (2013) Dose-related alterations of carbon nanoparticles in mammalian cells detected using biospectroscopy: potential for real-world effects. *Environ. Sci. Technol. 47*, 10005−10011.
(19) Ollesch, J., Drees, S. L., Heise, H. M., Behrens, T., Brüning, T., and Gerwert, K. (2013) FTIR spectroscopy of biofluids revisited: an automated approach to spectral biomarker identification. *Analyst 138*, 4092−4102.
(20) Baker, M. J., Trevisan, J., Bassan, P., Bhargava, R., Butler, H. J., Dorling, K. M., Fielden, P. R., Fogarty, S. W., Fullwood, N. J., Heys, K. A., Hughes, C., Lasch, P., Martin-Hirsch, P. L., Obinaju, B., Sockalingum, G. D., Sulé-Suso, J., Strong, R. J., Walsh, M. J., Wood, B. R., Gardner, P., and Martin, F. L. (2014) Using Fourier transform IR spectroscopy to analyze biological materials. *Nat. Protoc. 9*, 1771−1791.
(21) Fearn, T. (2006) Discriminant Analysis, in *Handbook of Vibrational Spectroscopy* (Griffiths, J. M. C., Ed.) pp 2086−2093, Springer, New York.10.1002/0470027320.s4302
(22) Walsh, M. J., Singh, M. N., Pollock, H. M., Cooper, L. J., German, M. J., Stringfellow, H. F., Fullwood, N. J., Paraskevaidis, E., Martin-Hirsch, P. L., and Martin, F. L. (2007) ATR microspectroscopy with multivariate analysis segregates grades of exfoliative cervical cytology. *Biochem. Biophys. Res. Commun. 352*, 213−219.
(23) Martin, F. L., German, M. J., Wit, E., Fearn, T., Ragavan, N., and Pollock, H. M. (2007) Identifying variables responsible for clustering in discriminant analysis of data from infrared microspectroscopy of a biological sample. *J. Comput. Biol. 14*, 1176−1184.
(24) Martin, F. L., Kelly, J. G., Llabjani, V., Martin-Hirsch, P. L., Patel, I. I., Trevisan, J., Fullwood, N. J., and Walsh, M. J. (2010) Distinguishing cell types or populations based on the computational analysis of their infrared spectra. *Nat. Protoc. 5*, 1748−1760.
(25) Smilde, A. K., Jansen, J. J., Hoefsloot, H. C. J., Lamers, R.-J. A. N., van der Greef, J., and Timmerman, M. E. (2005) ANOVA-simultaneous component analysis (ASCA): a new tool for analyzing designed metabolomics data. *Bioinformatics 21*, 3043−3048.
(26) Stahl, T., Mattern, D., and Brunn, H. (2011) Toxicology of perfluorinated compounds. *Environ. Sci. Eur. 23*, 38−89.
(27) Manzetti, S., van der Spoel, E. R., and van der Spoel, D. (2014) Chemical properties, environmental fate, and degradation of seven classes of pollutants. *Chem. Res. Toxicol. 27*, 713−737.
(28) Du, G., Huang, H., Hu, J., Qin, Y., Wu, D., Song, L., Xia, Y., and Wang, X. (2013) Endocrine-related effects of perfluorooctanoic acid (PFOA) in zebrafish, H295R steroidogenesis and receptor reporter gene assays. *Chemosphere 91*, 1099−1106.
(29) Hines, E. P., White, S. S., Stanko, J. P., Gibbs-Flournoy, E. A., Lau, C., and Fenton, S. E. (2009) Phenotypic dichotomy following developmental exposure to perfluorooctanoic acid (PFOA) in female CD-1 mice: Low doses induce elevated serum leptin and insulin, and overweight in mid-life. *Mol. Cell. Endocrinol. 304*, 97−105.
(30) Gorrochategui, E., Pérez-Albaladejo, E., Casas, J., Lacorte, S., and Porte, C. (2014) Perfluorinated chemicals: differential toxicity, inhibition of aromatase activity and alteration of cellular lipids in human placental cells. *Toxicol. Appl. Pharmacol. 277*, 124−130.
(31) Gorrochategui, E., Casas, J., Pérez-Albaladejo, E., Jáuregui, O., Porte, C., and Lacorte, S. (2014) Characterization of complex lipid mixtures in contaminant exposed JEG-3 cells using liquid chromatography and high-resolution mass spectrometry. *Environ. Sci. Pollut. Res. 21*, 11907−11916.
(32) Gorrochategui, E., Casas, J., Porte, C., Lacorte, S., and Tauler, R. (2015) Chemometric strategy for untargeted lipidomics: biomarker detection and identification in stressed human placental cells. *Anal. Chim. Acta 854*, 20−33.
(33) Rafferty, K. A., Jr., and Sherwin, R. W. (1969) The length of secondary chromosomal constrictions in normal individuals and in a nucleolar mutant of *Xenopus laevis*. *Cytogenet. Genome Res. 8*, 427−438.
(34) Perkins, F. M., and Handler, J. S. (1981) Transport properties of toad kidney epithelia in culture. *Am. J. Physiol.: Cell Physiol. 241*, 154−159.
(35) Ichigi, J., and Asashima, M. (2001) Dome formation and tubule morphogenesis by Xenopus kidney A6 cell cultures exposed to microgravity simulated with a 3D-clinostat and to hypergravity. *In Vitro Cell. Dev. Biol.: Anim. 37*, 31−44.
(36) Kellenberger, S., and Schild, L. (2002) Epithelial Sodium Channel/Degenerin Family of Ion Channels: A Variety of Functions for a Shared Structure. *Physiol. Rev. 82*, 735−767.
(37) Ikuzawa, M., Akiduki, S., and Asashima, M. (2007) Gene expression profile of Xenopus A6 cells cultured under random positioning machine shows downregulation of ion transporter genes and inhibition of dome formation. *Adv. Space Res. 40*, 1694−1702.
(38) Rehn, M., Weber, W. M., and Clauss, W. (1998) Role of the cytoskeleton in stimulation of Na+ channels in A6 cells by changes in osmolality. *Pfluegers Arch. 436*, 270−279.
(39) Tanaka, M., Asashima, M., and Atomi, Y. (2003) Proliferation and differentiation of Xenopus A6 cells under hypergravity as revealed by time-lapse imaging. *In Vitro Cell. Dev. Biol.: Anim. 39*, 71−79.
(40) Trevisan, J., Angelov, P. P., Scott, A. D., Carmichael, P. L., and Martin, F. L. (2013) IRootLab: a free and open-source MATLAB toolbox for vibrational biospectroscopy data analysis. *Bioinformatics 29*, 1095−1097.
(41) Vis, D. J., Westerhuis, J. A., Smilde, A. K., and van der Greef, J. (2007) Statistical validation of megavariate effects in ASCA. *BMC Bioinf. 8*, 322−329.
(42) Movasaghi, Z., Rehman, S., and ur Rehman, D. I. (2008) Fourier Transform Infrared (FTIR) Spectroscopy of Biological Tissues. *Appl. Spectrosc. Rev. 43*, 134−179.
(43) Lawrence, J. E., Lamm, S. H., Pino, S., Richman, K., and Braverman, L. E. (2000) The effect of short-term low-dose perchlorate on various aspects of thyroid function. *Thyroid 10*, 659−663.
(44) Witorsch, R. J. (2002) Low-dose in utero effects of xenoestrogens in mice and their relevance to humans: an analytical review of the literature. *Food Chem. Toxicol. 40*, 905−912.
(45) vom Saal, F. S., and Hughes, C. (2005) An extensive new literature concerning low-dose effects of bisphenol A shows the need for a new risk assessment. *Environ. Health Perspect. 113*, 926−933.
(46) Kamrin, M. A. (2007) The "low dose" hypothesis: validity and implications for human risk. *Int. J. Toxicol. 26*, 13−23.
(47) Vandenberg, L. N., Colborn, T., Hayes, T. B., Heindel, J. J., Jacobs, D. R., Lee, D.-H., Shioda, T., Soto, A. M., vom Saal, F. S., Welshons, W. V., Zoeller, R. T., and Myers, J. P. (2012) Hormones and endocrine-disrupting chemicals: low-dose effects and nonmonotonic dose responses. *Endocr. Rev. 33*, 378−455.
(48) Han, X., Nabb, D. L., Russell, M. H., Kennedy, G. L., and Rickard, R. W. (2012) Renal elimination of perfluorocarboxylates (PFCAs). *Chem. Res. Toxicol. 25*, 35−46.
(49) Yahia, D., Haruka, I., Kagashi, Y., and Tsuda, S. (2016) 8-Hydroxy-2′-deoxyguanosine as a biomarker of oxidative DNA damage induced by perfluorinated compounds in TK6 cells. *Environ. Toxicol. 31*, 192−200.
(50) Cui, Y., Liu, W., Xie, W., Yu, W., Wang, C., and Chen, H. (2015) Investigation of the Effects of Perfluorooctanoic Acid (PFOA) and Perfluorooctane Sulfonate (PFOS) on Apoptosis and Cell Cycle in a Zebrafish (Danio rerio) Liver Cell Line. *Int. J. Environ. Res. Public Health 12*, 15673−15682.
(51) Shabalina, I. G. (1999) Effects of the rodent peroxisome proliferator and hepatocarcinogen, perfluorooctanoic acid, on apoptosis in human hepatoma HepG2 cells. *Carcinogenesis 20*, 2237−2246.

DOI: 10.1021/acs.chemrestox.6b00076
Chem. Res. Toxicol. XXXX, XXX, XXX−XXX

(52) Panaretakis, T., Shabalina, I. G., Grandér, D., Shoshan, M. C., and DePierre, J. W. (2001) Reactive oxygen species and mitochondria mediate the induction of apoptosis in human hepatoma HepG2 cells by the rodent peroxisome proliferator and hepatocarcinogen, perfluorooctanoic acid. *Toxicol. Appl. Pharmacol. 173*, 56−64.

DOI: 10.1021/acs.chemrestox.6b00076
Chem. Res. Toxicol. XXXX, XXX, XXX−XXX

SUPPLEMENTARY MATERIAL OF SCIENTIFIC ARTICLE VIII

Perfluoroalkylated substance efects in Xenopus laevis A6 kidney epithelial cells determined by ATR-FTIR spectroscopy and chemometric analysis

E. Gorrochategui, S. Lacorte, R. Tauler, F.L. Martin

Chemical Research in Toxicology (2016) **29 (5)**, 924-932

Supplementary liveslides at: https://pubs.acs.org/doi/suppl/10.1021/acs.chemrestox.6b00076/suppl_file/tx6b00076_liveslides.mp4

Theory

A brief description of the chemometric methods used in this study is shown below.

Principal Component Analysis plus Linear Discriminant Analysis (PCA-LDA)

PCA-LDA is a method that exploits the benefit of linear discriminant analysis (or canonical variants analysis, LDA), after using Principal Component Analysis[1,2] .

On the one hand, the central idea of PCA is to reduce the dimensionality of a data set consisting of large number of interrelated variables, using a small number of PCA factors [*i.e.*, principal components (PCs)] to retain as much as possible of the variation present in the original data set (> 95%)[3]. On the other hand, LDA is a data separation technique, which explicitly attempts to model the differences between the classes of the data set that were assigned *a priori*. New variables [linear discriminants (LD)] are found such that the ratio of the between-cluster variance to the within-cluster variance is maximized, and thus the clusters are visualized at maximum separation. Therefore, LDA, like regression methods such as Partial Least Squares, is a "supervised" method, that requires some previous knowledge of the samples constituents (*i.e.*, classes). PCA can be applied before LDA (thus "PCA-LDA") to reduce computational complexity, increase the recognition accuracy in different categories, and avoid LDA overfitting[4].

ANOVA-simultaneous component analysis (ASCA)

The ASCA method can be understood as a direct generalization of the analysis of variance (ANOVA) for univariate data to the multivariate case[5,6]. Moreover, this method incorporates the information of the structure of data sets (*i.e.*, underlying factors such as time, dose or combinations thereof), enabling a better understanding of their biological information. Thus, in ASCA, an ANOVA is initially performed on the raw data matrix, which is decomposed into the sum of different data matrices characterising the variance caused by each one of the considered factors, plus a residual matrix containing the unexplained variance. The ANOVA equation valid for the three data sets of the present study, acquired following an experimental design of two factors (*i.e.*, chemical -*c*- and dose -*d*-) is shown in **Equation S1**:

$$X = \mu + \alpha_c + \beta_d + \alpha\beta_{(cd)} + E \qquad (S1)$$

where **X** is a matrix containing the raw data acquired with the ATR-FTIR instrument, μ represents an overall offset, $\boldsymbol{\alpha_c}$ represents the effect of the factor "chemical", $\boldsymbol{\beta_d}$ represents the effect of the factor "dose", $\boldsymbol{\alpha\beta_{(cd)}}$ represents the interaction of "chemical" and "dose" and **E** is the residual matrix representing the natural variation among replicates. Thus, the performance of ANOVA allows the

division of the variation of the distinct factors in orthogonal and independent parts, which is also one of the goals of the ASCA model.

Following ANOVA, a simultaneous component analysis (SCA) is applied individually to each of the ANOVA factor matrices. SCA is a generalization of PCA for the situation where the same variables have been measured in multiple conditions.

Thus, ASCA model combines the power of ANOVA to separate variance sources with the advantages of SCA to the modelling of the individual separate effect matrices. The mathematical basis of the resulting ASCA model for the data set of the present study (*i.e.*, two-factor data set) is shown in **Equation S2**:

$$X = \mu + T_c P_c^T + T_d P_d^T + T_{(cd)} P_{(cd)}^T + E \qquad (S2)$$

where component scores of each sub-model are given by the matrices indicated by $\mathbf{T_c}$, $\mathbf{T_d}$, $\mathbf{T_{(cd)}}$, and the component loadings are given by matrices $\mathbf{P_c}$, $\mathbf{P_d}$, $\mathbf{P_{(cd)}}$. **E** is a matrix in which the residuals of all sub-models of the ASCA model are collected ($\mathbf{E = E_c + E_d + E_{(cd)}}$). Thus, this equation means that the matrix **X** is separated into contributions from the overall mean (**μ**), one SCA model ($\mathbf{T_c P_c^T}$) describing the overall effect of the factor "chemical", one SCA model ($\mathbf{T_d P_d^T}$) describing the overall effect of the factor "dose" and another SCA model ($\mathbf{T_{(cd)} P_{(cd)}^T}$) describing the interaction of "dose" with "chemical". Hence, the ASCA model (**Equation S2**) is a direct multivariate generalization of the ANOVA model (**Equation S1)**. In order to examine the statistical significance of the effects of the investigated factors and their interaction, ASCA performs a permutation test in which the null hypothesis ($\mathbf{H_0}$) assumes that there is no effect of the considered factor. However, such permutation test can only be performed under the assumption that raw data are well-balanced (*i.e.*, same number of observations for each factor level).

Figure S1. Visual effect of different pre-processing steps on a set of ATR-FTIR spectra, including feature selection, rubber band baseline correction, Amide I normalization, trained-mean centring and class definition.

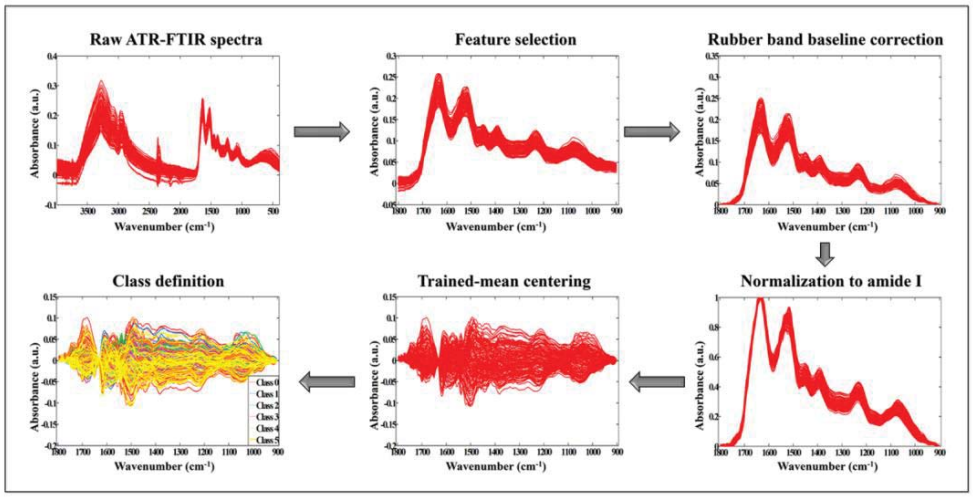

Figure S2. PCA-LDA loadings of PFBS, PFOA, PFOS and PFNA-treatments for the three experiments. Grey-shaded regions indicate spectral regions corresponding to particular biomolecuar entities affected in all PFAS-treatments and thicker lines indicate PFAS-doses causing higher effects.

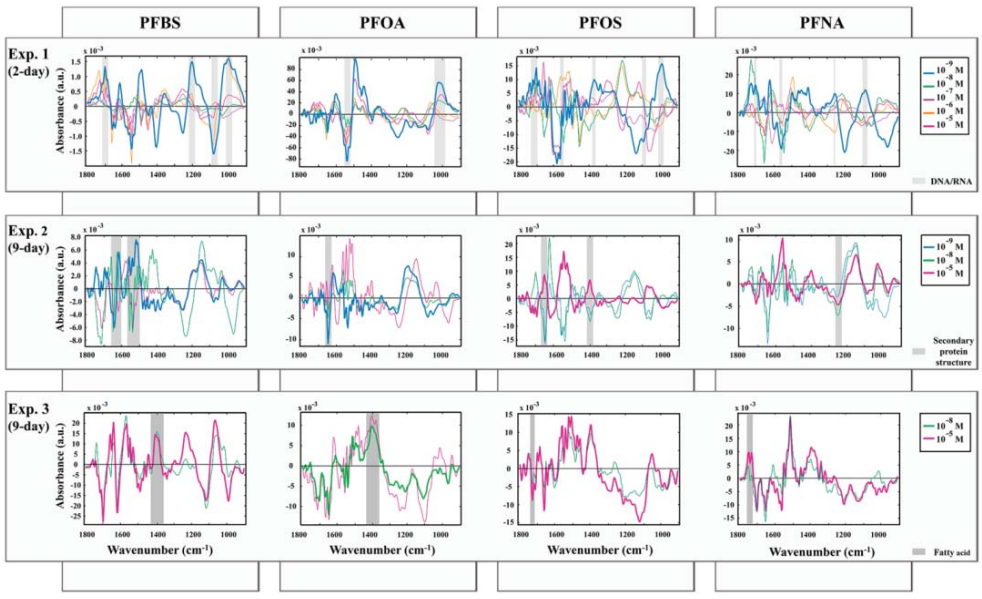

Figure S3. Structure of the data sets arranged for experiments 1, 2 and 3 to perform subsequent ASCA analyses. In the left part of the figures, each rectangle represents an ATR-FTIR spectrum, and the total of them is further arranged into a matrix, as indicated in the right-part of the figures. In all cases, the following indices are used: w=1,…,W for the wavenumbers, d=1,…,D for the doses tested (d_1=0 M, d_2=10^{-9} M, d_3=, 10^{-8} M, d_4=10^{-7} M, d_5=10^{-6} M and d_6=10^{-5} M), c=1,…,C for the chemicals tested (c_1= PFBS, c_2=PFOS, c_3=PFOA and c_4=PFNA) and i=1,…,I for the number of replicates of each category.

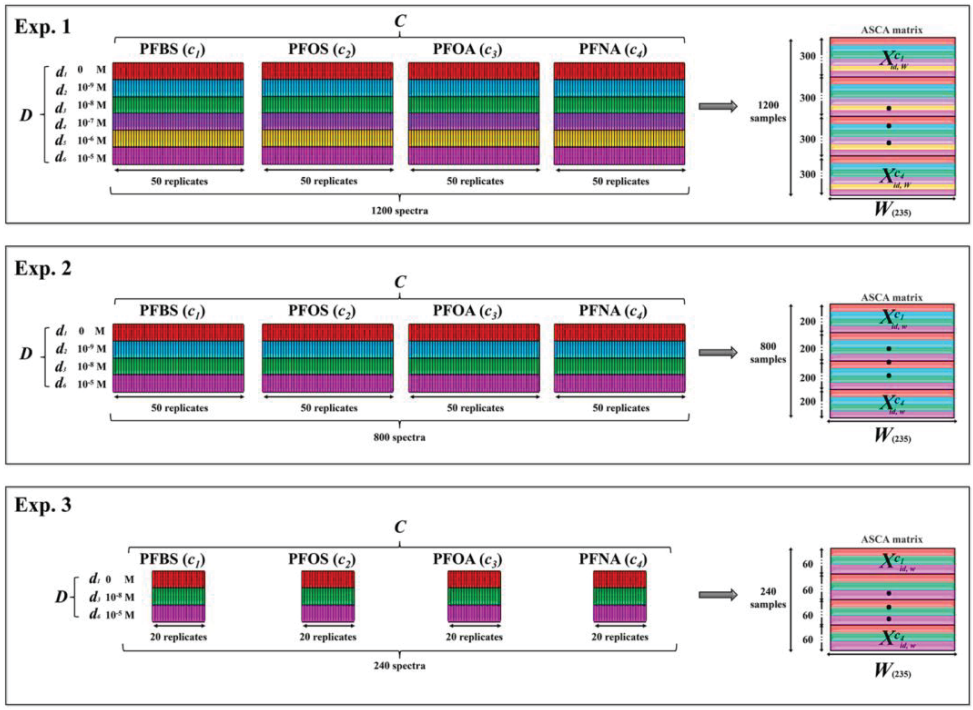

Table S1. Principal segregating wavenumbers and associated biomolecular entities[7] derived from cluster vector plots of **PCA-LDA**. The indicated wavenumbers (ranked from higher to lower priority) are shown for the distinct experiments and chemicals (*i.e.*, PFBS, PFOS, PFOA and PFNA) at the dose presenting highest effects. Grey-shaded raws indicate spectral bands associated to particular entities affeted by all chemicals: DNA/RNA (light gray, exp. 1), secondary protein structures (medium gray, exp. 2) and fatty acids (dark gray, exp. 3).

Exp.	Chemical treatment	Dose of highest effects	Wavenumber (cm^{-1})	Biological fingerprint
1	PFBS	10^{-9} M	1080	Stretching PO_2^- symmetric
			994	C-O ribose, C-C
			1201	PO_2^- asymmetric (phosphate I)
			1403	Symmetric CH_3 bending modes of the methyl groups of proteins
			1549	Amide II
			1698/9	C_2=O guanine/ N-H thymine
	PFOS	10^{-9} M	1489	In-plane CH bending vibration
			1581	Ring C-C stretching of phenyl
			1567	Ring base
			1137	Oligosaccharide C-OH stretching band
			996	C-O ribose, C-C
			1698/9	C_2=O guanine/ N-H thymine
			1095	Stretching PO_2^- symmetric
			1717	C=O thymine; C=O stretching vibration of DNA and RNA; C=O stretching vibration of purine base
			1373	Stretching C-N cytosine, guanine
			1736	C=O stretching (lipids)
	PFOA	10^{-9} M	1494	In-plane CH bending vibration
			1543	Amide II
			1020	DNA
			1524	Stretching C=N, C=C
			1555	Ring base
			1444	δ (CH_2), lipids, fatty acids
			1250	Amide III
	PFNA	10^{-9} M	1204	Vibrational modes of collagen proteins-amide III
			1558	Ring base
			1624	Unassigned band
			1728	C=O band
			1089	Stretching PO_2^- symmetric in RNA
			1705	C=O thymine
			1408	Unassigned band
			1258	PO_2^- asymmetric (phosphate I)
2	PFBS	10^{-9} M	1517	Amide II
			1510	In-plane CH bending vibration from the phenyl rings

			1616	Ring C-C stretching of phenyl
			1643	Amide I band (arises from C=O stretching vibrations)
			1559	Ring base
			1540	Protein Amide II absorption- predominately β-sheet of amide II
			1750	ν (C=C) lipids, fatty acids
	PFOS	**10^{-5} M**	1543	Amide II
			1524	Stretching C=N, C=C
			1559	Ring base
			1652	Amide I
			1396	Symmetric CH_3 bending of the methyl groups of proteins
			1620	Peak of nucleic acids due to the base carbonyl stretching and ring breathing mode
	PFOA	**10^{-9} M**	1647	Amide I in normal tissues
			1192	Unassigned band
			1535	Stretching C=N, C=C
			1620	Peak of nucleic acids due to the base carbonyl stretching and ring breathing mode
	PFNA	**10^{-5} M**	1562	Unassigned band
			1146	Phosphate and oligosaccharides
			1026	Carbohydrates peak for solutions; vibrational frequency of CH_2OH groups of carbohydrates (inclusing glucose, fructose, glycogen, etc.); glycogen
			1254	Amide III
			1400	Symmetric stretching vibration of COO^- group of fatty acids and amino acids
			1713	C=O thymine
3	**PFBS**	**10^{-5} M**	1698/9	C_2=O guanine/ N-H thymine
			1620	Peak of nucleic acids due to the base carbonyl stretching and ring breathing mode
			1068	Stretching C-O ribose
			1639	Amide I
			1567	Ring base
			994	C-O ribose, C-C
			1119	Symmetric stretching P-O-C; C-O stretching mode
			1234	Composed of amide III and phosphate vibration of nucleic acids
			1400	Symmetric stretching vibration of COO^- group of fatty acids and amino acids
	PFOS	**10^{-5} M**	1119	Symmetric stretching P-O-C; C-O stretching mode
			1504	In-plane CH bending from the phenyl rings
			1517	Amide II
			1396	Symmetric CH_3 bending of the methyl groups of proteins
			1659	Amide I
			1559	Ring base
			1539	Protein amide II absorption- predominately β–sheet of amide II
			1724	C=O stretching band mode of the fatty acid

			ester
PFOA	**10^{-8} M**	1400	Symmetric stretching vibration of COO^- group of fatty acids and amino acids
		1647	Amide I in normal tissues- for cancer is in lower frequencies
		1512	In-plane CH bending vibration from the phenyl rings
		1113	Symmetric stretching P-O-C
PFNA	**10^{-5} M**	1512	In-plane CH bending vibration from the phenyl rings
		1701	C=O guanine
		1651	Amide I
		1562	Unassigned band
		1393	Unassigned band
		1528	C=N guanine
		1748	*v* (C=C) lipids, fatty acids
		1732	Absorption band of fatty acid ester; Fatty acid ester band

References

(1) Fearn, T. (2002) Discriminant analysis, in *Handbook of Vibrational Spectroscopy* (Griffiths, J. M. C. and P. R., Ed.), pp 2086–2093. New York.

(2) Walsh, M. J., Singh, M. N., Pollock, H. M., Cooper, L. J., German, M. J., Stringfellow, H. F., Fullwood, N. J., Paraskevaidis, E., Martin-Hirsch, P. L., and Martin, F. L. (2007) ATR microspectroscopy with multivariate analysis segregates grades of exfoliative cervical cytology. *Biochem. Biophys. Res. Commun. 352*, 213–219.

(3) Llabjani, V., Jones, K. C., Thomas, G. O., Walker, L. A., Shore, R. F., and Martin, F. L. (2009) Polybrominated diphenyl ether-associated alterations in cell biochemistry as determined by attenuated total reflection Fourier-transform infrared spectroscopy: a comparison with DNA-reactive and/or endocrine-disrupting agents. *Environ. Sci.Technol. 43*, 3356-3364.

(4) Llabjani, V., Trevisan, J., Jones, K. C., Shore, R. F., and Martin, F. L. (2010) Binary mixture effects by PBDE congeners (47, 153, 183, or 209) and PCB congeners (126 or 153) in MCF-7 cells: biochemical alterations assessed by IR spectroscopy and multivariate analysis. *Environ. Sci. Technol. 44*, 3992–3998.

(5) Smilde, A. K., Jansen, J. J., Hoefsloot, H. C. J., Lamers, R.-J. A. N., van der Greef, J., and Timmerman, M. E. (2005) ANOVA-simultaneous component analysis (ASCA): a new tool for analyzing designed metabolomics data. *Bioinformatics 21*, 3043–3048.

(6) Farrés, M., Villagrasa, M., Eljarrat, E., Barceló, D., and Tauler, R. (2012) Chemometric evaluation of different experimental conditions on wheat (Triticum aestivum L.) development using liquid chromatography mass spectrometry (LC-MS) profiles of benzoxazinone derivatives. *Anal. Chim. Acta 731*, 24–31.

(7) Movasaghi, Z., Rehman, S., and ur Rehman, D. I. (2008) Fourier transform infrared (FTIR) spectroscopy of biological tissues. *Appl. Spectrosc. Rev. 43*, 134–179.

4.2.2. SCIENTIFIC ARTICLE IX

Diet-sourced carbon-based nanoparticles induce lípid alterations in tissues of zebrafish (Danio rerio) with genòmic hypermethylation changes in brain

E. Gorrochategui, J. Li, N.J. Fullwood, G.G. Ying, M. Tian, L. Cui, H. Shen, S. Lacorte, R. Tauler, F.L. Martin

Mutagenesis (2017) **32 (1)**, 91-103

Mutagenesis Advance Access published October 26, 2016

Mutagenesis, 2016, 00, 1–13
doi:10.1093/mutage/gew050
Original Manuscript

Original Manuscript

Diet-sourced carbon-based nanoparticles induce lipid alterations in tissues of zebrafish (*Danio rerio*) with genomic hypermethylation changes in brain

Eva Gorrochategui[1,§], Junyi Li[2,§], Nigel J. Fullwood[3], Guang-Guo Ying[4], Meiping Tian[5], Li Cui[5], Heqing Shen[5], Sílvia Lacorte[1], Romà Tauler[1] and Francis L. Martin[2,6,*]

[1]Department of Environmental Chemistry, Institute of Environmental Assessment and Water Research (IDAEA), Consejo Superior de Investigaciones Científicas (CSIC), Barcelona, 08034, Catalonia, Spain, [2]Centre for Biophotonics and [3]Biomedical and Life Sciences Division, Lancaster Environment Centre, Lancaster University, Lancaster LA1 4YQ, UK, [4]State Key Laboratory of Organic Geochemistry, Guangzhou Institute of Geochemistry, Chinese Academy of Sciences, Guangzhou 510640, China, [5]Key Lab of Urban Environment and Health, Institute of Urban Environment, Chinese Academy of Sciences, Xiamen 361021, China and [6]Biosciences, School of Pharmacy and Biomedical Sciences, Maudland Building, University of Central Lancashire, Preston PR1 2HE, UK

*Corresponding author: Tel: +44 1772 896482; Email: flmartin@uclan.ac.uk
[§]These authors contributed equally.

Received 11 May 2016; Revised 19 September 2016; Accepted 29 September 2016.

Abstract

With rising environmental levels of carbon-based nanoparticles (CBNs), there is an urgent need to develop an understanding of their biological effects in order to generate appropriate risk assessment strategies. Herein, we exposed zebrafish *via* their diet to one of four different CBNs: C_{60} fullerene (C_{60}), single-walled carbon nanotubes (SWCNT), short multi-walled carbon nanotubes (MWCNTs) or long MWCNTs. Lipid alterations in male and female zebrafish were explored post-exposure in three target tissues (brain, gonads and gastrointestinal tract) using 'omic' procedures based in liquid chromatography coupled with mass spectrometry (LC-MS) data files. These tissues were chosen as they are often target tissues following environmental exposure. Marked alterations in lipid species are noted in all three tissues. To further explore CBN-induced brain alterations, Raman microspectroscopy analysis of lipid extracts was conducted. Marked lipid alterations are observed with males responding differently to females; in addition, there also appears to be consistent elevations in global genomic methylation. This latter observation is most profound in female zebrafish brain tissues post-exposure to short MWCNTs or SWCNTs ($P < 0.05$). This study demonstrates that even at low levels, CBNs are capable of inducing significant cellular and genomic modifications in a range of tissues. Such alterations could result in modified susceptibility to other influences such as environmental exposures, pathology and, in the case of brain, developmental alterations.

Introduction

Carbon-based nanoparticles (CBNs) are key constituents in many technologies. As a consequence, environmental exposure is increasing in the absence of a full understanding of the potential risks that they might pose. Significant gaps in our understanding or the ability to assess such risks (1) exist and these include: (i) as they differ from chemicals, an absence of an understanding of their toxicodynamics

and toxicokinetics; (ii) an obscure mechanism of action; (iii) an absence of identified endpoints; and (iv) a lack of assays of exposure and effect. There is an urgent need to determine CBN-induced environmental effects in target organisms and to develop approaches towards measuring endpoint outcomes (2,3).

CBNs comprise a diverse range of entities including multi-walled carbon nanotubes (MWCNTs; long or short), single-walled carbon nanotubes (SWCNTs) and C_{60} fullerene (C_{60}). These carbon allotropes with cylindrical nanostructures have unusual properties that confer advantages in electronics, optics, materials sciences and nanotechnology. In the environment, they possess the ability to either interact with cell membranes or even penetrate into cells to interact with organelles. Figure 1 shows an example of long MWCNTs that have penetrated into a stromal fibroblast, taken from a representative exposed tissue. They may surround or further penetrate into subcellular structures such as lysosomes. The consequences of such effects might be the generation of reactive oxygen species (ROS), rupture of organelles with consequent leakage of degradative enzymes or effects on the lipidome (2,4). Understanding the effects on the lipidome is of crucial interest, because lipids play essential roles in energy production and storage and cell membrane development (5,6), and thus, their study can aid in understanding the pathogenesis of many disease states. Given the multiplicity of possible outcomes, 'omic' procedures might be a better approach towards determining endpoint effects. The significance of parameters such as lipid peroxidation, potential genetic damaged induced by ROS and genomic methylation are critical to our understanding of environmental nanotoxicology (7–12).

Omic procedures using liquid chromatography coupled with mass spectrometry (LC-MS)-based methods have the ability for the analysis of low-molecular-weight compounds, such as complex lipid mixtures or biomolecules, in biological systems (13). The large amount of information contained in LC-MS data files (14) can be processed using chemometric tools such as multivariate curve resolution–alternating least squares (MCR-ALS) (15), which has been shown in recent omic (e.g. lipidomic) studies to successfully resolve extensive LC-MS data sets with strongly co-eluted and hidden peaks (16–21). In addition, principal component analysis (PCA) or partial least squares discriminant analysis (PLS-DA) can further explore sample classification/discrimination and allow biomarker discovery (22).

Application of spectrochemical methods such as Raman microspectroscopy to biological systems follows a similar premise (23). The advantage of this reagent-free and non-destructive approach is that it readily generates a signature fingerprint of the analysed sample. Applying a computational framework to a generated data set allows one to extract distinguishing features associated with altered chemical bonds; these can be associated with constituents such as lipids, proteins or DNA/RNA (24). Raman microspectroscopy has been applied to shed insights into CBN-induced effects (25,26), cell lineage (27) and to generate tissue images (28).

Considering that ROS generation might be an underlying mechanism of CBN-induced toxicity, herein we examine the effects of low dietary exposures on three target tissues (brain, gonads and gastrointestinal tract) in male and female zebrafish. Although many such studies have examined liver, a major downside to this approach is that pathological effects rarely feature highly in this target tissue. Central to our hypothesis for conducting this study, we chose gastrointestinal tract as the initial target tissue following dietary exposure, brain as there is an emerging notion that nanoparticles might modify development and gonads to determine any potential effects on reproductive biology. Primarily, we examine lipid alterations through LC-MS and Raman microspectroscopy; this is extended to examine genomic methylation levels post-exposure in brain. Our aim is to examine whether sublethal CBN exposures might induce subtle alterations that could ultimately be associated with development or pathological changes.

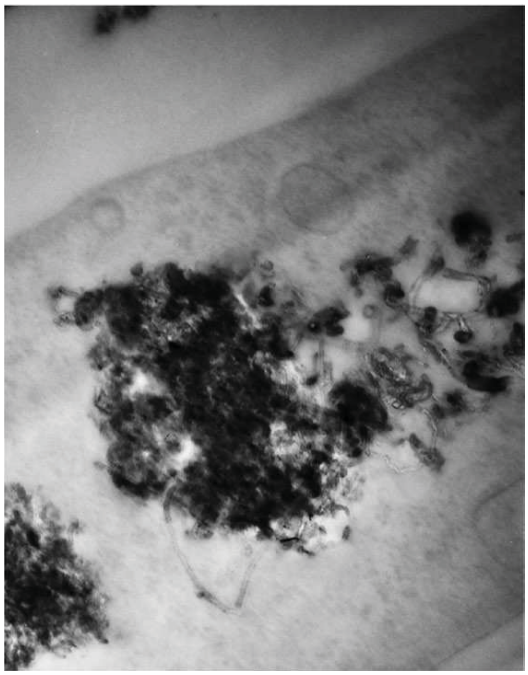

Figure 1. Transmission electron micrograph of a clump of nanotubes within the cytoplasm of a cell. Individual MWNTs are visible projecting from edges of the clump. The micrograph shows how large quantities of nanotubes can be internalised and accumulated within the cell cytoplasm.

Animals, materials and methods

Chemicals and CBNs

Bovine serum albumin (BSA) obtained from Sigma was ≥98%. All CBNs were purchased from Sigma. Short MWCNTs were >90% pure being 10–15 nm in diameter and 0.1–10 μm in length. Long MWCNTs were >90% pure also but were 110–170 nm in diameter and 5–9 μm in length. C_{60} had a purity >99.5% and particle size of 1 nm. SWCNTs were described as CarboLex AP-grade (the purity of AP-grade products ranges from 50% to 70% by volume); major impurities are carbon nanospheres and carbon-encapsulated catalyst nanoparticles—the diameter was 1.2–1.5 nm. All CBNs were analysed by Raman spectroscopy (Renishaw PLC, UK) with a 785 nm laser and determined to be of high purity; CBNs were reanalysed throughout the course of the study and no degradation in their purity was noted during this time. Additionally, images of CBNs were taken using a scanning electron microscope (JSM 5600, JEOL) (2–4). CBNs were dispersed in 1% BSA solution with a 15-min ultrasonication and stock solutions were made at concentrations of 100 mg L^{-1} and 1 mg L^{-1}. CNT solutions were stable and well-dispersed, while C_{60} appeared to agglomerate.

Such CNT solutions are known to be stable (29). In DLVO theory, the agglomeration and stability of particle dispersions are determined by the sum of the attractive and repulsive forces between individual particles. The attraction between particles is due to van der Waals

forces. The interaction of electrical double layers surrounding each particle is called electrostatic repulsive force. Typically, when dispersing CNPs in solution, they can form agglomerates, or remain as aggregates, surrounded by an electrical double layer. To overcome this problem, two different approaches are currently being used to disperse carbon nanotubes, i.e. mechanical (or physical) methods and chemical methods. Using mechanical methods such as ultrasonication with a suitable period of mixing, nanotubes are separated from each other. Chemical methods use surfactants or chemical moieties to change the surface energy of the nanotubes, improving their wetting or adhesion characteristics and improving their dispersion stability in solvent. However, many dispersants cannot be applied to biological research due to their intrinsic toxicity in *in vitro* and *in vivo* systems. The non-covalent adsorption of BSA, as a biocompatible dispersant, on the surface of CNTs could change the surface charge of CNTs. However, C_{60} is more likely to aggregate forming as nC_{60} than CNTs.

Fish maintenance and experimental conditions

All experiments were carried out in accordance with local Institutional Review Board requirements. Zebrafish were maintained in the Aquatic Toxicology Laboratory at the Guangzhou Institute of Geochemistry (Chinese Academy of Sciences). All fish were kept in 50 L flow-through tanks filled with dechlorinated tap water in a temperature-controlled room maintained at 27 ± 1°C. The room was on a 14:10 h light:dark cycle, and fish were fed once daily with a quantity of commercial food at 5% of the wet weight.

Fish exposures were conducted in 10 L glass tanks, and each experimental tank contained 5 L dechlorinated tap water and 4 fish (2 males and 2 females). Prior to exposure, zebrafish in 50 L tanks were randomly transferred to the experimental tank for a 7-day adaptive period. Following this, CNP exposure was initiated and run for 21 days. There were 15 randomly assigned tanks for total exposure (control and treatment with each CBN at 0.1 mg L^{-1} in triplicate). Exposure concentration was chosen based on previous *in vitro* studies (2), which showed that, speculated real-world environmental levels induced alterations in exposed cell populations are detectable by biospectroscopy techniques (3, 4). To minimize contamination, fish were only fed in the morning every day; in the afternoon, each tank was cleaned to remove fish faeces and food remains by siphoning the water out of the tanks. Then all tanks were filled with fresh water and fresh treatment. All fish were killed within seconds by immersion in melting ice at the end of the exposure. From each fish, brain, gonads and intestine were independently harvested and stored in liquid nitrogen for further analysis. Exposure experiments were conducted in triplicate.

Transmission electron microscopy

Stromal fibroblasts were isolated from a representative tissue section post-exposure to long MWCNTs; these were fixed in 2.5% glutaraldehyde in 0.1 M cacodylate buffer for 2 h. Samples were washed three times in buffer before being post fixed in 2% aqueous osmium tetroxide for 1 h. Samples were washed again in buffer prior to dehydration through a graded ethanol series. They were then transferred to propylene oxide for two 30-min steps and transferred to Araldite resin overnight before being placed in fresh resin and polymerised for 24 h at 60°C. Ultrathin sections were collected on copper grids stained briefly with phosphotungstic acid and Reynold's lead citrate prior to examination on a JEOL 10-10 transmission electron microscope.

Lipid extraction

Approximately 0.5 mg amounts of tissue were homogenized in 0.1% ammonium acetate. Then methanol (1.5 mL) was added to a 200-µL sample aliquot, which was placed into a glass tube with a Teflon-lined cap, and the tube was vortexed. Five millilitre of methyl tert-butyl ether (MTBE) was added and the mixture was incubated for 1 h at room temperature in a shaker. Adding 1.25 mL of high-performance liquid chromatography-grade water-induced phase separation. Upon 10 min of incubation at room temperature, the sample was centrifuged at 1000 *g* for 10 min. The upper (organic) phase was collected, and organic phases were dried in a vacuum centrifuge. Half of the extracted lipids were dissolved in MTBE for Surface-enhanced Raman spectroscopy (SERS), the other was dissolved in 200 µL of methanol for further LC-high–resolution mass spectrometry (HRMS) analysis.

LC-MS analysis

LC-HRMS analysis was performed using an Acquity ultrahigh-performance liquid chromatography (UHPLC) system (Waters, USA) connected to a time-of-flight (LCT Premier XE) detector with an Acquity UHPLC BEH C_8 column (1.7 µm particle size, 100 mm × 2.1 mm, Waters, Ireland) at a flow rate of 0.3 mL min^{-1} and column temperature of 30°C. Full scan spectra from 50 to 1500 Da were acquired, and individual spectra were summed to produce data points each of 0.2 s. Mass accuracy at a resolving power of 10 000 and reproducibility were maintained using an independent reference spray *via* the LockSpray interference. The mobile phases were methanol with 2 mM ammonium formiate and 0.2% formic acid (A)/water with 2 mM ammonium formiate and 0.2% formic acid (B). Phosphatidylcholine (PC), plasmalogen PC, lyso plasmalogen PC, phosphatidylethanolamine (PE), phosphatidylserine (PS), diacylglycerol (DAG) and triacylglycerol (TAG) species were analysed under positive ESI (electrospray ionization).

Chemometric analysis of LC-HRMS data

Each UHPLC-HRMS chromatographic run recorded for every sample resulted in a data file, which was converted to NetCDF format and further imported into MATLAB environment (30). Then, data were loaded into MATLAB workspace and transformed to data matrices, while reducing their size using in-house written routines that search for the regions of interest (ROI) and construct compressed data matrices containing relevant LC-HRMS features (23) without any loss of spectral mass accuracy (see supplementary Figure 1, available at *Mutagenesis* Online). ROI data matrices contain mass spectra at all retention times in their rows and at the ROI selected *m/z* values in their columns. In order to compare the distinct samples (control and stressed), new column-wise augmented data matrices were generated, arranging samples one at the top of each other (sample × elution time, *m/z* values) (see supplementary Figure 2, available at *Mutagenesis* Online). The final augmented data matrix containing information of the 90 samples was then generated (see supplementary Figure 3, available at *Mutagenesis* Online) in this way. Then, the MCR-ALS method (16) was applied to the final augmented data matrix for the resolution of co-eluted elution profiles and hidden peaks of the different sample constituents (lipids) as well as their corresponding mass spectra. In this analysis, 150 components were simultaneously resolved, each one describing a pure elution and mass spectral profile, and a 99.2% of the total variance was explained (see supplementary Figure 4, available at *Mutagenesis* Online). Also, relative areas of the resolved elution profiles for each of these components in the different analysed samples (control and treatment for the different tissues) were obtained. The elution profiles of the 150 components were further examined and only those that described reliable chromatographic peak features were selected,

whereas components explaining background instrumental noise or solvent contribution were excluded. From the spectra profiles of the relevant MCR-ALS components, 94 lipids were finally identified, and from their relative areas, it was possible to evaluate their relative amounts in each sample. A first exploratory evaluation of the calculated MCR-ALS relative areas using a PCA of the 90 samples and 94 variables (lipid species) was performed. Six components were selected to build the model, explaining a cumulative variance of 78.02% (Figure 2). For a detailed examination, and in order to explore potential biomarkers (i.e. components showing significant differences in control *versus* treatment samples), two complementary methods were used. First, a PLS-DA was performed in the data matrix containing calculated areas of the 94 identified lipid species for the 90 samples. PLS-DA was applied 24 times, considering one pair of classes each time (i.e. 4 treatments × 3 tissues × 2 genders). The determination of lipids showing significant differences was feasible when observing variables importance in projection (VIP) scores with a threshold higher than one (see supplementary Figure 5, available at *Mutagenesis* Online). Further, two-sample Student's *t*-test ($P < 0.05$) was used to corroborate the previously encountered potential biomarkers. Finally, only those lipid species showing significant alterations in both approaches (VIPs from PLS-DA and Student's *t*-test) were proposed as potential biomarkers (see supplementary Table 1, available at *Mutagenesis* Online). Changes in lipid areas among the distinct sample groups were also examined by performing a hierarchical cluster analysis (HCA) together with headmapping display (31), which also allowed the evaluation of lipid species showing similar behaviour amongst CBNs exposure.

Peak assignment and identification of lipids

For the identification of the MCR-ALS-resolved components, both a home-made database of lipids built previously (17,32) using the same chromatographic conditions and external databases available online such as LipidMaps (http://www.lipidmaps.org) and Human Metabolome Database were used. The assigned compound corresponded to the lipid molecule with the minimum mass error value (≤10 ppm) respect to the measured *m/z*, considering the possible adducts in positive ionization mode. The lipid annotated also had to fulfil an adequate retention time regarding its polarity. Glycerophospholipids, TAG and DAG species were annotated as <lipid subclass> <total fatty acyl chain length> <total number of unsaturated bonds>. In this study, 30 PC, 3 Plasmalogen PC, 3 Lyso PC, 1 Lyso plasmalogen PC, 3 PE, 10 PS, 40 TAG and 4 DAG lipid species were identified (see supplementary Table 2, available at *Mutagenesis* Online).

Software for LC-MS data analysis

MATLAB 8.6.0 R2015a and R2015b (The MathWorks, Inc., Natick, MA, USA) were used as the development platforms for LC-MS data analysis and visualization. A graphical interface was used to apply MCR-ALS, which additionally provided detailed information about the implementation of this algorithm. Statistics Toolbox™ for MATLAB, PLS Toolbox 7.3.1 (Eigenvector Research Inc., Wenatchee, WA, USA), Bioinformatics Toolbox™ and other home-made routines (30) were used in this work. Waters/Micromass MassLynx™ V 4.1 software was used for data set conversion from raw into NetCDF format and as one of the formula identification platforms through its elemental composition tool.

Surface-enhanced Raman spectroscopy

SERS was performed using nanosilver, supplied from Dr Cui Li's Lab (33,34). Three spectra were acquired from each sample (three samples for each group). Silver nanoparticles (Ag NPs) for SERS were synthesised using trisodium citrate as the reductants (33,34). For SERS interrogation, the lipid extracts in MTBE were mixed with Ag NPs. After vortexing, an aliquot of 10 µL of the mixture were dropped onto a glass slide for SERS measurement.

SERS spectra were acquired using a LabRAM Aramis (HORIBA JobinYvon) confocal micro-Raman system equipped with a 1200 g mm^{-1} grating, helium–neon 632.8 nm laser (laser power ≤70 mW prior to lens). System calibration was carried out using a silicon calibration source for wavenumber shift. A 50× objective (Olympus) with a numerical aperture of 0.55 was used to focus the laser beam and collect Raman signal with a working distance of about 8 mm. In

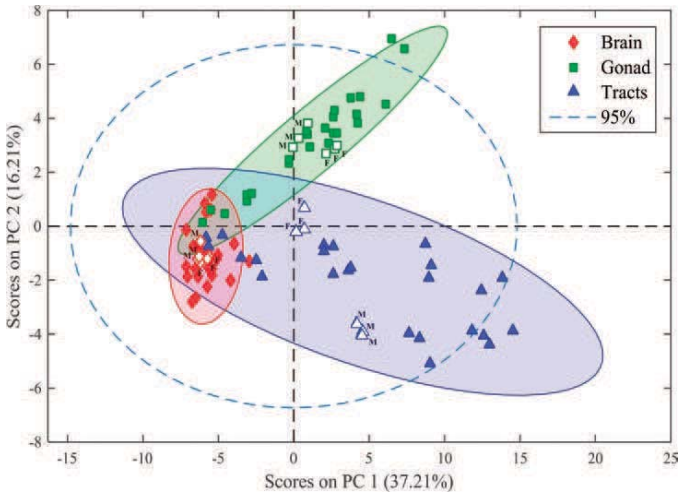

Figure 2. PCA scores plot of the 90 samples analysed (MCR-ALS relative areas of the 94 identified lipid species), corresponding to brain, gonad and gastrointestinal tract tissues of male and female zebrafish including control (open symbols) and stressed-samples (solid symbols). (F: female, M: male).

order to reduce any laser damage to cells, DuoScan in the micromapping mode with a scanning area of 30 µm × 30 µm was applied with an acquisition time of 5 s.

Spectral data processing, acquired from Raman spectroscopy, were performed using IRootLab toolbox (http://irootlab.google-code.com) running on MATLAB r2010a (The MathWorks, Inc., USA) (35). SERS spectra were initially processed in LabSpec 6 (software provided with the Raman system) for cosmic ray removal and background correction. The spectral data were then inputted into MATLAB and preprocessed following wavelet de-noising, cut to 400–1800 cm^{-1}, second differentiation and vector normalisation (36). The differentiation is employed both as a means of baseline correction and to resolve overlapped bands (23). The wavelet de-noising utilises non-linear filtering implemented through multi-scale decomposition and thresholding for de-noising, especially for the spectra containing sharp peaks. Computational analysis using multivariate techniques including PCA and linear discriminant analysis (LDA) can efficiently analyse such large spectral data sets (24,37). The main difference between PCA and LDA is that the former is an unsupervised method, whilst the latter is supervised. PCA looks for projections to maximise variance and LDA looks for projections that maximise the ratio of between-category to within-category scatter. Following preprocessing, PCA was applied to the data set. PCA reduces the dimensions of the data. Undoubtedly, PCA is capable of identifying important information in spectral data but has less discriminatory power. Often, in order to interpret complex biochemical information with labelled classes, further analysis using supervised procedures like LDA is required (37). The output data derived from PCA or PCA-LDA (the first 10 PC factors of PCA are used for LDA since >99% of variance is captured) can then be visualised as 1-D, 2-D or 3-D scatterplots ('scores plots'). In scores plots, nearness between two categories implies similarity, while distance indicates dissimilarity. To reveal the biochemical alterations associated with each category in the data set, both loading plots and cluster vectors were developed. To simplify the identification of the main biochemical alterations distinguishing each category, peak detector was used to indicate the first few highest peaks in the loadings plots or cluster vectors plots.

Global DNA methylation in brain tissue determined by HPLC-MS

Brain tissue in zebrafish exposed to one of four CBNs at 0.1 mg L^{-1} were collected and stored in liquid nitrogen prior to DNA methylation analysis. DNA was extracted from tissue using the DNeasy tissue Kit (Tiangen, China) following the manufacturer's instructions. RNase A was added to columns in the kit to remove RNA residue. DNA hydrolysis was conducted using a mixture degradase kit (DNA Degradase Plus, Zymo Research, USA) following the manufacturer's protocol. To confirm complete hydrolysis of DNA, agarose gel electrophoresis was employed to test the result of the hydrolysis. The DNA hydrolysis mixtures were then stored at –20°C for mass spectrometric analysis.

To perform chromatographic separation, a Kinetex C_{18} column (100 mm × 4.6 mm, 2.6 µm; Phenomenex, USA) was employed in an HPLC system (LC-20AD, Shimadzu, Japan). The injection volume was 20 µL. The mobile phase consisted of water (A) and methanol (B). A gradient elution protocol was as follows: 0–0.01 min, 3% B; 0.01–5.00 min, 5% B; 3.00–12.00 min, 50% B; 12.00–15.00 min, 100% B; 15.00–25.00 min, 3% B at a flow rate of 0.5 mL min^{-1}. For the mass spectrometric analysis, an electrospray ionization tandem mass spectrometry (LCMS-8030, Shimadzu, Japan) system was used, operating in positive ionization mode and conditioned at a capillary temperature of 400°C and medium nitrogen curtain gas. Optimised multiple reaction monitoring conditions were set to evaluate dC from *m/z* 228.1 to 111.9 and 5 mdC from *m/z* 242.1 to 126.0. Data acquisition and processing were performed *via* Analyst software. The global DNA methylation ratio (MR) was determined by MR = [5 mdC]/([5 mdC] + [dC]).

The data are expressed as the mean ± SD. Significant differences among multiple groups were determined using a one-way analysis of variance (ANOVA) followed by Dunnett's *post hoc* tests. Probabilities of $P < 0.05$ were considered as statistically significant. All these tests were conducted in GraphPad Prism 4 (GraphPad Software, USA).

Results

Post-exposure to CBNs, tissues (brain, gonads and gastrointestinal tracts) were isolated from zebrafish (male and female). Isolation of lipids allowed for lipidomic analysis. PCA of the 90 samples (MCR-ALS relative lipid areas) are shown in Figure 2. The resultant scores plot indicates that effects produced are more pronounced on lipid extracts from gonads and intestinal tracts compared to brain. This is reflected by the higher data dispersion observed in the first two clusters (gonads and intestinal tracts) compared with the latter (i.e. brain).

It remains important to determine whether dietary exposure to CBNs results in exposure to distal and protected tissues such as brain. Figure 3 shows that in males, TAG and PC species behave similarly, showing a decrease in their intensities compared with the controls in C_{60}- and short MWCNT-exposed tissue samples (blue and violet, respectively), whereas there is an increase in these lipid species in SWCNT- and long MWCNT-exposed tissue samples (orange and dark green, respectively). However, no obvious effects in PC species are noted in CBN-exposed females. TAG species appear to be elevated in SWCNT-exposed samples (orange), but there is a slight decrease in their levels in short MWCNT- and long MWCNT-exposed samples (violet and dark green, respectively).

A major concern regarding CBN exposure would be with regard to the effects on reproductive health. In zebrafish, there appears to be male *versus* female differences in that PC and TAG species behave differently in males, whereas in females they exhibit a similar pattern (Figure 4). In males, TAG species appear to decrease in short MWCNT-exposed tissue samples (violet), but there is an apparent increase in C_{60}- and long MWCNT-exposed tissue samples (blue and dark green, respectively). PC species exhibit a marked increase in long MWCNT-exposed samples (dark green). In females, both TAG and PC lipids exhibit remarkable decreases in levels compared with the controls in SWCNT-exposed tissue samples (orange).

As a tissue that would readily come into contact with CBNs *via* dietary exposure, effects on lipid constituents in gastrointestinal tracts from male and female zebrafish were examined (Figure 5). In males, TAG species show decreases due to short MWCNT treatment (violet), whereas there are increases due to long MWCNT exposure (dark green). PC species exhibit a decrease caused by SWCNT or short MWCNT exposures (blue and dark green, respectively). In females, TAG species increase after C_{60} or long MWCNT exposure (blue and dark green, respectively), but appear decreased following short MWCNT treatment (violet). PC species are elevated after C_{60} or SWCNT exposures (pink and blue, respectively) and decreased post-exposure with short MWCNT or long MWCNT (violet and dark green, respectively).

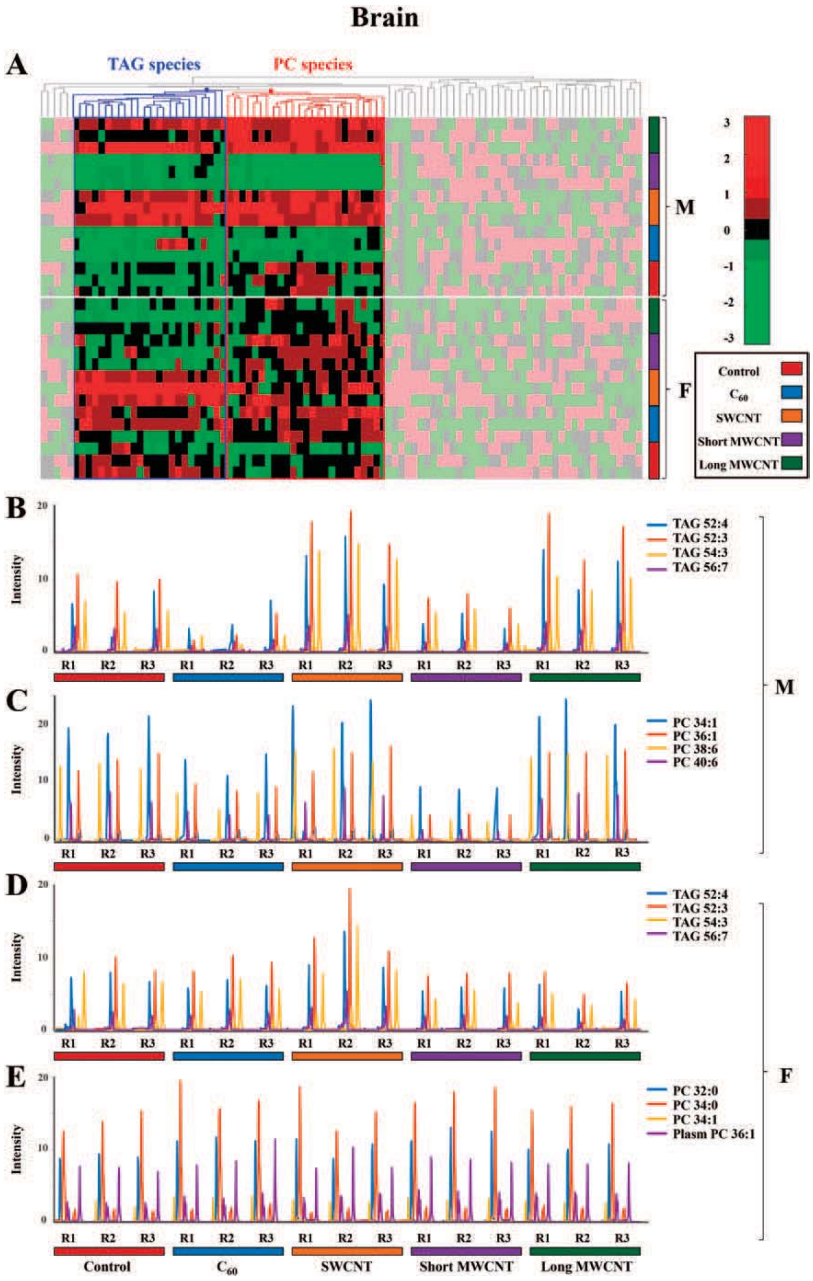

Figure 3. (**A**) Hierarchical clustering heatmap of the peak areas of the 94 identified lipid species in brain zebrafish samples (autoscaled data). Degree of change in the different stressed groups (C_{60}, SWCNT, short MWCNT and long MWCNT) compared with the control groups is marked with colours inside the heatmap indicating up-regulation (red) and down-regulation (green), as indicated by the colour bar at the top right of figure. Identified lipids are represented in the horizontal axis and sample groups in the vertical axis. Two clusters corresponding to glycerolipids (mainly TAG species) and glycerophospholipids (mainly PC species) are outlined. The decoloured parts of the heatmap correspond to lipid species showing no clear disrupting tendency. (**B** and **C**) Elution profiles of some representative TAG and PC lipid species, respectively, from male brain tissue samples exposed to CBNs. (**D** and **E**) Elution profiles of some representative TAG and PC lipid species, respectively, from female brain tissue samples exposed to CBNs. (F: female, M: male, R: replicate, 1 to 3: replicate number). The following colour legend for the distinct treatments is used: controls (deep red), C_{60} (blue), SWCNT (orange), short MWCNT (purple) and long MWCNT (dark green).

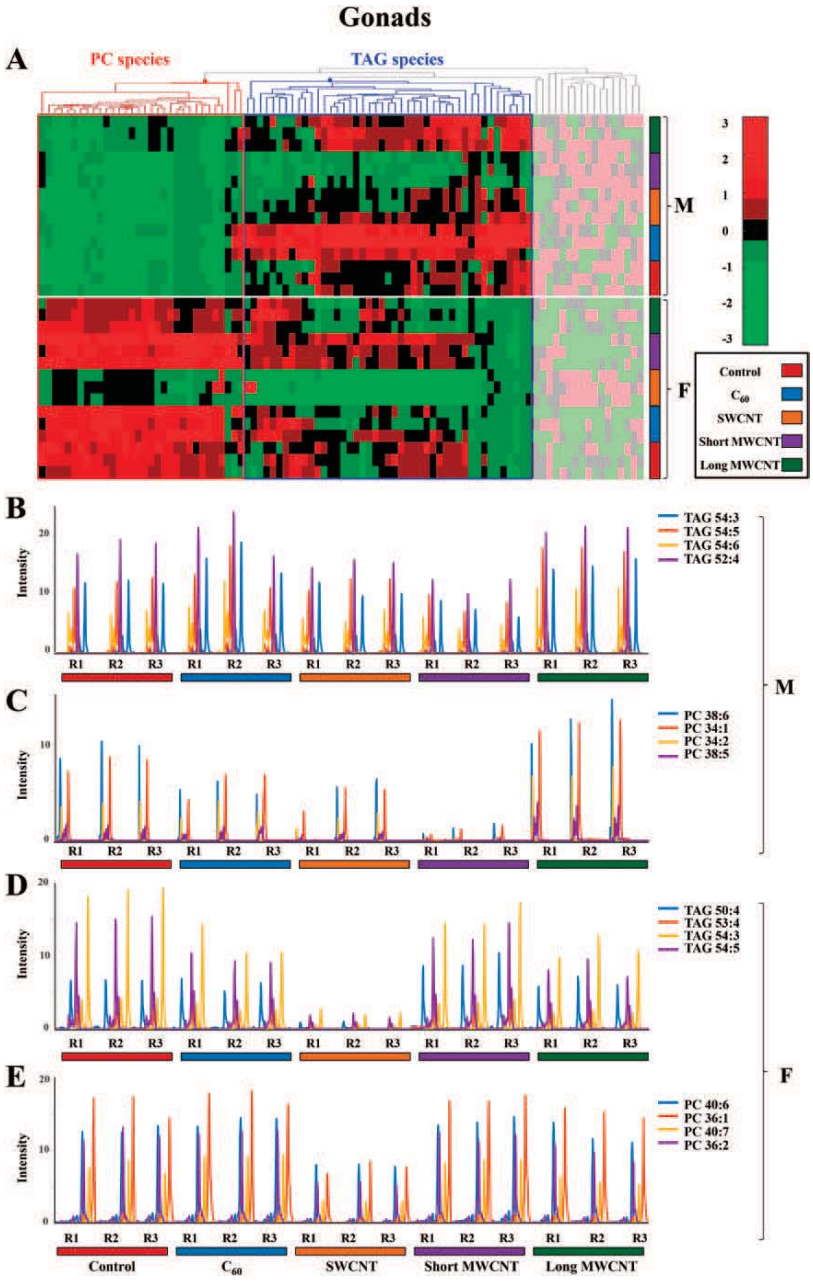

Figure 4. (**A**) Hierarchical clustering heatmap of the peak areas of the 94 identified lipid species in gonad zebrafish samples (autoscaled data). Degree of change in the different stressed groups (C_{60}, SWCNT, short MWCNT and long MWCNT) compared with the control groups is marked with colours indicating up-regulation (red) and down-regulation (green), as indicated by the colour bar at the top right of figure. Identified lipids are represented in the horizontal axis and sample groups in the vertical axis. Two clusters corresponding to glycerolipids (mainly TAG species) and glycerophospholipids (mainly PC species) are outlined. The decoloured parts of the heatmap correspond to lipid species showing no clear disrupting tendency. (**B** and **C**) Elution profiles of some representative TAG and PC lipid species, respectively, from male gonad tissue samples exposed to CBNs. (**D** and **E**) Elution profiles of some representative TAG and PC lipid species, respectively, from female gonad tissue samples exposed to CBNs. (F: female, M: male, R: replicate, 1 to 3: replicate number). The following colour legend for the distinct treatments is used: controls (deep red), C_{60} (blue), SWCNT (orange), short-MWCNT (purple) and long MWCNT (dark green).

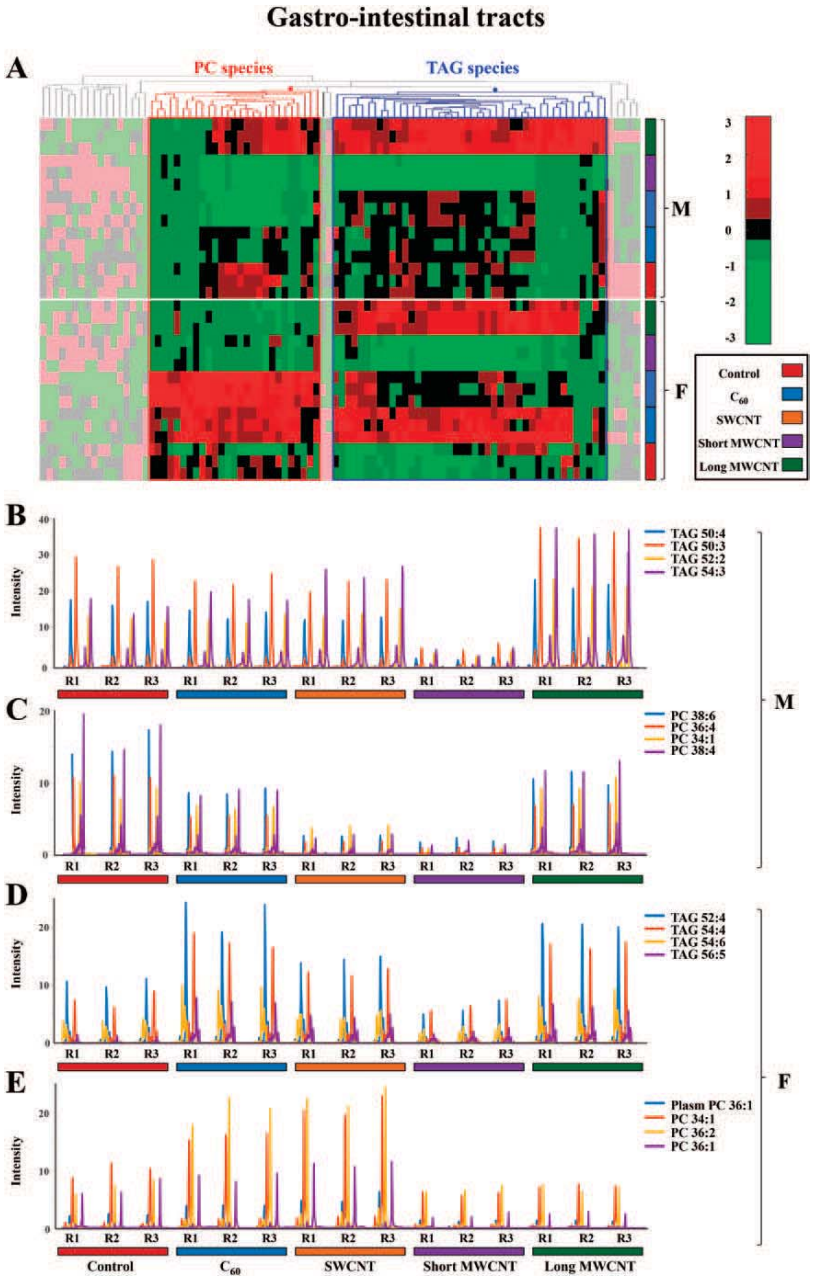

Figure 5. (**A**) Hierarchical clustering heatmap of the peak areas of the 94 identified lipid species in gastrointestinal tract zebrafish samples (autoscaled data). Degree of change in the different stressed groups (C_{60}, SWCNT, short MWCNT and long MWCNT) compared with the control groups is marked with colours inside the heatmap indicating up-regulation (red) and down-regulation (green), as indicated by the colour bar at the top right of figure. Identified lipids are represented in the horizontal axis, and sample groups in the vertical axis. Two clusters corresponding to glycerolipids (mainly TAG species) and glycerophospholipids (mainly PC species) are outlined. The decoloured parts of the heatmap correspond to lipid species showing no clear disrupting tendency. (**B** and **C**) Elution profiles of some representative TAG and PC lipid species, respectively, from male gastrointestinal tract tissue samples exposed to CBNs. (**D** and **E**) Elution profiles of some representative TAG and PC lipid species, respectively, from female gastrointestinal tract tissue samples exposed to CBNs. (F: female, M: male, R: replicate, 1 to 3: replicate number). The following colour legend for the distinct treatments is used: controls (deep red), C_{60} (blue), SWCNT (orange), short-MWCNT (purple) and long MWCNT (dark green).

To further examine CBN-induced effects in brain tissues of zebrafish, a SERS approach was employed (Figure 6). The preprocessed SERS spectra show that CBNs induce lipid alterations in both males and females, but there are obvious gender-specific differences. In both males and females, long MWCNTs appear to induce the most profound effects followed by SWCNTs as further evidenced by their cluster separation away from control in the resultant PCA-LDA scores plot (Figure 7A). Whilst clusters for C_{60} and short MWCNTs were still significantly removed away from the control cluster, they appear to co-locate and thus more likely to generate similar alterations. The cluster vector plots (Figure 7B) supported the notion that CBNs individually induced nanoparticle-specific profiles of alterations in males, whereas altered features in lipid extracts derived from female zebrafish brains were more similar. Table 1 shows the tentative wavenumber assignments associated with dietary CBN exposure; in females, there are consistent similarities although SWCNT-exposed differs from the other three treatments. This consistency is not mirrored in the highlighted tentative wavenumber alterations in CBN-exposed male zebrafish. In addition to the lipid alterations noted, there also appears to be consistent elevations in global genomic methylation; this was most profound in female zebrafish brain tissue samples following exposure to short MWCNTs and SWCNTs ($P < 0.05$; Figure 8).

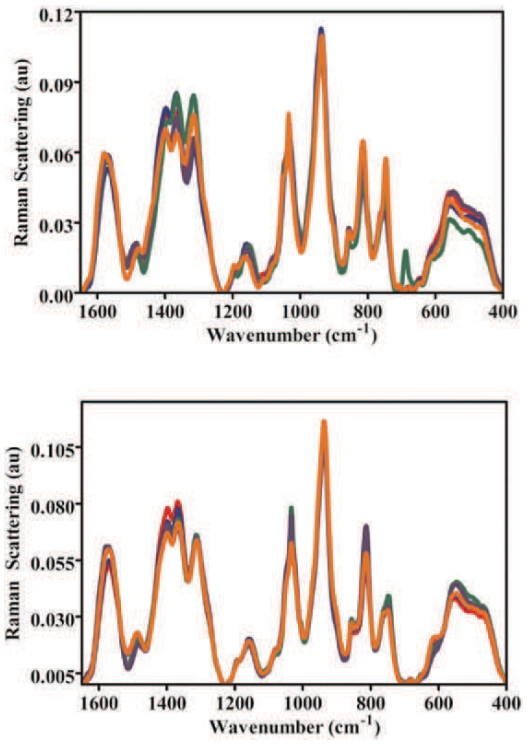

Figure 6. SERS spectra of lipid extracts of brain tissue from male (upper panel) and female (lower panel) zebrafish post-exposure with one of four CBNs. Fish (2 males and 2 females) exposures were conducted in 10 L glass tanks. CNP exposure (0.1 mg L^{-1}) was initiated and run for 21 days. Post-exposure and isolation of brain tissue, lipids were extracted; these were then mixed with Ag NPs prior to SERS. The spectral data were then inputted into MATLAB and preprocessed following wavelet de-noising, cut to 400–1800 cm^{-1}, second differentiation and vector normalisation. —, Control; —, C_{60} fullerene-treated; —, Long MWCNT-treated; —, Short MWCNT-treated; and, —, SWCNT-treated.

Discussion

Given the rising ubiquity of CBN environmental exposure, there is now an urgent need to assess risk under relevant conditions. Herein, we exposed male and female zebrafish to CBNs *via* their diet. Levels employed would be consistent with reasonable low environmental levels (38). Although mechanically disaggregated, CBN solutions would reasonably be expected to be stable, especially CNT solutions (29,39), although C_{60} would be more likely to agglomerate (40–42). We then examined the lipidomic profile of exposed *vs.* control in brain, gonads and gastrointestinal tissues. Whilst the liver acts as a portal to the body in many sentinel organisms (43), only in a small number of cases is it the target for consequent pathology. The tissues chosen in this study were chosen to determine whether CBNs possess potential to induce developmental alterations (i.e. brain) reproductive alterations (i.e. gonads) or point-of-contact alterations (i.e. gastrointestinal tract). From an exploratory study, marked alterations were noted (Figures 2 to 5). To confirm brain-associated alterations, an SERS approach was applied to the same lipid extracts and significant spectral alterations (Figures 6 and 7A) were noted associated with tentative chemical bonds (Figure 7B, Table 1). Interestingly, the observed lipidomic alterations in brain tissues using both approaches (i.e., LC-HRMS and SERS) were to some extent correlated. As evidenced in the scores plots obtained following SERS analysis (Figure 7A), treatments with long MWCNTs and SWCNTs produced most pronounced effects in both male and female brain tissues, whereas C_{60} and short MWCNTs treatments produced minor and similar alterations (co-located clusters in Figure 7A).

Accordingly, LC-MS lipid profiles of male brain tissues evidenced a large impact of long MWCNTs and SWCNTs, both producing an increment in TAG and PC lipid species, while there is a minor impact of C_{60} and short MWCNTs treatments, each behaving similarly and producing a diminution on TAG and PC lipid levels. Moreover, both SERS and LC-MS approaches evidenced that SWCNT treatment caused major alterations in female brain tissues, showing a discriminant pattern in comparison with the other treatments. Such distinguished effects caused by SWCNTs are noticeable in the cluster vectors plots resulting from the SERS approach (Figure 7B) but become even more evident in LC-MS TAG profiles of brain female samples represented in Figure 3D. In the latter Figure, it is readily observed that SWCNT treatment produces a significant increment in TAG species, while the other CBN treatments produce no significant alterations respect to controls.

Sparse evidence is found in the literature regarding the effects that CBNs can pose on lipid molecules of organisms. Little research in this direction has focused on the study of the interaction between CBNs and membrane lipids, such as PC species and their derivatives with plasmalogens. Rusciano *et al.* (44) investigated the interaction of organic carbon-based nanoparticles (NOC) with giant unilamellar vesicles, used as a model membrane, and suggested that ROS production induced by NOCs causes membrane peroxidation leading to the alteration of membrane permeability. Moreover, Engelmann *et al.* (45) suggested a direct linkage between the induced alterations on membrane lipids and the generation of ROS. Such connection is attributed to the reported capacity of plasmenyl-PCs to protect against the damaging effects of ROS, facilitating signalling processes and protecting membrane lipids from oxidation. In this study, a significant increase of PC species and derivatives was observed on brain male samples exposed to SWCNTs or long MWCNTs, on

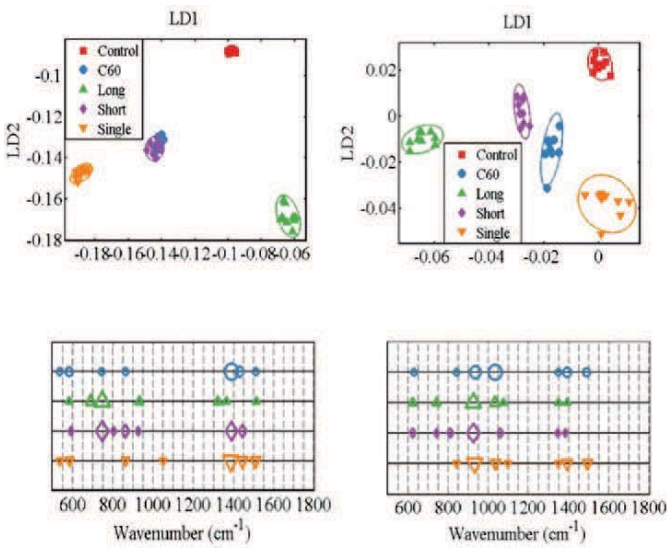

Figure 7. Scores plots and corresponding cluster vectors plots of brain tissue from male (left panels) and female (right panels). Fish (2 males and 2 females) exposures were conducted in 10 L glass tanks. CNP exposure (0.1 mg L^{-1}) was initiated and run for 21 days. Post-exposure and isolation of brain tissue, lipids were extracted; these were then mixed with Ag NPs prior to SERS. Following spectral preprocessing, computational analysis using the multivariate techniques of PCA and LDA were applied. Score plots show clusters for control (red squares), C_{60} fullerene-treated (blue diamond), long MWCNT-treated (green triangle), short MWCNT-treated (purple diamond) and SWCNT (inverted orange triangle). Cluster vectors plots indicate the top distinguishing wavenumbers associated with each CBN treatment compared with the control; symbol size is proportional to strength of alteration.

Table 1. Primary wavenumbers (ranked in order of importance) in cluster vectors derived from PCA-LDA of SERS spectral data sets.

	Female		Male	
CBN	Wavenumber (cm^{-1})	Tentative assignments	Wavenumber (cm^{-1})	Tentative assignments
C_{60} fullerene	1033	Phenylalanine	1387	CH_3
	932	C–C stretch	1430	CH_2 bending
	1393	CH_3	582	C–C twisting mode
	1488	CN stretch	743	C–S stretch
	838	O–P–O stretch	862	O–P–O stretch
	1346	CH	533	ν(S–S)
	626	C–C twisting mode	1510	ν(C=C)
Long MWCNTs	924	C–C stretch	745	C–S stretch
	1033	Phenylalanine	689	C–C twisting mode
	741	C–S stretch	930	C–C stretch
	621	C–C twisting mode	1321	CH
	1072	Chain C–C stretch	1364	CH_3
	1393	CH_3	1512	ν(C=C)
	1346	CH	580	ν(S–S)
Short MWCNTs	924	C–C stretch	745	C–S stretch
	1058	Chain C–C stretch	1387	CH_3
	807	O–P–O stretch	860	O–P–O stretch
	621	C–C twisting mode	1445	CH_2 bending
	741	C–S stretch	589	ν(S–S)
	1383	CH_3	924	C–C stretch
	1344	CH	803	O–P–O stretch
SWCNTs	930	C–C stretch	1385	CH_3
	1393	CH_3	1443	CH_2 bending
	1035	Phenylalanine	1510	ν(C=C)
	1494	CN stretch	862	O–P–O stretch
	838	O–P–O stretch	584	ν(S–S)
	1095	ν(C–N)	533	ν(S–S)
	1346	CH	1049	Phenylalanine

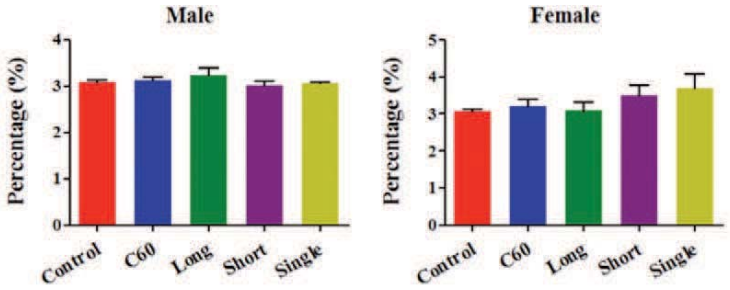

Global DNA methylation	Male		Female	
	Mean	SD	Mean	SD
Control	3.077	±0.05132	3.073	±0.04933
C_{60}	3.127	±0.06807	3.207	±0.1756
Long MWCNTs	3.233	±0.1604	3.077	±0.2250
Short MWCNTs	3.023	±0.08327	3.503	±0.2810
SWCNTs	3.063	±0.02887	3.693	±0.3884

The treatment *vs.* Control	*P*-value (ANOVA)	
	Male	Female
C_{60}	$P > 0.05$	$P > 0.05$
Long MWCNTs	$P > 0.05$	$P > 0.05$
Short MWCNTs	$P > 0.05$	$P > 0.05$
SWCNTs	$P > 0.05$	$P < 0.05$

Figure 8. Levels of genomic methylation in brain tissue of male or female zebrafish post-exposure with one of four CBNs. Fish (2 males and 2 females) exposures were conducted in 10 L glass tanks. CNP exposure (0.1 mg L^{-1}) was initiated and run for 21 days. Post-exposure and isolation of brain tissue, DNA methylation analysis was carried out.

gonad male samples exposed to long MWCNTs and on gastrointestinal female samples treated with C_{60} or SWCNTs. The increment of the amount of such membrane lipids can be attributed to a defence mechanism of the cellular membranes against CBN-induced oxidative stress. Concerning the effects that CBNs may have on lipid droplets, mainly formed by TAG and DAG species, no evidence currently exists in the literature. However, in this study, we have demonstrated the capacity of CBNs to alter TAG and DAG species in brain, gonad and gastrointestinal tissue samples of zebrafish. Further work would require extensive transmission electron microscopy studies to determine uptake and localisation of tissue-specific CBNs (46).

Finally, we examined whether CBN exposure might alter the levels of genomic methylation; despite expected *in vivo* heterogeneity, a consistent increase following CBN exposure is noted especially post-exposure with SWCNTs (Figure 8). Given the likely persistence of these agents, long-term exposure would likely lead to modifications that could alter development.

Overall, this work provides insights on the effects that CNTs or fullerenes can pose on lipids of female and male zebrafish (*Danio rerio*) at low environmentally relevant doses and highlights: (i) the ability of CBNs to induce marked lipid alterations in brain, gonads and gastrointestinal tissue samples of zebrafish; (ii) the response of membrane lipids against the oxidation damage induced by CBNs; and (iii) the capacity of CBNs to cause elevations in global genomic methylation, especially in female zebrafish tissue samples. Hence, this study proves that dietary exposures to low environmentally relevant levels of CBNs can induce far-reaching alterations in a range of tissues. These would likely be sublethal but could modify consequent susceptibility to other influences such as environmental exposures (47) and disease onset. There will be an increasing need for sophisticated data-handling approaches to tease out exposure-specific effect alterations in target cells following the application of omic approaches (47). Future studies are needed to explore the long-term consequences of these CBN exposures as well as their influence in combination with other environmental influences such as chemicals.

Supplementary data

Supplementary Tables 1 and 2 and Supplementary Figures 1 to 5 are available at *Mutagenesis* Online.

Funding

The research leading to these results has received funding from the European Research Council under the European Union's Seventh Framework Programme (FP/2007–2013)/ERC grant agreement no. 320737. One of the first authors (E.G.) acknowledges the Spanish Government (Ministerio de Educación, Cultura y Deporte) for a predoctoral FPU scholarship (FPU13/04384). Research in F.L.M.'s laboratory is supported by Rosemere Cancer Foundation and the Engineering and Physical Sciences Research Council (EPSRC; grant no: EP/K023349/1). Data relating to this study is deposited and freely available at: https://dx.doi.org/10.6084/m9.figshare.4012683.v1.

Conflict of interest statement: None declared.

References

1. Ema, M., Hougaard, K. S., Kishimoto, A. and Honda, K. (2016) Reproductive and developmental toxicity of carbon-based nanomaterials: a literature review. *Nanotoxicology*, 10, 391–412.
2. Li, J., Strong, R., Trevisan, J., Fogarty, S. W., Fullwood, N. J., Jones, K. C. and Martin, F. L. (2013) Dose-related alterations of carbon nanoparticles in mammalian cells detected using biospectroscopy: potential for real-world effects. *Environ. Sci. Technol.*, 47, 10005–10011.
3. Li, J., Tian, M., Cui, L., Dwyer, J., Fullwood, N. J., Shen, H. and Martin, F. L. (2016) Low-dose carbon-based nanoparticle-induced effects in A549 lung cells determined by biospectroscopy are associated with increases in genomic methylation. *Sci. Rep.*, 6, 20207.
4. Li, J., Ying, G. G., Jones, K. C. and Martin, F. L. (2015) Real-world carbon nanoparticle exposures induce brain and gonadal alterations in zebrafish (*Danio rerio*) as determined by biospectroscopy techniques. *Analyst*, 140, 2687–2695.
5. Oresic, M., Hänninen, V. A. and Vidal-Puig, A. (2008) Lipidomics: a new window to biomedical frontiers. *Trends Biotechnol.*, 26, 647–652.
6. van Meer, G. (2005) Cellular lipidomics. *EMBO J.*, 24, 3159–3165.
7. Jha, A. N. (2004) Genotoxicological studies in aquatic organisms: an overview. *Mutat. Res.*, 552, 1–17.
8. Jha, A. N. (2008) Ecotoxicological applications and significance of the comet assay. *Mutagenesis*, 23, 207–221.
9. Mustafa, S. A., Karieb, S. S., Davies, S. J. and Jha, A. N. (2015) Assessment of oxidative damage to DNA, transcriptional expression of key genes, lipid peroxidation and histopathological changes in carp *Cyprinus carpio* L. following exposure to chronic hypoxic and subsequent recovery in normoxic conditions. *Mutagenesis*, 30, 107–116.
10. Smolkova, B., El Yamani, N., Collins, A. R., Gutleb, A. C. and Dusinska, M. (2015) Nanoparticles in food. Epigenetic changes induced by nanomaterials and possible impact on health. *Food Chem. Toxicol.*, 77, 64–73.
11. Mirbahai, L. and Chipman, J. K. (2014) Epigenetic memory of environmental organisms: a reflection of lifetime stressor exposures. *Mutat. Res. Genet. Toxicol. Environ. Mutagen.*, 764–765, 10–17.
12. Vandegehuchte, M. B. and Janssen, C. R. (2014) Epigenetics in an ecotoxicological context. *Mutat. Res. Genet. Toxicol. Environ. Mutagen.*, 764–765, 36–45.
13. Wilson, I. D., Plumb, R., Granger, J., Major, H., Williams, R. and Lenz, E. M. (2005) HPLC-MS-based methods for the study of metabonomics. *J. Chromatogr. B. Analyt. Technol. Biomed. Life Sci.*, 817, 67–76.
14. Chadeau-Hyam, M., Campanella, G., Jombart, T., Bottolo, L., Portengen, L., Vineis, P., Liquet, B. and Vermeulen, R. C. (2013) Deciphering the complex: methodological overview of statistical models to derive OMICS-based biomarkers. *Environ. Mol. Mutagen.*, 54, 542–557.
15. Tauler, R. (1995) Multivariate curve resolution applied to second order data. *Chemom. Intell. Lab. Syst.*, 30, 133–146.
16. Farrés, M., Piña, B. and Tauler, R. (2015) Chemometric evaluation of Saccharomyces cerevisiae metabolic profiles using LC-MS. *Metabolomics*, 11, 210–224.
17. Gorrochategui, E., Casas, J., Porte, C., Lacorte, S. and Tauler, R. (2015) Chemometric strategy for untargeted lipidomics: biomarker detection and identification in stressed human placental cells. *Anal. Chim. Acta*, 854, 20–33.
18. Ortiz-Villanueva, E., Jaumot, J., Benavente, F., Piña, B., Sanz-Nebot, V. and Tauler, R. (2015) Combination of CE-MS and advanced chemometric methods for high-throughput metabolic profiling. *Electrophoresis*, 36, 2324–2335.
19. Bedia, C., Dalmau, N., Jaumot, J. and Tauler, R. (2015) Phenotypic malignant changes and untargeted lipidomic analysis of long-term exposed prostate cancer cells to endocrine disruptors. *Environ. Res.*, 140, 18–31.
20. de Juan, A., Jaumot, J. and Tauler, R. (2014) Multivariate Curve Resolution (MCR). Solving the mixture analysis problem. *Anal. Methods*, 6, 4964–4976.
21. Sánchez Pérez, I., Culzoni, M. J., Siano, G. G., Gil García, M. D., Goicoechea, H. C. and Martínez Galera, M. (2009) Detection of unintended stress effects based on a metabonomic study in tomato fruits after treatment with carbofuran pesticide. Capabilities of MCR-ALS applied to LC-MS three-way data arrays. *Anal. Chem.*, 81, 8335–8346.
22. Yi, L., Dong, N., Yun, Y., Deng, B., Ren, D., Liu, S. and Liang, Y. (2016) Chemometric methods in data processing of mass spectrometry-based metabolomics: a review. *Anal. Chim. Acta*, 914, 17–34.
23. Butler, H. J., Ashton, L., Bird, B., *et al.*(2016) Using Raman spectroscopy to characterize biological materials. *Nat. Protoc.*, 11, 664–687.
24. Trevisan, J., Park, J., Angelov, P. P., Ahmadzai, A. A., Gajjar, K., Scott, A. D., Carmichael, P. L. and Martin, F. L. (2014) Measuring similarity and improving stability in biomarker identification methods applied to Fourier-transform infrared (FTIR) spectroscopy. *J. Biophotonics*, 7, 254–265.
25. Riding, M. J., Trevisan, J., Hirschmugl, C. J., Jones, K. C., Semple, K. T. and Martin, F. L. (2012) Mechanistic insights into nanotoxicity determined by synchrotron radiation-based Fourier-transform infrared imaging and multivariate analysis. *Environ. Int.*, 50, 56–65.
26. Heys, K. A., Riding, M. J., Strong, R. J., Shore, R. F., Pereira, M. G., Jones, K. C., Semple, K. T. and Martin, F. L. (2014) Mid-infrared spectroscopic assessment of nanotoxicity in gram-negative vs. gram-positive bacteria. *Analyst*, 139, 896–905.
27. Patel, I. I., Harrison, W. J., Kerns, J. G., *et al.*(2012) Isolating stem cells in the inter-follicular epidermis employing synchrotron radiation-based Fourier-transform infrared microspectroscopy and focal plane array imaging. *Anal. Bioanal. Chem.*, 404, 1745–1758.
28. Patel, I. I., Trevisan, J., Evans, G., Llabjani, V., Martin-Hirsch, P. L., Stringfellow, H. F. and Martin, F. L. (2011) High contrast images of uterine tissue derived using Raman microspectroscopy with the empty modelling approach of multivariate curve resolution-alternating least squares. *Analyst*, 136, 4950–4959.
29. Kim, J. S., Song, K. S., Lee, J. H. and Yu, I. J. (2011) Evaluation of biocompatible dispersants for carbon nanotube toxicity tests. *Arch. Toxicol.*, 85, 1499–1508.
30. Gorrochategui, E., Jaumot, J. and Tauler, R. (2015) A protocol for LC-MS metabolomic data processing using chemometric tools. *Protoc. Exch.*, 10.1038/protex.2015.102, November 30, 2015.
31. Schonlau, M. (2004) Visualizing non-hierarchical and hierarchical cluster analyses with clustergrams. *Comput. Stat.*, 19, 95–111.
32. Gorrochategui, E., Casas, J., Pérez-Albaladejo, E., Jáuregui, O., Porte, C. and Lacorte, S. (2014) Characterization of complex lipid mixtures in contaminant exposed JEG-3 cells using liquid chromatography and high-resolution mass spectrometry. *Environ. Sci. Pollut. Res. Int.*, 21, 11907–11916.
33. Cui, L., Yao, M., Ren, B. and Zhang, K. S. (2011) Sensitive and versatile detection of the fouling process and fouling propensity of proteins on polyvinylidene fluoride membranes via surface-enhanced Raman spectroscopy. *Anal. Chem.*, 83, 1709–1716.
34. Cui, L., Chen, P., Chen, S., Yuan, Z., Yu, C., Ren, B. and Zhang, K. (2013) In situ study of the antibacterial activity and mechanism of action of silver nanoparticles by surface-enhanced Raman spectroscopy. *Anal. Chem.*, 85, 5436–5443.

35. Trevisan, J., Angelov, P. P., Scott, A. D., Carmichael, P. L. and Martin, F. L. (2013) IRootLab: a free and open-source MATLAB toolbox for vibrational biospectroscopy data analysis. *Bioinformatics*, 29, 1095–1097.
36. Butler, H. J., Fogarty, S. W., Kerns, J. G., Martin-Hirsch, P. L., Fullwood, N. J. and Martin, F. L. (2015) Gold nanoparticles as a substrate in bio-analytical near-infrared surface-enhanced Raman spectroscopy. *Analyst*, 140, 3090–3097.
37. Martin, F. L., German, M. J., Wit, E., Fearn, T., Ragavan, N. and Pollock, H. M. (2007) Identifying variables responsible for clustering in discriminant analysis of data from infrared microspectroscopy of a biological sample. *J. Comput. Biol.*, 14, 1176–1184.
38. Mueller, N. C. and Nowack, B. (2008) Exposure modeling of engineered nanoparticles in the environment. *Environ. Sci. Technol.*, 42, 4447–4453.
39. Jiang, J., Oberdörster, G. and Biswas, P. (2009) Characterization of size, surface charge, and agglomeration state of nanoparticle dispersions for toxicological studies. *J. Nanopart. Res.*, 11 77–89.
40. Deguchi, S., Alargova, R. G. and Tsujii, K. (2001) Stable dispersions of fullerenes, C_{60} and C_{70}, in water. Preparation and characterization. *Langmuir*, 17, 6013–6017.
41. Brant, J., Lecoanet, H., Hotze, M. and Wiesner, M. (2005) Comparison of electrokinetic properties of colloidal fullerenes (n-C60) formed using two procedures. *Environ. Sci. Technol.*, 39, 6343–6351.
42. Dhawan, A., Taurozzi, J. S., Pandey, A. K., Shan, W., Miller, S. M., Hashsham, S. A. and Tarabara, V. V. (2006) Stable colloidal dispersions of C60 fullerenes in water: evidence for genotoxicity. *Environ. Sci. Technol.*, 40, 7394–7401.
43. Llabjani, V., Crosse, J. D., Ahmadzai, A. A., Patel, I. I., Pang, W., Trevisan, J., Jones, K. C., Shore, R. F. and Martin, F. L. (2011) Differential effects in mammalian cells induced by chemical mixtures in environmental biota as profiled using infrared spectroscopy. *Environ. Sci. Technol.*, 45, 10706–10712.
44. Rusciano, G., De Luca, A. C., Pesce, G. and Sasso, A. (2009) On the interaction of nano-sized organic carbon particles with model lipid membranes. *Carbon N. Y.*, 47, 2950–2957.
45. Engelmann, B., Bräutigam, C. and Thiery, J. (1994) Plasmalogen phospholipids as potential protectors against lipid peroxidation of low density lipoproteins. *Biochem. Biophys. Res. Commun.*, 204, 1235–1242.
46. Rhiem, S., Riding, M. J., Baumgartner, W., Martin, F. L., Semple, K. T., Jones, K. C., Schäffer, A. and Maes, H. M. (2015) Interactions of multiwalled carbon nanotubes with algal cells: quantification of association, visualization of uptake, and measurement of alterations in the composition of cells. *Environ. Pollut.*, 196, 431–439.
47. Gorrochategui, E., Lacorte, S., Tauler, R. and Martin, F. L. (2016) Perfluoroalkylated substance effects in *Xenopus laevis* A6 kidney epithelial cells determined by ATR-FTIR spectroscopy and chemometric analysis. *Chem. Res. Toxicol.*, 29, 924–932.

SUPPLEMENTARY MATERIAL OF SCIENTIFIC ARTICLE IX

Diet-sourced carbon-based nanoparticles induce lípid alterations in tissues of zebrafish (Danio rerio) with genòmic hypermethylation changes in brain

E. Gorrochategui, J. Li, N.J. Fullwood, G.G. Ying, M. Tian, L. Cui, H. Shen, S. Lacorte, R. Tauler, F.L. Martin

Mutagenesis (2017) **32 (1)**, 91-103

Figure S1. LC-MS profiles once imported into MATLAB environment and after compression and data matrix construction. Example shown for lipid extracts from control brain, gonads and gastro-intestinal tracts of female zebrafish.

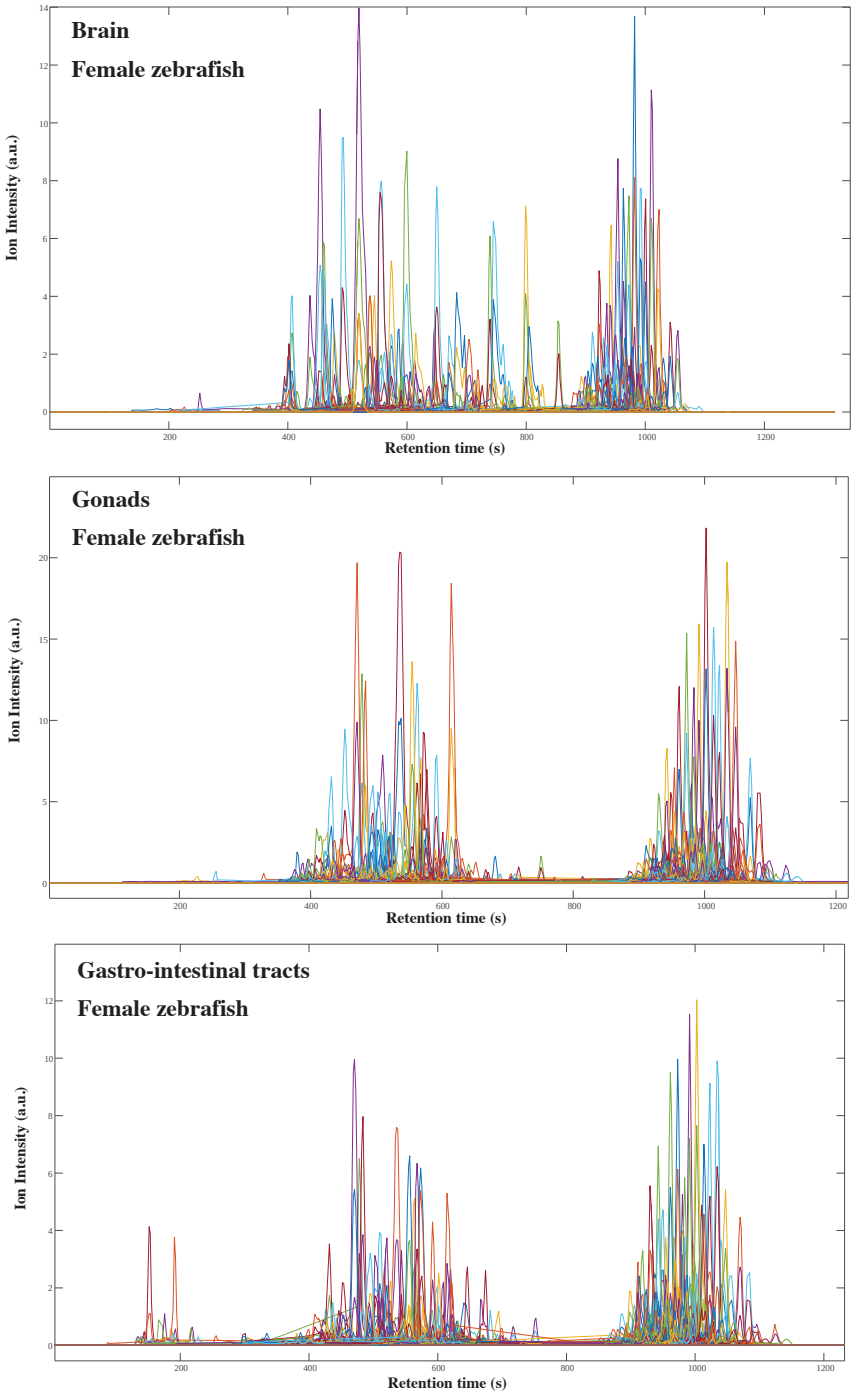

Figure S2. Augmented LC-MS data matrices of brain samples (Control, C_{60}, SWCNT, short MWCNT and long MWCNT) of female and male zebrafish.

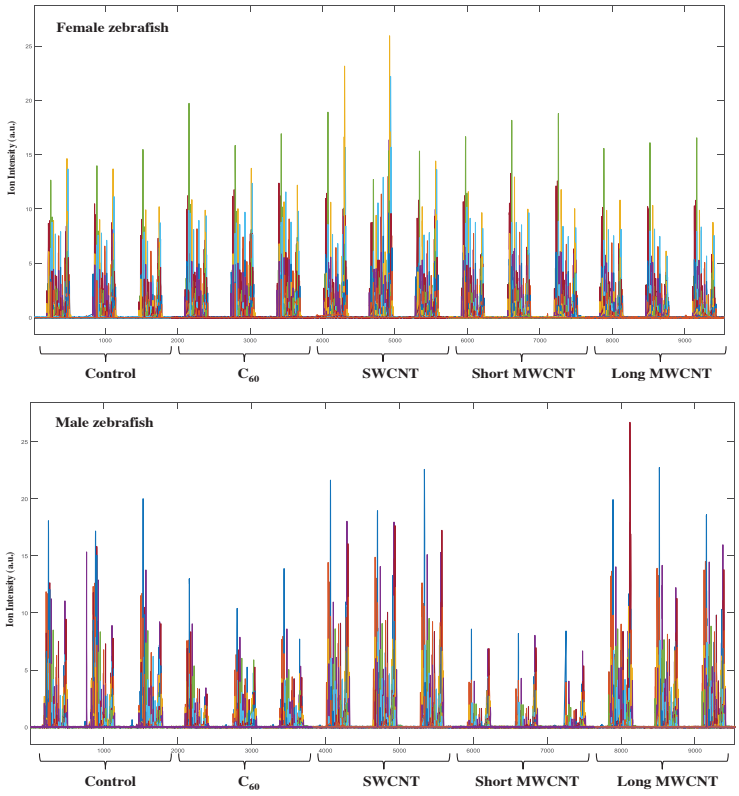

Figure S3. Final augmented LC-MS data matrix containing information of the 90 samples analysed. Input matrix for further MCR-ALS analysis.

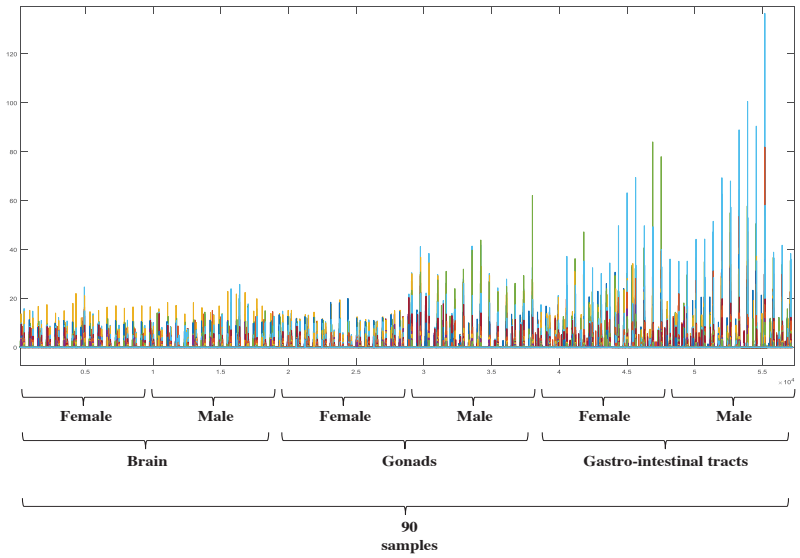

Figure S4. A) Output of MCR-ALS analysis of the final augmented data matrix to find purest elution and mass spectra profiles. 150 components resolved, explaining 99.2% of data variance. **B)** Example of elution and spectra profiles for component 2 in the 90 samples.

A]

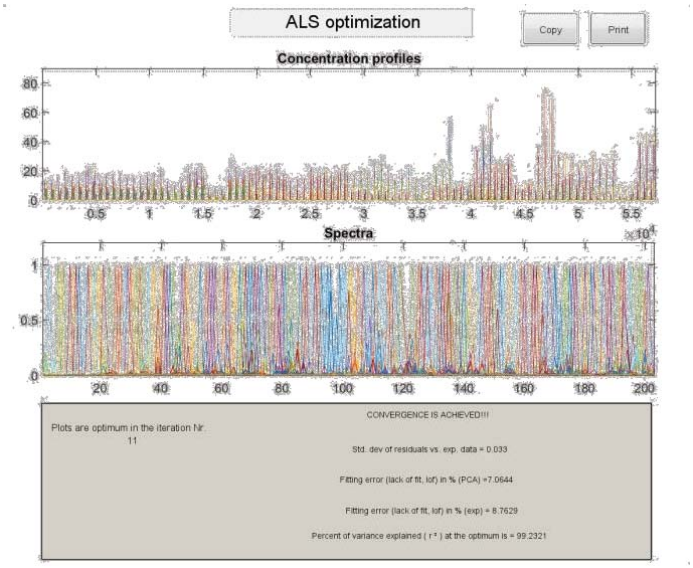

B]

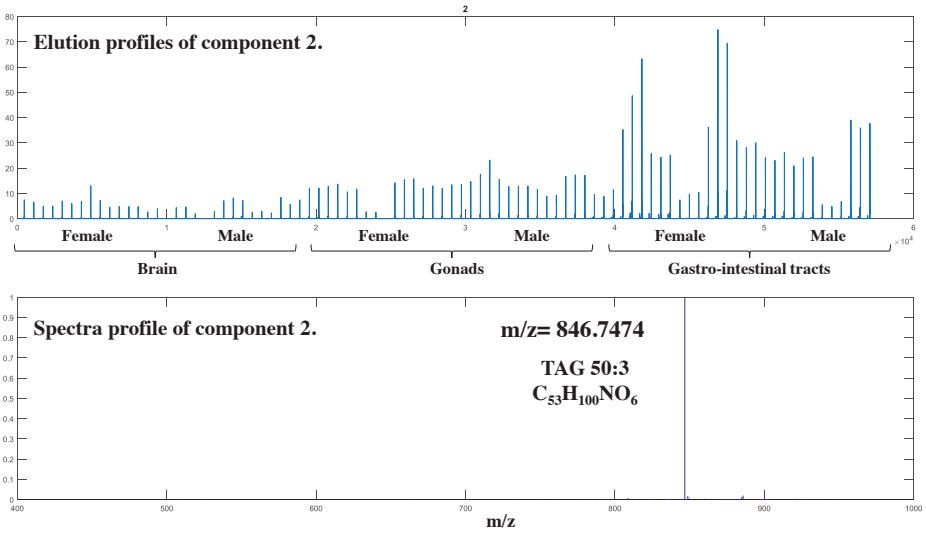

Figure S5. A) PLS-DA scores plot for control and C_{60}-stressed samples of brain tissues of female zebrafish**. B)** Variables importance in projection (VIP scores) plot from PLS-DA analysis of the 94 lipid species. Horitzontal red line show the threshold values of 1 (dotted line) lipid species in red indicate most important variables according to the highest threshold value (potential biomarkers). (* Lipid species also showing significant differences among controls and stressed samples in the two-sample Student's *t*-Test ($P < 0.05$)).

A]

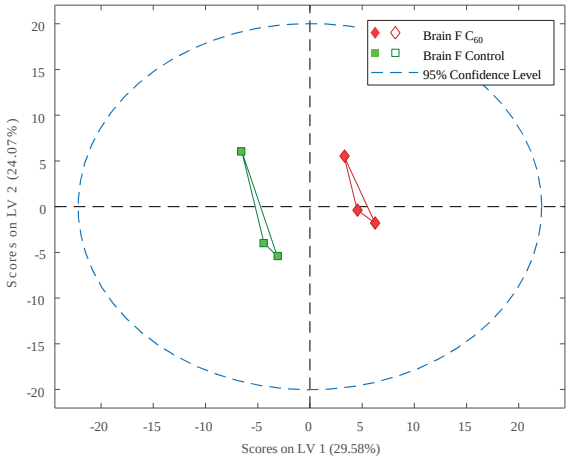

B]

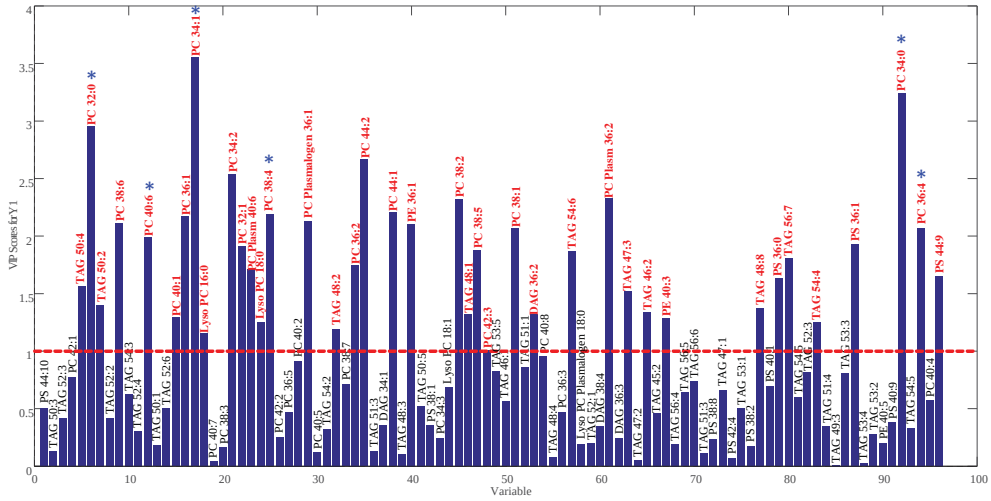

Table S1. Potential biomarkers for lipid disruption in distinct tissues of zebrafish exposed to carbon-based nanoparticles. Lipid species in stressed samples showing significant down- or up- regulation respect to controls were determined by PLS-DA analyses (VIP > 1) and further two-sample Student's *t*-Test ($P < 0.05$). (See Section 2.5. in the manuscript).

Lipid specie	Lipid classification	Fold-change[a]	*p*-values[b]	Up(+)/down(-) regulation
BRAIN FEMALE				
C_{60}-treatment				
PC 32:0	Glycerophospholipid	1.27	0.00433	+
PC 34:0	Glycerophospholipid	1.24	0.04483	+
PC 34:1	Glycerophospholipid	1.24	0.00070	+
PC 36:4	Glycerophospholipid	2.52	0.03353	+
PC 38:4	Glycerophospholipid	2.18	0.04557	+
PC 40:6	Glycerophospholipid	1.21	0.02364	+
SWCNT-treatment				
PC 34:1	Glycerophospholipid	1.23	0.02501	+
Short MWCNT-treatment				
PC 32:0	Glycerophospholipid	1.24	0.02088	+
PC 34:0	Glycerophospholipid	1.20	0.01347	+
PC 34:1	Glycerophospholipid	1.26	0.00054	+
Plasmalogen PC 36:1	Glycerophospholipid	1.21	0.03517	+
PS 44:9	Glycerophospholipid	1.67	0.04574	-
TAG 52:3	Glycerolipid	1.90	0.04651	+
TAG 52:4	Glycerolipid	1.67	0.03786	+
TAG 54:3	Glycerolipid	1.38	0.04367	+
Long MWCNT-treatment				
PC 34:1	Glycerophospholipid	1.13	0.02182	+
Plasmalogen PC 36:1	Glycerophospholipid	1.28	0.00584	+
TAG 54:2	Glycerolipid	1.50	0.02358	-
TAG 54:3	Glycerolipid	1.59	0.04319	-
BRAIN MALE				
C_{60}-treatment				
PC 32:0	Glycerophospholipid	1.65	0.03755	-
PC 32:1	Glycerophospholipid	1.27	0.04428	-
PC 34:0	Glycerophospholipid	1.41	0.00615	-
PC 34:1	Glycerophospholipid	1.36	0.01910	-
PC 36:1	Glycerophospholipid	1.42	0.00498	-
PC 40:1	Glycerophospholipid	1.58	0.02230	-
PC 40:6	Glycerophospholipid	1.41	0.02480	-
PE 36:1	Glycerophospholipid	1.23	0.01975	-
TAG 52:3	Glycerolipid	4.92	0.00453	-
SWCNT-treatment				

PC 32:0	Glycerophospholipid	1.07	0.04442	+
PC 36:2	Glycerophospholipid	1.60	0.00027	+
PC 38:2	Glycerophospholipid	1.40	0.01532	+
PC 38:6	Glycerophospholipid	1.28	0.02924	+
PC 42:1	Glycerophospholipid	2.06	0.02671	+
Plasmalogen PC 36:1	Glycerophospholipid	1.49	0.00824	+
PE 36:1	Glycerophospholipid	1.22	0.00659	+
TAG 48:2	Glycerolipid	1.34	0.03339	+
TAG 50:1	Glycerolipid	1.20	0.00340	+
TAG 52:3	Glycerolipid	1.73	0.03941	+
TAG 54:3	Glycerolipid	2.05	0.01670	+
Short MWCNT-treatment				
PC 36:1	Glycerophospholipid	3.32	0.00028	-
PC 36:4	Glycerophospholipid	9.28	0.04385	-
PC 38:2	Glycerophospholipid	4.61	0.00746	-
PC 38:6	Glycerophospholipid	5.40	0.00251	-
PC 42:2	Glycerophospholipid	4.40	0.00042	-
Plasmalogen PC 36:1	Glycerophospholipid	3.08	0.00260	-
Plasmalogen PC 36:2	Glycerophospholipid	2.76	0.00565	-
PE 36:1	Glycerophospholipid	5.43	0.00917	-
PE 40:5	Glycerophospholipid	10.77	0.00033	-
TAG 48:2	Glycerolipid	2.97	0.02315	-
TAG 51:2	Glycerolipid	1.30	0.00391	-
TAG 56:7	Glycerolipid	1.94	0.00459	-
Long MWCNT-treatment				
PC 34:0	Glycerophospholipid	1.19	0.00390	+
PC 34:1	Glycerophospholipid	1.25	0.01552	+
PC 36:1	Glycerophospholipid	1.20	0.04961	+
PC 38:2	Glycerophospholipid	1.5	0.02783	+
PC 38:4	Glycerophospholipid	1.82	0.04112	+
PC 40:1	Glycerophospholipid	2.27	0.04875	+
PC 40:6	Glycerophospholipid	1.16	0.01137	+
PC 42:1	Glycerophospholipid	2.17	0.00094	+
PC 42:2	Glycerophospholipid	1.39	0.49028	+
PC 44:2	Glycerophospholipid	3.37	0.00698	+
Plasmalogen PC 36:1	Glycerophospholipid	1.56	0.00654	+
PS 40:9	Glycerophospholipid	2.42	0.04645	+
PS 44:9	Glycerophospholipid	1.68	0.02099	+
TAG 48:2	Glycerolipid	1.43	0.00403	+
TAG 50:1	Glycerolipid	1.19	0.02154	+
TAG 51:1	Glycerolipid	1.32	0.03486	+
TAG 52:4	Glycerolipid	2.21	0.00919	+
TAG 54:2	Glycerolipid	1.37	0.03118	+
TAG 54:5	Glycerolipid	3.09	0.01760	+
GONAD FEMALE				
C_{60}-treatment				
PC 38:4	Glycerophospholipid	1.32	0.00941	+
PC 40:4	Glycerophospholipid	1.67	0.01783	+
PC 40:5	Glycerophospholipid	1.61	0.01354	+

Plasmalogen PC 36:1	Glycerophospholipid	1.28	0.04628	+
Plasmalogen PC 36:2	Glycerophospholipid	1.05	0.00628	-
Plasmalogen PC 40:6	Glycerophospholipid	1.28	0.01150	+
PE 36:1	Glycerophospholipid	1.14	0.01093	+
TAG 46:1	Glycerolipid	1.41	0.04471	+
TAG 48:1	Glycerolipid	1.71	0.04178	+
TAG 52:2	Glycerolipid	1.22	0.04604	-
TAG 54:4	Glycerolipid	1.34	0.01140	-
TAG 54:5	Glycerolipid	1.60	0.01531	-
TAG 54:6	Glycerolipid	1.15	0.02472	-
TAG 56:6	Glycerolipid	1.38	0.02793	-
SWCNT-treatment				
PC 32:0	Glycerophospholipid	1.65	0.01017	-
PC 34:3	Glycerophospholipid	4.15	0.02982	-
PC 36:5	Glycerophospholipid	5.10	0.01138	-
PC 38:3	Glycerophospholipid	2.51	0.00188	-
PC 38:4	Glycerophospholipid	1.71	0.00623	-
PC 38:7	Glycerophospholipid	5.25	0.01556	-
PC 40:5	Glycerophospholipid	1.82	0.00681	-
PC 40:6	Glycerophospholipid	1.91	0.00395	-
PC 40:7	Glycerophospholipid	2.00	0.01548	-
PC 40:8	Glycerophospholipid	4.18	0.02038	-
Plasmalogen PC 36:1	Glycerophospholipid	1.82	0.00513	-
Plasmalogen PC 36:2	Glycerophospholipid	2.33	0.00619	-
Plasmalogen PC 40:6	Glycerophospholipid	1.76	0.00524	-
PE 36:1	Glycerophospholipid	1.81	0.00852	-
PS 36:0	Glycerophospholipid	1.99	0.02070	-
PS 38:8	Glycerophospholipid	1.73	0.00401	-
TAG 48:1	Glycerolipid	1.85	0.02626	-
TAG 48:2	Glycerolipid	4.08	0.00712	-
TAG 50:2	Glycerolipid	3.91	0.00813	-
TAG 50:4	Glycerolipid	6.22	0.00036	-
TAG 50:5	Glycerolipid	4.27	0.01845	-
TAG 51:1	Glycerolipid	2.64	0.00747	-
TAG 52:6	Glycerolipid	9.47	0.00125	-
TAG 53:4	Glycerolipid	10.27	0.03470	-
TAG 54:3	Glycerolipid	7.24	0.00139	-
TAG 54:5	Glycerolipid	4.85	0.00121	-
Short MWCNT-treatment				
PC 38:4	Glycerophospholipid	1.35	0.01163	+
PC 38:5	Glycerophospholipid	1.20	0.01885	+
PC 38:7	Glycerophospholipid	1.72	0.03684	+
PC 40:4	Glycerophospholipid	1.97	0.02234	+
PC 40:5	Glycerophospholipid	1.5	0.02276	+
Plasmalogen PC 36:1	Glycerophospholipid	1.34	0.02652	+
PE 36:1	Glycerophospholipid	1.44	0.03396	+
PS 40:9	Glycerophospholipid	1.22	0.03952	+
TAG 48:1	Glycerolipid	1.62	0.00595	+
TAG 48:2	Glycerolipid	1.58	0.01842	+
TAG 50:5	Glycerolipid	1.63	0.00283	+
TAG 52:3	Glycerolipid	1.16	0.01998	+

TAG 54:2	Glycerolipid	1.20	0.04159	-
Long MWCNT-treatment				
PC 38:7	Glycerophospholipid	1.57	0.01038	-
PC 34:0	Glycerophospholipid	1.17	0.03019	-
PC 34:3	Glycerophospholipid	1.38	0.01775	-
PC 38:3	Glycerophospholipid	1.32	0.01569	-
PC 40:8	Glycerophospholipid	1.35	0.02246	-
Plasmalogen PC 36:2	Glycerophospholipid	1.25	0.03679	-
PE 40:3	Glycerophospholipid	1.25	0.01265	-
PS 44:9	Glycerophospholipid	1.47	0.03745	-
PS 44:10	Glycerophospholipid	1.53	0.04856	-
TAG 46:1	Glycerolipid	1.66	0.02385	+
TAG 48:1	Glycerolipid	2.19	0.01589	+
TAG 48:2	Glycerolipid	1.71	0.01393	+
TAG 48:8	Glycerolipid	1.86	0.03248	-
TAG 52:2	Glycerolipid	1.30	0.03318	-
TAG 53:2	Glycerolipid	1.38	0.03547	-
TAG 53:3	Glycerolipid	2.08	0.01287	-
TAG 54:3	Glycerolipid	1.50	0.01735	-
TAG 54:4	Glycerolipid	1.67	0.01082	-
TAG 54:5	Glycerolipid	1.60	0.01728	-
TAG 54:6	Glycerolipid	1.43	0.03137	-
TAG 56:5	Glycerolipid	2.20	0.00394	-
TAG 56:7	Glycerolipid	1.60	0.03255	-
GONAD MALE				
C_{60}-treatment				
PC 34:3	Glycerophospholipid	1.38	0.01775	-
PS 44:9	Glycerophospholipid	1.47	0.03745	-
PS 44:10	Glycerophospholipid	1.53	0.04856	-
TAG 48:1	Glycerolipid	2.19	0.01588	+
TAG 48:2	Glycerolipid	1.71	0.01392	+
TAG 46:1	Glycerolipid	1.66	0.02385	+
TAG 52:2	Glycerolipid	1.30	0.03318	-
TAG 53:2	Glycerolipid	1.38	0.03547	-
TAG 53:3	Glycerolipid	2.08	0.01287	-
TAG 54:3	Glycerolipid	1.50	0.01735	-
TAG 54:4	Glycerolipid	1.67	0.01082	-
TAG 54:5	Glycerolipid	1.60	0.01725	-
TAG 54:6	Glycerolipid	1.43	0.03137	+
TAG 56:5	Glycerolipid	2.19	0.00394	-
SWCNT-treatment				
PC 34:3	Glycerophospholipid	1.38	0.01775	-
PC 38:7	Glycerophospholipid	1.57	0.01038	-
PS 44:9	Glycerophospholipid	1.47	0.03745	-
TAG 46:1	Glycerolipid	1.66	0.02385	+
TAG 48:1	Glycerolipid	2.19	0.01589	+
TAG 48:2	Glycerolipid	1.71	0.01393	+
TAG 48:8	Glycerolipid	1.86	0.03248	-
TAG 52:2	Glycerolipid	1.30	0.03318	-

TAG 54:3	Glycerolipid	1.50	0.01736	-
TAG 54:4	Glycerolipid	1.67	0.01082	-
TAG 54:5	Glycerolipid	2.24	0.00261	-
TAG 54:6	Glycerolipid	1.44	0.03137	-
TAG 56:5	Glycerolipid	2.20	0.00393	-
TAG 56:7	Glycerolipid	1.60	0.03255	-
Short MWCNT-treatment				
PC 34:1	Glycerophospholipid	7.67	0.00705	-
PC 34:2	Glycerophospholipid	1.79	0.02747	-
PC 36:4	Glycerophospholipid	2.89	0.01655	-
PC 38:5	Glycerophospholipid	3.48	0.01722	-
PC 38:6	Glycerophospholipid	7.24	0.00164	-
TAG 45:2	Glycerolipid	2.97	0.02125	-
TAG 46:1	Glycerolipid	1.45	0.01502	-
TAG 47:2	Glycerolipid	1.60	0.00619	-
TAG 47:3	Glycerolipid	2.89	0.01534	-
TAG 48:1	Glycerolipid	1.43	0.02177	-
TAG 51:3	Glycerolipid	1.12	0.04120	-
TAG 52:3	Glycerolipid	1.45	0.04158	-
TAG 54:5	Glycerolipid	1.49	0.04263	-
TAG 56:6	Glycerolipid	2.63	0.00001	-
TAG 56:7	Glycerolipid	3.15	0.03554	-
Long MWCNT-treatment				
PC 32:0	Glycerophospholipid	1.89	0.01584	+
PC 34:1	Glycerophospholipid	1.75	0.02775	+
PC 34:2	Glycerophospholipid	2.02	0.01267	+
PC 36:2	Glycerophospholipid	3.87	0.02230	+
PC 36:3	Glycerophospholipid	3.08	0.00047	+
PC 36:5	Glycerophospholipid	3.50	0.02086	+
PC 38:4	Glycerophospholipid	3.64	0.00095	+
PC 38:5	Glycerophospholipid	1.95	0.00705	+
PC 38:6	Glycerophospholipid	1.55	0.02194	+
PC 40:6	Glycerophospholipid	2.91	0.00048	+
Plasmalogen PC 40:6	Glycerophospholipid	2.73	0.00059	+
PS 44:9	Glycerophospholipid	1.25	0.00657	+
TAG 48:8	Glycerolipid	1.66	0.04382	-
TAG 52:3	Glycerolipid	1.20	0.01093	+
TAG 54:3	Glycerolipid	1.38	0.00789	+
TAG 54:5	Glycerolipid	1.36	0.01044	+
TAG 54:6	Glycerolipid	1.34	0.04136	+
TAG 56:7	Glycerolipid	1.20	0.03363	-
GASTRO-INTESTINAL TRACT FEMALE				
C_{60}-treatment				
32:0	Glycerophospholipid	1.59	0.01646	+
PC 34:1	Glycerophospholipid	1.49	0.01489	+
PC 36:2	Glycerophospholipid	3.04	0.00327	+
PC 38:5	Glycerophospholipid	3.33	0.01694	+
Plasmalogen PC 36:1	Glycerophospholipid	2.05	0.01539	+
Plasmalogen PC 36:2	Glycerophospholipid	1.74	0.04366	+

PS 36:0	Glycerophospholipid	2.69	0.01864	+
PS 36:1	Glycerophospholipid	5.50	0.01236	+
PS 38:1	Glycerophospholipid	3.32	0.00129	+
PS 40:1	Glycerophospholipid	3.48	0.00475	-
PS 40:9	Glycerophospholipid	2.39	0.01905	+
PS 42:4	Glycerophospholipid	2.97	0.02799	+
PS 44:10	Glycerophospholipid	2.20	0.02911	+
TAG 54:2	Glycerolipid	2.38	0.00423	+
DAG 34:1	Glycerolipid	1.78	0.02749	-
TAG 53:5	Glycerolipid	2.80	0.00608	+
TAG 46:1	Glycerolipid	1.90	0.03871	+
TAG 47:1	Glycerolipid	2.91	0.03802	+
TAG 49:3	Glycerolipid	3.67	0.00569	+
TAG 50:3	Glycerolipid	3.96	0.01189	+
TAG 50:5	Glycerolipid	3.16	0.00987	+
TAG 51:2	Glycerolipid	2.34	0.04958	+
TAG 51:3	Glycerolipid	3.65	0.07862	+
TAG 51:4	Glycerolipid	5.02	0.01363	+
TAG 52:2	Glycerolipid	1.85	0.03951	+
TAG 52:3	Glycerolipid	12.98	0.01306	+
TAG 52:4	Glycerolipid	2.28	0.01526	+
TAG 52:6	Glycerolipid	6.71	0.03478	+
TAG 53:3	Glycerolipid	2.19	0.03406	+
TAG 53:4	Glycerolipid	4.67	0.01247	+
TAG 54:4	Glycerolipid	2.36	0.00968	+
TAG 54:5	Glycerolipid	2.05	0.03297	-
TAG 54:6	Glycerolipid	1.91	0.02795	+
TAG 56:5	Glycerolipid	6.16	0.00343	+
TAG 56:6	Glycerolipid	3.71	0.01635	+
SWCNT-treatment				
PC 34:1	Glycerophospholipid	1.71	0.02575	+
PC 36:1	Glycerophospholipid	1.46	0.39146	+
PC 40:4	Glycerophospholipid	3.53	0.00142	+
PC 40:5	Glycerophospholipid	4.25	0.01664	+
Plasmalogen PC 36:1	Glycerophospholipid	1.78	0.01726	+
Plasmalogen PC 36:2	Glycerophospholipid	1.97	0.01636	+
PS 36:1	Glycerophospholipid	8.62	0.02691	+
PS 38:1	Glycerophospholipid	2.14	0.00478	+
PS 38:8	Glycerophospholipid	3.49	0.06795	-
TAG 52:3	Glycerolipid	10.24	0.00050	+
TAG 52:4	Glycerolipid	1.42	0.00948	+
TAG 54:3	Glycerolipid	3.01	0.00417	+
TAG 54:4	Glycerolipid	1.60	0.01738	+
TAG 54:5	Glycerolipid	2.40	0.01902	-
TAG 54:6	Glycerolipid	1.36	0.00410	+
TAG 56:5	Glycerolipid	4.74	0.00167	+
TAG 56:6	Glycerolipid	3.88	0.00384	+
TAG 56:7	Glycerolipid	3.26	0.00811	+
DAG 34:1	Glycerolipid	1.45	0.03137	-
Short MWCNT-treatment				
PC 34:1	Glycerophospholipid	1.96	0.03000	-
PC 36:1	Glycerophospholipid	2.81	0.01082	-

PC 40:4	Glycerophospholipid	1.43	0.00448	-
Plasmalogen PC 36:1	Glycerophospholipid	1.65	0.00316	-
Plasmalogen PC 36:2	Glycerophospholipid	2.52	0.02248	-
PS 36:1	Glycerophospholipid	2.48	0.02339	+
PS 38:8	Glycerophospholipid	5.45	0.04351	-
PS 40:1	Glycerophospholipid	9.20	0.04185	-
TAG 50:3	Glycerolipid	1.39	0.03074	-
TAG 52:3	Glycerolipid	4.15	0.02796	+
TAG 52:4	Glycerolipid	1.76	0.00970	-
TAG 54:5	Glycerolipid	2.07	0.02286	-
DAG 34:1	Glycerolipid	1.81	0.01293	-
TAG 54:6	Glycerolipid	1.47	0.01632	-
TAG 56:5	Glycerolipid	2.42	0.02334	+
TAG 56:6	Glycerolipid	2.54	0.01408	+
TAG 56:7	Glycerolipid	2.06	0.01472	+
Long MWCNT-treatment				
PC 32:0	Glycerophospholipid	1.36	0.04101	-
PC 40:4	Glycerophospholipid	2.79	0.01009	-
Plasmalogen PC 36:2	Glycerophospholipid	2.38	0.01989	-
PS 38:1	Glycerophospholipid	3.50	0.00037	+
PS 38:8	Glycerophospholipid	5.67	0.04532	-
PS 40:9	Glycerophospholipid	2.00	0.02944	+
PS 44:9	Glycerophospholipid	2.32	0.03354	+
PS 44:10	Glycerophospholipid	2.13	0.01615	+
TAG 46:1	Glycerolipid	1.99	0.02461	+
TAG 47:1	Glycerolipid	3.34	0.03561	+
TAG 48:2	Glycerolipid	1.54	0.03932	+
TAG 49:3	Glycerolipid	3.02	0.00902	+
TAG 50:1	Glycerolipid	1.95	0.00810	+
TAG 50:2	Glycerolipid	1.83	0.03918	+
TAG 50:3	Glycerolipid	4.89	0.04333	+
TAG 50:4	Glycerolipid	2.91	0.00496	+
TAG 51:2	Glycerolipid	2.39	0.00818	+
TAG 52:3	Glycerolipid	10.73	0.00073	+
TAG 52:4	Glycerolipid	2.24	0.00008	+
TAG 52:6	Glycerolipid	3.13	0.02218	+
TAG 53:3	Glycerolipid	2.11	0.00316	+
TAG 53:4	Glycerolipid	4.30	0.00081	+
TAG 54:3	Glycerolipid	4.44	0.01160	+
TAG 54:4	Glycerolipid	2.26	0.00465	+
TAG 54:5	Glycerolipid	2.03	0.00199	-
TAG 54:6	Glycerolipid	1.70	0.00022	+
TAG 56:5	Glycerolipid	5.52	0.00061	+
TAG 56:6	Glycerolipid	2.81	0.00618	+
TAG 56:7	Glycerolipid	2.76	0.00657	+
GASTRO-INTESTINAL TRACT MALE				
C_{60}-treatment				
PC 36:4	Glycerophospholipid	1.95	0.01961	-
PC 38:4	Glycerophospholipid	1.66	0.02040	-
PC 38:5	Glycerophospholipid	1.80	0.02324	-
PC 38:6	Glycerophospholipid	1.80	0.02874	-

PC 40:6	Glycerophospholipid	1.81	0.02861	-
PC 40:7	Glycerophospholipid	1.96	0.00392	-
Lyso PC 16:0	Glycerophospholipid	7.75	0.00313	-
Lyso PC 18:0	Glycerophospholipid	4.87	0.03126	-
Lyso PC 18:1	Glycerophospholipid	9.49	0.00317	-
Plasmalogen PC 40:6	Glycerophospholipid	1.59	0.01805	-
Lyso Plasmalogen	Glycerophospholipid	3.85	0.03956	-
PC 18:0	Glycerophospholipid	1.67	0.01297	-
PS 36:1	Glycerophospholipid	1.19	0.03138	-
PS 38:1	Glycerophospholipid	2.78	0.03726	+
PS 38:8	Glycerophospholipid	1.32	0.02609	-
TAG 48:2	Glycerolipid	1.24	0.03685	-
TAG 50:4	Glycerolipid	1.22	0.03497	-
TAG 53:3	Glycerolipid	1.23	0.02224	+
TAG 54:2	Glycerolipid	1.26	0.01678	-
SWCNT-treatment				
PC 34:1	Glycerophospholipid	2.31	0.00227	-
PC 34:2	Glycerophospholipid	3.36	0.03373	-
PC 36:1	Glycerophospholipid	1.91	0.03183	-
PC 36:3	Glycerophospholipid	2.33	0.00074	-
PC 36:4	Glycerophospholipid	6.61	0.00505	-
PC 36:5	Glycerophospholipid	12.06	0.04318	-
PC 38:4	Glycerophospholipid	6.10	0.00786	-
PC 38:5	Glycerophospholipid	6.24	0.00820	-
PC 38:6	Glycerophospholipid	5.66	0.01963	-
PC 40:6	Glycerophospholipid	6.49	0.00893	-
PC 40:7	Glycerophospholipid	3.78	0.00209	-
Lyso PC 16:0	Glycerophospholipid	4.96	0.01989	-
Lyso PC 18:0	Glycerophospholipid	4.67	0.01783	-
Lyso PC 18:1	Glycerophospholipid	2.20	0.02408	-
Plasmalogen PC 40:6	Glycerophospholipid	3.71	0.00248	-
Lyso PlasmalogenPC	Glycerophospholipid	2.84	0.03156	-
18:0	Glycerophospholipid	2.91	0.00497	-
PE 40:3	Glycerophospholipid	10.03	0.00210	-
PE 40:5	Glycerophospholipid	14.40	0.00854	-
PS 36:1	Glycerophospholipid	1.19	0.04901	-
PS 38:1	Glycerophospholipid	1.52	0.00047	+
PS 44:9	Glycerophospholipid	1.29	0.03589	+
PS 44:10	Glycerophospholipid	1.34	0.00457	-
TAG 48:1	Glycerolipid	1.48	0.04321	-
TAG 48:2	Glycerolipid	1.21	0.02779	-
TAG 50:3	Glycerolipid	1.44	0.01904	+
TAG 54:2	Glycerolipid	1.54	0.00677	+
TAG 54:3	Glycerolipid	1.22	0.04494	+
TAG 54:4	Glycerolipid	1.06	0.01246	+
TAG 54:5	Glycerolipid	1.09	0.00416	-
TAG 54:6	Glycerolipid	1.65	0.02853	+
TAG 56:5	Glycerolipid	1.60	0.04519	+
TAG 56:6				
Short MWCNT-treatment				
PC 34:1	Glycerophospholipid	27.47	0.00229	-

PC 34:2	Glycerophospholipid	4.43	0.03245	-
PC 36:1	Glycerophospholipid	3.01	0.00792	-
PC 36:3	Glycerophospholipid	3.84	0.00369	-
PC 36:4	Glycerophospholipid	8.10	0.00451	-
PC 38:4	Glycerophospholipid	13.32	0.01111	-
PC 38:5	Glycerophospholipid	7.02	0.01184	-
PC 38:6	Glycerophospholipid	11.44	0.01856	-
PC 40:6	Glycerophospholipid	6.46	0.00925	-
PC 40:7	Glycerophospholipid	3.77	0.00215	-
Lyso PC 16:0	Glycerophospholipid	4.88	0.02344	-
Lyso PC 18:0	Glycerophospholipid	4.60	0.01923	-
Lyso PC 18:1	Glycerophospholipid	1.97	0.03230	-
Plasmalogen PC 40:6	Glycerophospholipid	7.52	0.01188	-
Lyso PlasmalogenPC	Glycerophospholipid	2.59	0.03737	-
18:0	Glycerophospholipid	3.67	0.00305	-
PE 40:3	Glycerophospholipid	2.96	0.03828	-
PE 40:5	Glycerophospholipid	3.39	0.00534	-
PS 36:1	Glycerophospholipid	1.98	0.00244	-
PS 38:1	Glycerophospholipid	14.79	0.01355	-
PS 40:9	Glycerophospholipid	6.81	0.02182	-
PS 44:9	Glycerophospholipid	4.34	0.00105	-
PS 44:10	Glycerolipid	1.32	0.01048	-
TAG 47:3	Glycerolipid	2.46	0.00168	-
TAG 48:1	Glycerolipid	5.68	0.00313	-
TAG 48:2	Glycerolipid	6.21	0.00050	-
TAG 50:3	Glycerolipid	5.92	0.00426	-
TAG 50:4	Glycerolipid	3.96	0.00075	-
TAG 51:2	Glycerolipid	3.09	0.01463	-
TAG 52:2	Glycerolipid	9.32	0.00982	-
TAG 52:6	Glycerolipid	2.94	0.04794	-
TAG 53:1	Glycerolipid	3.30	0.01236	-
TAG 53:2	Glycerolipid	3.07	0.00719	-
TAG 53:5	Glycerolipid	2.60	0.00590	-
TAG 54:2	Glycerolipid	3.76	0.00738	-
TAG 54:3	Glycerolipid	4.22	0.00156	-
TAG 54:4	Glycerolipid	4.00	0.00026	-
TAG 54:6	Glycerolipid	6.36	0.01149	-
TAG 56:5	Glycerolipid	2.44	0.02166	-
TAG 56:6	Glycerolipid	3.80	0.00316	-
TAG 56:7				
Long MWCNT-treatment				
PC 36:3	Glycerophospholipid	1.36	0.00763	-
PC 38:5	Glycerophospholipid	1.50	0.01597	-
Lyso PC 16:0	Glycerophospholipid	1.91	0.00313	+
Lyso PC 18:0	Glycerophospholipid	3.90	0.00550	-
Lyso PC 18:1	Glycerophospholipid	3.80	0.00700	-
Plasmalogen PC 36:1	Glycerophospholipid	3.81	0.00366	+
Plasmalogen PC 36:2	Glycerophospholipid	2.88	0.00017	+
PS 36:1	Glycerophospholipid	1.25	0.04929	-
PS 38:1	Glycerophospholipid	1.24	0.02154	+
PS 38:2	Glycerophospholipid	3.68	0.00346	+
PS 42:4	Glycerophospholipid	2.12	0.00304	+
PS 44:9	Glycerophospholipid	2.26	0.00078	+
PS 44:10	Glycerophospholipid	3.54	0.00574	-

TAG 46:1	Glycerolipid	2.02	0.00927	+
TAG 46:2	Glycerolipid	4.01	0.00226	+
TAG 47:1	Glycerolipid	3.05	0.03412	+
TAG 47:2	Glycerolipid	3.14	0.00454	+
TAG 48:4	Glycerolipid	3.68	0.00601	+
TAG 48:8	Glycerolipid	1.95	0.02620	+
TAG 50:1	Glycerolipid	1.53	0.01396	+
TAG 50:2	Glycerolipid	1.69	0.00846	+
TAG 50:3	Glycerolipid	1.27	0.00192	+
TAG 50:4	Glycerolipid	1.21	0.03187	+
TAG 50:5	Glycerolipid	1.65	0.00774	+
TAG 51:1	Glycerolipid	1.40	0.03999	+
TAG 51:2	Glycerolipid	1.39	0.02665	+
TAG 52:2	Glycerolipid	2.09	0.00846	+
TAG 52:3	Glycerolipid	2.18	0.04763	+
TAG 52:4	Glycerolipid	1.56	0.00083	+
TAG 52:6	Glycerolipid	1.82	0.02020	+
TAG 53:1	Glycerolipid	2.04	0.04333	+
TAG 53:2	Glycerolipid	2.10	0.01378	+
TAG 53:3	Glycerolipid	1.44	0.02969	+
TAG 53:4	Glycerolipid	2.01	0.04109	+
TAG 53:5	Glycerolipid	1.31	0.03052	+
TAG 54:2	Glycerolipid	2.35	0.01541	+
TAG 54:3	Glycerolipid	2.43	0.01820	+
TAG 54:4	Glycerolipid	1.84	0.00142	+
TAG 54:5	Glycerolipid	1.56	0.00559	+
TAG 54:6	Glycerolipid	1.43	0.00271	+
TAG 56:5	Glycerolipid	1.97	0.00279	+
TAG 56:6	Glycerolipid	2.16	0.00177	+
TAG 56:7	Glycerolipid	1.66	0.00239	+
DAG 34:1	Glycerolipid	3.71	0.00020	+
DAG 36:2	Glycerolipid	3.87	0.00292	+
DAG 36:3	Glycerolipid	2.90	0.02318	+

[a]Fold change- mean of stressed-samples/mean of control samples.
[b]*p*-value- Significance levels for the two-sample Student's *t*-Test were computed for assessing the significance between stressed and control samples.

Table S2. Elemental composition of glycerophospholipid and glycerolipid species found in brain, gonad and gastro-intestinal tract tissues of zebrafish, calculated by mass accuracy within error of 10 ppm, with atom constraints and with -0.5 ≤ DBE ≤ 15.0. DBE: double-bond equivalent. Elemental composition of PC, Plasmalogen PC, Lyso PC, Lyso Plasmalogen PC and PE refer to the $[M+H]^+$ ions whereas TAG, DAG and PS refer to ammonium adducts $[M + NH_4]^+$. Lipid species were detected under ESI (+) using an UHPLC system coupled to a TOF analyzer with an Acquity UPLC BEH C_8 column (1.7 µm particle size, 100 mm x 2.1 mm).

GLYCEROPHOSPHOLIPIDS						
Lipid subclass	**Lipid specie**	**Measured mass (Da)**	**Elemental composition**	**Calculated mass (Da)**	**Error (ppm)**	**DBE**
PC						
	32:0	734.5750	$C_{40}H_{81}NO_8P$	734.5694	7.6	1.5
	32:1	732.5600	$C_{40}H_{79}NO_8P$	732.5538	8.5	2.5
	34:0	762.6013	$C_{42}H_{85}NO_8P$	762.6007	0.8	1.5
	34:1	760.5900	$C_{42}H_{83}NO_8P$	760.5851	6.4	2.5
	34:2	758.5760	$C_{42}H_{81}NO_8P$	758.5694	8.7	3.5
	34:3	756.5613	$C_{42}H_{79}NO_8P$	756.5538	9.9	4.5
	36:1	788.6234	$C_{44}H_{87}NO_8P$	788.6164	8.9	2.5
	36:2	786.6085	$C_{44}H_{85}NO_8P$	786.6007	9.9	3.5
	36:3	784.5890	$C_{44}H_{83}NO_8P$	784.5851	5.0	4.5
	36:4	782.5760	$C_{44}H_{81}NO_8P$	782.5694	8.4	5.5
	36:5	780.5600	$C_{44}H_{79}NO_8P$	780.5538	7.9	6.5
	38:1	816.6543	$C_{46}H_{91}NO_8P$	816.6478	8.0	2.5
	38:2	814.6400	$C_{46}H_{89}NO_8P$	814.6320	9.8	3.5
	38:3	812.6200	$C_{46}H_{87}NO_8P$	812.6164	4.4	4.5
	38:4	810.6057	$C_{46}H_{85}NO_8P$	810.6007	6.2	5.5
	38:5	808.5897	$C_{46}H_{83}NO_8P$	808.5851	5.7	6.5
	38:6	806.5620	$C_{46}H_{81}NO_8P$	806.5694	-9.2	7.5
	38:7	804.5600	$C_{46}H_{79}NO_8P$	804.5537	7.8	8.5
	40:1	844.6864	$C_{48}H_{95}NO_8P$	844.6790	8.8	1.5
	40:2	842.6706	$C_{48}H_{93}NO_8P$	842.6633	8.7	3.5
	40:4	838.6339	$C_{48}H_{89}NO_8P$	838.6320	2.3	5.5
	40:5	836.6189	$C_{48}H_{87}NO_8P$	836.6164	3.0	6.5
	40:6	834.6052	$C_{48}H_{85}NO_8P$	834.6007	5.4	7.5
	40:7	832.5900	$C_{48}H_{83}NO_8P$	832.5850	6.0	8.5
	40:8	830.5733	$C_{48}H_{81}NO_8P$	830.5694	4.7	9.5
	42:1	872.7190	$C_{50}H_{99}NO_8P$	872.7102	10.0	2.5
	42:2	870.7000	$C_{50}H_{97}NO_8P$	870.6946	6.2	3.5
	42:3	868.6840	$C_{50}H_{95}NO_8P$	868.6790	5.8	4.5
	44:1	900.7500	$C_{52}H_{103}NO_8P$	900.7415	9.4	1.5
	44:2	898.7349	$C_{52}H_{101}NO_8P$	898.7259	10.0	2.5
Plasmalogen PC						
	36:1	774.6292	$C_{44}H_{89}NO_7P$	774.6371	-10.0	1.5
	36:2	772.6143	$C_{44}H_{87}NO_7P$	772.6215	-9.4	2.5
	40:6	820.6140	$C_{48}H_{87}NO_7P$	820.6215	-9.1	6.5
Lyso PC						

	16:0	496.3390	$C_{24}H_{51}NO_7P$	496.3398	1.6	0.5
	18:0	524.3671	$C_{26}H_{55}NO_7P$	524.3711	7.6	0.5
	18:1	522.3540	$C_{26}H_{53}NO_7P$	522.3554	2.7	1.5
Lyso plasmalogen PC						
	18:0	510.3877	$C_{26}H_{57}NO_6P$	510.3918	-8.0	-0.5
PE						
	36:1	746.5760	$C_{41}H_{81}NO_8P$	746.5694	8.8	2.5
	40:3	796.5916	$C_{45}H_{83}NO_8P$	796.5851	8.2	5.5
	40:5	792.5607	$C_{45}H_{79}NO_8P$	792.5538	8.7	7.5
PS						
	36:0	809.5970	$C_{42}H_{86}N_2O_{10}P$	809.6015	5.5	1.5
	36:1	807.5830	$C_{42}H_{84}N_2O_{10}P$	807.5858	3.5	2.5
	38:1	835.7672	$C_{44}H_{88}N_2O_{10}P$	835.6172	5.4	2.5
	38:2	833.6100	$C_{44}H_{86}N_2O_{10}P$	833.6015	10.0	3.5
	38:8	821.5160	$C_{44}H_{74}N_2O_{10}P$	821.5076	10.2	9.5
	40:1	863.6399	$C_{46}H_{92}N_2O_{10}P$	863.6485	10.0	2.5
	40:9	847.514	$C_{46}H_{76}N_2O_{10}P$	847.5232	10.8	10.5
	42:4	885.6416	$C_{48}H_{90}N_2O_{10}P$	885.6328	9.9	5.5
	44:9	903.5950	$C_{50}H_{84}N_2O_{10}P$	903.5859	10.1	10.5
	44:10	901.5800	$C_{50}H_{82}N_2O_{10}P$	901.5702	10.8	11.5
GLYCEROLIPIDS						
TAG						
	45:2	778.6974	$C_{48}H_{92}NO_6$	778.6919	7.1	3.5
	46:1	794.7294	$C_{49}H_{96}NO_6$	794.7232	7.8	2.5
	46:2	792.7143	$C_{49}H_{94}NO_6$	792.7076	8.5	3.5
	47:1	808.7431	$C_{50}H_{98}NO_6$	808.7389	5.2	2.5
	47:2	806.7280	$C_{50}H_{96}NO_6$	806.7233	5.8	3.5
	47:3	804.7125	$C_{50}H_{94}NO_6$	804.7076	6.1	4.5
	48:1	822.7606	$C_{51}H_{100}NO_6$	822.7545	7.4	2.5
	48:2	820.7442	$C_{51}H_{98}NO_6$	820.7389	6.5	3.5
	48:3	818.7262	$C_{51}H_{96}NO_6$	818.7232	3.7	4.5
	48:4	816.7102	$C_{51}H_{94}NO_6$	816.7076	3.2	5.5
	48:8	812.6800	$C_{51}H_{90}NO_6$	812.6763	4.6	9.5
	49:3	832.7365	$C_{52}H_{98}NO_6$	832.7389	-2.9	4.5
	50:1	850.7940	$C_{53}H_{104}NO_6$	850.7858	9.6	2.5
	50:2	848.7766	$C_{53}H_{102}NO_6$	848.7702	7.5	3.5
	50:3	846.7574	$C_{53}H_{100}NO_6$	846.7545	3.4	4.5
	50:4	844.7467	$C_{53}H_{98}NO_6$	844.7389	9.2	5.5
	50:5	842.7294	$C_{53}H_{96}NO_6$	842.7232	7.4	6.5
	51:1	864.8091	$C_{54}H_{106}NO_6$	864.8015	8.8	2.5
	51:2	862.7926	$C_{54}H_{104}NO_6$	862.7864	7.2	3.5
	51:3	860.7731	$C_{54}H_{102}NO_6$	860.7702	3.4	4.5
	51:4	858.7611	$C_{54}H_{100}NO_6$	858.7546	7.6	5.5
	52:1	878.8242	$C_{55}H_{108}NO_6$	878.8171	8.1	2.5
	52:2	876.8089	$C_{55}H_{106}NO_6$	876.8015	8.4	3.5
	52:3	874.7910	$C_{55}H_{104}NO_6$	874.7858	5.9	4.5
	52:4	872.7783	$C_{55}H_{102}NO_6$	872.7702	9.3	5.5
	52:6	868.7460	$C_{55}H_{98}NO_6$	868.7389	8.2	7.5
	53:1	892.8400	$C_{56}H_{110}NO_6$	892.8328	8.1	2.5
	53:2	890.8250	$C_{56}H_{108}NO_6$	890.8172	8.8	3.5
	53:3	888.8049	$C_{56}H_{106}NO_6$	888.8015	3.8	4.5

	53:4	886.7896	$C_{56}H_{104}NO_6$	886.7859	4.2	5.5
	53:5	884.7771	$C_{56}H_{102}NO_6$	884.7702	7.8	6.5
	54:2	904.8401	$C_{57}H_{110}NO_6$	904.8328	8.0	3.5
	54:3	902.8207	$C_{57}H_{108}NO_6$	902.8171	4.0	4.5
	54:4	900.8074	$C_{57}H_{106}NO_6$	900.8015	6.5	5.5
	54:5	898.7938	$C_{57}H_{104}NO_6$	898.7858	8.9	6.5
	54:6	896.7789	$C_{57}H_{102}NO_6$	896.7702	9.7	7.5
	56:4	928.8354	$C_{59}H_{110}NO_6$	928.8328	2.8	5.5
	56:5	926.8208	$C_{59}H_{108}NO_6$	926.8172	3.9	6.5
	56:6	924.8084	$C_{59}H_{106}NO_6$	924.8015	7.6	7.5
	56:7	922.7940	$C_{59}H_{104}NO_6$	922.7859	8.8	8.5
DAG						
	34:1	612.5569	$C_{37}H_{74}NO_5$	612.5562	1.1	1.5
	36:2	638.5718	$C_{39}H_{76}NO_5$	638.5718	0.0	2.5
	36:3	636.5604	$C_{39}H_{74}NO_5$	636.5562	6.6	3.5
	38:4	662.5718	$C_{41}H_{76}NO_5$	662.5718	0.0	4.5

4.3. DISCUSSION OF RESULTS

In this Section of the discussion of results, the findings obtained in the study of the effects of some xenobiotics in two distinct biological systems used for environmental assessment are presented. First, the effects of four PFASs (*i.e.*, PFBS, PFOA, PFOS and PFNA) on the *Xenopus laevis* A6 kidney epithelial cell line, used as a toxicological model to simulate effects on amphibians, are discussed. Secondly, the alterations produced in three distinct tissues (*i.e.*, brain, gonads and intestinal tracts) of male and female zebrafish (*Danio rerio*) after exposure to four CBNs (*i.e.*, C_{60}, SWCNTs, short MWCNTs and long MWCNTs) are further commented. Also, the adequacy of spectroscopic techniques (IR and Raman) and of LC-MS to perform lipidomics is discussed.

ATR-FTIR and Raman spectroscopy generate biological spectral fingerprints whereas LC-MS enables the finding of specific biomarkers in omic studies

In this Thesis, the adequacy of both spectroscopic techniques (*i.e.*, IR and Raman) and of mass spectrometry techniques (in particular LC-MS) for the analysis of the samples generated in lipidomic (and metabolomic) studies has been proved (Scientific articles VIII and IX). However, the performance of these analytical techniques concerning sample preparation and data analysis together with the biological information that can be finally extracted from them is different and it is hereby commented.

Regarding sample preparation, the use of ATR-FTIR technique generally requires minimal sample arrangement, compared to LC-MS techniques that necessitate longer sample preparation steps. Such differences are evident when comparing the sample preparation procedures used in this Thesis for ATR-FTIR analysis (Scientific article VIII) respect to SERS and LC-MS analyses (Scientific article IX). Preparation of samples for ATR-FTIR analysis only involved fixation of the cell suspensions with 70% EtOH and placement of the obtained cell pellets on Low-E-reflective glass microscope slides (Scientific article VIII). Moreover, although not performed in this Thesis, it is important to mention that spectroscopic techniques allow the analysis of fresh tissues directly and also live-cell determinations[496]. In contrast, the preparation of samples for LC-MS lipidomic analysis required extensive sample preparation, involving lipid extraction, sample clean-up and resuspension into the solvent phase (Scientific article IX). It is worth-mentioning that basic Raman analysis of all metabolites

in a sample generally requires the same sample preparation used for IR determinations. However, in this Thesis, SERS analysis of lipid extracts was performed and the same extensive sample preparation used for LC-MS analysis was required, with final addition of silver nanoparticles (AgNPs) previous to the analysis. Another significant difference between the spectroscopic (*i.e.*, IR and Raman) *versus* the spectrometric (*i.e.*, MS) techniques is the non-destructive nature of the first ones respect to the latter. While the amount of sample prepared for LC-MS analysis is successively reduced after each injection, thus limiting the number of possible injections, the samples prepared for IR analysis can be reused as many times as desirable.

A common aspect of these analytical techniques is the requirement of multivariate tools for the analysis of the vast amount of data that they generate. Thus, as observed in this Thesis, both the generated data using IR, Raman and LC-MS techniques have been analysed in MATLAB computational environment using multivariate methods such as PCA, LDA, ASCA, among others (Scientific articles VIII and IX). Nevertheless, some differences exist regarding sample pre-processing of data obtained using these different analytical techniques. Pre-processing of IR and Raman data sets is very similar and usually consists on background correction, Amide I peak normalization, noise reduction (and simultaneous resolution of overlapped peaks when performing second differentiation[496]) and shortening the spectra to the biological fingerprint area (*i.e.*, 900-1800 cm^{-1})[497]. Contrarily, the pre-processing steps of LC-MS data sets generally include data compression (*e.g.*, binning, windowing or ROI), chemical data normalization (*e.g.*, correction using surrogates, internal standards and quality controls) or mathematical data normalization (*e.g.*, PQN), and the crucial step of data resolution, necessary to resolve coeluted chromatographic peaks and mass spectra of the sample constituents (for instance by using the ROIMCR procedure or directly the MCR-ALS procedure).

Finally, the information obtained from the analysis of IR, Raman and LC-MS data is also different. Resulting from IR and Raman analyses, information of molecular groups of biological samples is obtained from stretching (v), bending (∂), and symmetric (s) and asymmetric (as) vibrations. Thus, information of lipids ($v_{as}(CH_3)$, $v_{as}(CH_2)$, $v_s(CH_2)$, $v_s(C=O)$ and $\partial_s(CH_2)$), proteins (Amide I and Amide II), nucleic acids ($v_{as}(PO_2^-)$ and $v_s(PO_2^-)$) and carbohydrates ($v_s(CO\text{-}O\text{-}C)$) is generated.

On the other hand, the spectral data generated in the analysis of LC-MS data sets allows a higher degree of information through the elucidation of the molecular formula of potential biomarkers resolved and identified by the ROIMCR or MCR-ALS procedures. Therefore, while all techniques can arrive to the same conclusion (*e.g.*, most significant effects produced by a xenobiotic are found in the lipids), only LC-MS technique enables the identification of the molecular lipid species causing those effects (*e.g.*, significant alterations in TAG species but no relevant effects in PC lipid species). This was evidenced in the study performed in this Thesis of the effects of CBNs on the lipids of brain zebrafish tissue samples (Scientific article IX, Section 4.2.2) using both SERS and LC-MS approaches. In that analysis, both SERS and LC-MS analyses evidenced that SWCNT treatment caused major alterations in the lipids of female brain tissues, showing a discriminant pattern in comparison with the other treatments. However, the analysis of LC-MS data sets allowed going one step further and specifying that SWCNT treatment produced a significant increment in TAG lipid species.

High-dose PFASs are required to significantly alter A6 cells forming domes, due to the enhanced excretion function of these structures

In this Thesis, the effects of PFBS, PFOA, PFOS and PFNA on *Xenopus laevis* A6 Kidney epithelial cells were comparatively studied in cells forming monolayers and in cells differentiated into dome structures by ATR-FTIR spectroscopy followed by chemometric analysis. The interest of culturing cells into dome structures was due to the different physiological and structural properties of cells forming these structures compared to those of cells conforming classical monolayers. As presented in a study of Rehn, M. *et al.*[498], one of the differential structural properties of A6 cells forming dome structures is their unique cytoskeleton. Therefore, in this Thesis, in order to evaluate the effects of the four PFASs on A6 cells depending on the cell differentiation status, the omic experiments were designed to last 2-day to allow cell monolayer conformation (experiment 1) and 9-day to allow dome formation (experiments 2 and 3). Moreover, with the purpose of evaluating the influence of the moment of exposure to the chemicals, cells were exposed to PFASs pre- (experiment 2) and post-dome formation (experiment 3).

Results of the 12 PCA-LDA analyses performed (one per each chemical and type of experiment) evidenced dissimilar dose-response behaviour in experiment 1 respect to experiments 2 and 3. In particular, while major effects were produced at the lowest dose tested (*i.e.*, 10^{-9} M) for all PFAS-treatments in experiment 1, most significant alterations in experiments 2 and 3 occurred at higher doses of the chemicals. A feasible explanation for such distinct effects of PFASs depending on the cell differentiation status might be the enhanced cell excretion function of domes[499], which causes that higher concentrations are necessary to produce an effect. Subsequent evaluation of the overall effects of PFASs on A6 cells obtained in the 12 PCA-LDA models evidenced a higher impact of the chemicals in experiment 3. Interestingly, in this Thesis it was suggested that the larger effects of PFASs in experiment 3 compared to experiment 2 might be due to the capacity of cells to eliminate PFASs under the latter conditions, since cells were allowed to finally grow for 7 days in fresh medium after PFAS-exposure. As reported in a review of Han X. *et al*.[500], renal elimination is the most important process in PFASs toxicokinetics. In that study, the authors proposed a basolateral membrane efflux pathway for PFAS reabsorption in the kidney and evidenced that PFASs renal elimination occurs among PFASs and renal organic anion transport proteins.

ASCA models evidence a link between the two factors underlying the experimental design (*i.e.*, chemical and dose) and the cytotoxicity of PFASs

Furthermore, the results of the three ASCA models, used to elucidate the influence of the two factors underlying the experimental design (*i.e.*, chemical and dose), helped with understanding the differential dose-response effect of PFASs in cells forming monolayers respect to cells forming domes. The scores of the first component of factor "chemical" indicated that the PFASs producing most significant effects on experiments 1, 2 and 3 were PFOS, PFOA and PFBS, respectively. When considering the cytotoxicity of these three chemicals, reported in a previous study[469] (*i.e.*, PFOS the most cytotoxic with an EC_{50} of 107-125 µM, followed by PFOA with an EC_{50} of 594-647 µM and finally PFBS the less cytotoxic) it was evidenced that lower doses were associated to most-cytotoxic PFASs whereas higher doses were linked to less-cytotoxic chemicals. Moreover, the results of the ASCA models regarding the factor "dose" evidenced once more that higher effects in experiment 1 occurred

at the low concentration tested (10^{-9} M), supporting the idea that effects on cells forming domes are produced at higher doses due to the higher excretion function of these structures.

The phenomenon explaining that the higher effects were produced at the lowest dose tested is called the "nonmonotonicity", which means nonlinear relationship between dose and effect. Surprisingly, such phenomenon is quite common in toxicology studies in which most significant alterations are produced at the lowest concentrations tested. In most cases, deviation from linearity (*i.e.*, effect of the toxicant is linearly proportional to its concentration) is generally observed with increasing dose of the toxicant due to saturation and/or inhibition processes.

The examination of the nonmonotonicity behaviour has special relevance in cancer studies since each individual has its own "threshold dose" to switch from "no cancer" to "cancer"; the dose–incidence "curve" represents a staircase of individual threshold doses and reflects the tolerance distribution in the examined population. Extrapolation to low-dose therefore follows differences in individual susceptibility and cannot be simply predicted by the concentration of the toxicant[501].

ATR-FTIR biomolecular fingerprints of A6 cells evidence differential effects of PFASs according to cell differentiation status, moment of exposure and cell population

In this Thesis, a further evaluation of the effects of PFASs on A6 kidney epithelial cells was performed by comparatively studying the biomolecular fingerprint of exposed respect to non-exposed samples. To do that, the primary wavenumbers important for the discrimination between control and exposed samples were determined by PCA-LDA analyses and visualized in cluster vector plots. Interestingly, the spectral alterations induced by PFASs substances insinuated three mechanisms of action of the chemicals determined by the cell differentiation status (*i.e.*, monolayer or dome), the moment of exposure (*i.e.*, pre- or post-dome formation), and cell population.

In experiment 1, all PFASs caused alterations related to DNA/RNA, suggesting a genotoxic insult of the chemicals at these conditions. According to our results, some studies are found in the literature indicating the capacity of some PFASs to produce a genotoxic insult in organisms. For instance, Eke, D. *et al*.[502] evidenced the capacity of PFOS to induce DNA

damage in rat liver. Also, a study performed on six hundred 14-15-year-old Flemish adolescents living in industrial areas, and therefore exposed to PFASs, evidenced the capacity of PFOA to produce short-term (oxidative) damage to DNA[503]. Contrarily to the effects of PFASs produced in experiment 1, the same chemicals caused alterations associated with secondary structures of proteins (Amide I, Amide II, and Amide III). If considering that effects on DNA are finally express in the proteins that it encodes, and that experiment 2 is an elongation in time of experiment 1, the effects of PFASs on proteins are justified. The capacity of PFASs to produce effects on proteins has also been reported in the literature. Jones, P.D. *et al.* evidenced the capacity of PFOS to interfere with hormone/protein interactions in blood and to bind to serum proteins[504]. Also, a study performed in liver and kidney of rats exposed to PFOA evidenced the capacity of this chemical to bind and interfere with cytosolic proteins of these tissues[505].

Finally, in experiment 3 all PFAS substances caused effects related with fatty acids. These results were quite surprising since similar effects to those observed in experiment 1 were expected, since in both conditions cells were analysed right after exposure to the chemicals. Nevertheless, the distinct cell differentiation status (*i.e.*, monolayers versus domes) might be the cause of the differential effects produced under these two experiments. The capacity of PFASs to induce alterations in fatty acids is also reported in the literature. PFOA was proved to induce lipid dysmetabolism in the liver by involving dysregulation of fatty acid trafficking[506]. Also, in *Escherichia coli*, exposure to PFOA caused a reduction of cell membrane fatty acid saturation[507].

In a further step, the effects of the four PFASs in the lipidome of A6 cells were extensively studied, due to the already reported capacity of PFAS to increase levels of the major components of cell membranes (*i.e.*, PC, lyso plasmalogen PC and plasmalogen PC). The results evidenced a significant effect of the chemicals in spectral wavenumbers associated to lipids. In concrete, in experiment 1 PFOS and PFOA produced alterations at 1736 cm^{-1} (C=O stretching lipids) and at 1444 cm^{-1} (lipids), respectively, and in experiment 2 PFBS induced alterations at 1750 cm^{-1}, associated with a C=C stretching in lipids, as happened with cells exposed to PFNA in experiment 3.

PFBS and PFNA behave completely different from PFOS and PFOA, the latter inducing strong cell death in A6 cells

To further assess the effects of the four PFASs on A6 cells, their capacity to induce cell death was studied by a growth-curve experiment. The results of that experiment evidenced a distinct behaviour of cells treated with PFBS/PFNA compared to those exposed to PFOS/PFOA. While PFBS/PFNA did not produce significant A6 cell proliferation or depletion respect to the controls, PFOS and PFOA caused a diminution in A6 cell population. Such cell depletion produced by PFOS and PFOA followed a particular trend: after 48 h of exposure, a moment when the two chemicals showed maximum effects, high-dose PFOS caused larger cell decreases, while low-dose PFOA was responsible for highest diminution in cell number. These results are in agreement with other studies in the literature that demonstrate the capacity of PFOS and PFOA to inhibit cell proliferation. For instance, a study of Liu, C. *et al.* evidenced the ability of these two PFASs to produce oxidative stress and induce apoptosis with involvement of caspases in primary cultured tilapia hepatocytes[508].

CBNs induce marked lipid alterations in brain, gonads and gastrointestinal tissue samples of zebrafish

As previously stated, in this Thesis A6 kidney epithelial cells were used to simulate effects of PFASs on amphibians. In order to simulate the omic effects of chemicals on fish, the model organism zebrafish (*Danio rerio*) was utilized. In particular, this model organism was used to study the effects of four CBNs (*i.e.*, C_{60}, SWCNT, short MWCNTs and long MWCNTs) in brain (to assess developmental alterations), gonads (to assess reproductive alterations) and intestinal tracts (to assess point-of-contact alterations) of male and female zebrafish. In all cases, the lipids of these samples were extracted and further analysed by LC-MS and brain tissues were also analysed with SERS spectroscopy.

In the first exploratory PCA analysis, six components were selected to build the model, explaining a cumulative variance of 78.02%. Resulting from this analysis, three major sources of variation were attributed to the original data, corresponding to the three target tissues: brain, gonads and intestinal tracts, indicating differential effects of CBNs on the distinct tissues. Moreover, extensive evaluation of the LC-MS lipid profiles of male and female

zebrafish allowed extracting conclusions of the effects of CBNs in the distinct tissues examined. First, LC-MS lipid profiles of male brain tissues indicated a profound effect of long MWCNTs and SWCNTs, both causing an increase in TAG and PC lipid species, while a smaller effect of C_{60} and short MWCNTs, which showed a similar pattern causing a decrease on the abundance of TAG and PC lipid species. These alterations produced in lipid profiles are represented in FIGURE 4.6, modified from a figure published in Scientific article IX.

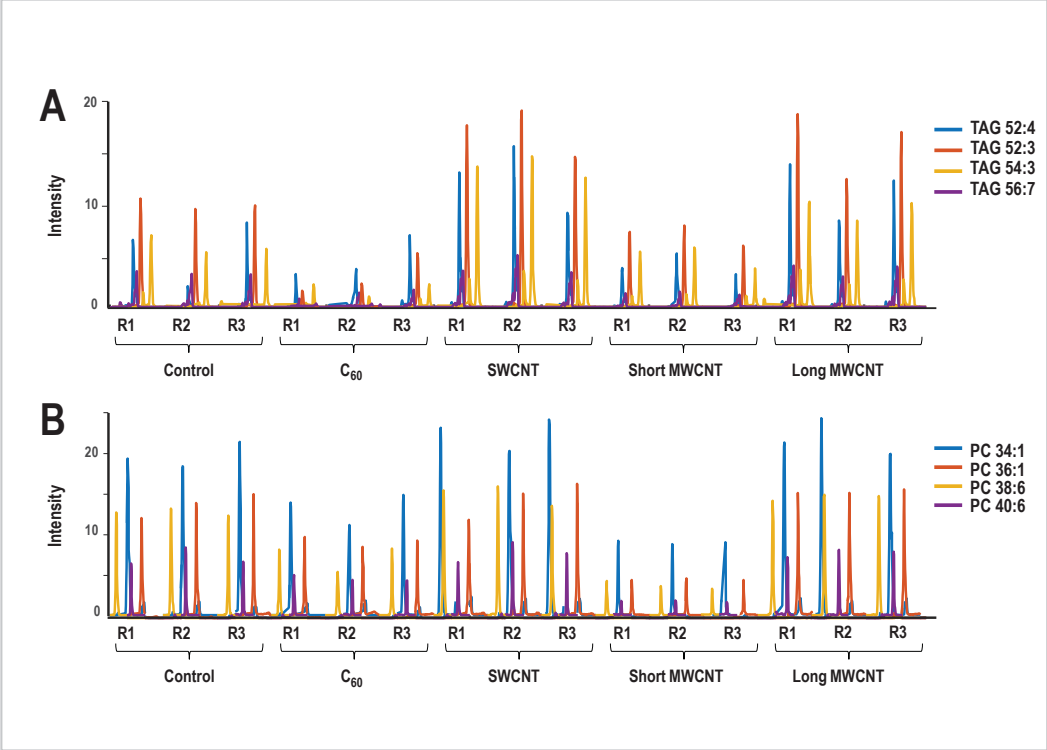

FIGURE 4.6

LC-MS elution profiles resolved using ROIMCR procedure of some representative TAG (A) and PC (B) lipid species from male brain tissue samples exposed to CBNs. (R: replicate, 1 to 3: replicate number). *The results represented in this Figure are published in the Scientific article IX, Section 4.2.2.*

Contrarily, both SERS and LC-MS approaches confirmed a spectacular effect of SWCNT treatment in female brain tissues compared to the other CBNs. Such discriminant effect of SWCNTs was mainly associated with an increase in the amount of TAG lipid species, as represented in FIGURE 4.7, modified from a figure published in Scientific article IX.

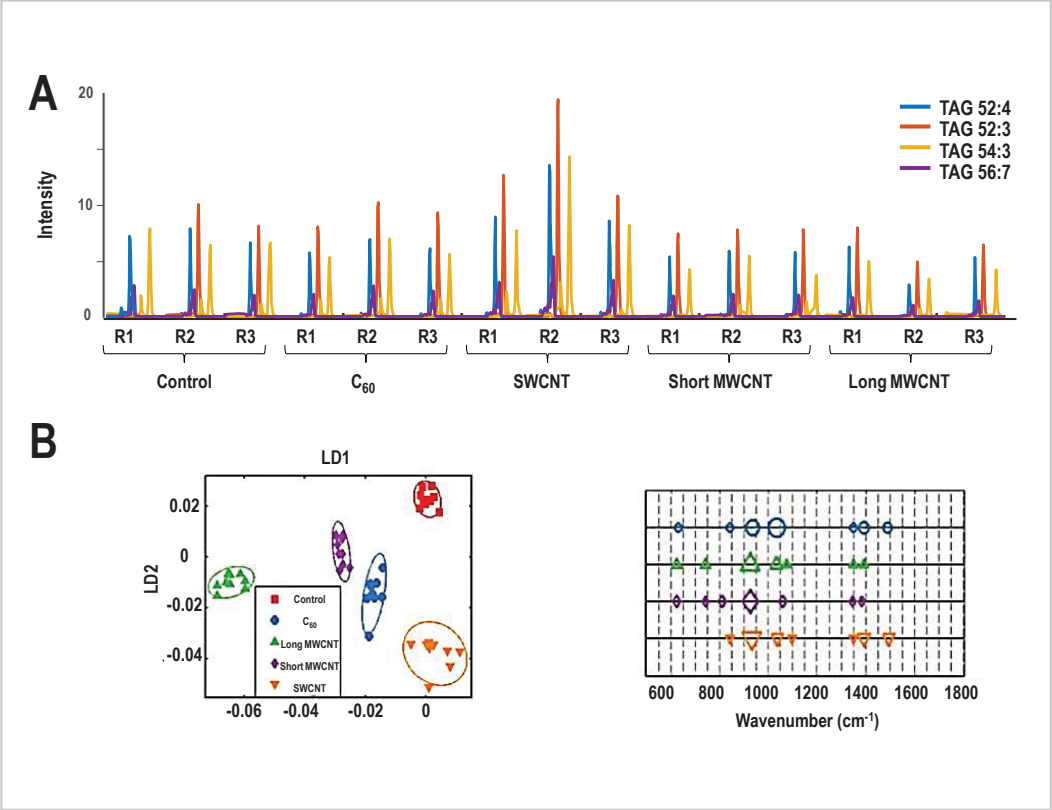

FIGURE 4.7

Effects on lipids of brain female tissues of zebrafish. A) LC-MS elution profiles resolved using ROIMCR procedure of some representative TAG lipid species of female brain tissue samples exposed to CBNs. (R: replicate, 1 to 3: replicate number). B) PCA scores plot (left panel) and cluster vector plot (right panel) resulting from SERS analysis. In scores plot the different clusters represent control (red squares), C60 fullerene-treated (blue diamond), long MWCNT-treated (green triangle), short MWCNT-treated (purple diamond) and SWCNT (inverted orange triangle). Cluster vectors plots indicate the top distinguishing wavenumbers associated with each CBN treatment compared with the control; symbol size is proportional to strength of alteration. *The results represented in this Figure are published in the Scientific article IX, Section 4.2.2.*

Membrane lipids of zebrafish samples response against the oxidation damage induced by CBNs

A search in the literature of the effects that CBNs can pose on organisms evidences a capacity of these chemicals to interact and alter membrane lipids. In fact, fullerene molecules can enter the cell membrane and occupy its hydrophobic region. Moreover, a study of Sastre J.

et al.[509] evidenced the capacity of fullerene particles to modify the structural properties of lipid membranes like thickness, area and internal ordering of the lipid species, as well as dynamical aspects such as molecular diffusion and cholesterol flip-flop. Other examples of studies that have demonstrated the capacity of CBNs to induce alterations in lipid membranes suggest their capacity to induce membrane peroxidation leading to the alteration of membrane permeability[510,511]. Similarly to these findings, in this Thesis some effects of CBNs on membrane lipids of male and female zebrafish have been observed. Among them, an important increase of PC species and derivatives was found on brain male samples exposed to SWCNTs or long MWCNTs, on gonad male samples exposed to long MWCNTs and on gastrointestinal female samples exposed to C_{60} or SWCNTs. A reason for such increment can be a defence mechanism of cellular membranes against the oxidative stress caused by CBNs, since some evidences link effects on membrane lipids and the generation of ROS[510].

Regarding the effects that CBNs may have on TAG and DAG species (the major constituents of lipid droplets), few evidences exist in the literature until now. For instance, a study of Cao Y. *et al.* evidenced that nano-sized carbon black (exposure) induced lipid accumulation in THP-1a cells[512]. Nevertheless, in this Thesis it was evidenced the capacity of CBNs to alter TAG and DAG species, both in brain, gonad and gastrointestinal tissue samples of zebrafish.

CBNs produce elevations in global genomic methylation, especially in female zebrafish tissue samples

Finally, in this Thesis, the capacity of CBNs to alter the levels of genomic methylation was assessed. The results evidenced a consistent increase in levels of genomic methylation, especially after exposure with SWCNTs. Moreover, if considering the high persistence of CBNs, long-term exposure to these chemicals would probably lead to alterations that could affect development. Similar findings of CBN capacity to induce DNA methylation were found in a study performed with A549 lung cells exposed to C_{60}, long and short MWCNTs and SWCNTs. In that study, it was evidenced for the first time the capacity of real-world levels of nanoparticles to alter the methylome of exposed cells, this having enormous implications for their regulatory assessment[513].

PFASs differential response in the presence of CBNs opens a new and little explored research line based on co-exposure studies

Both PFASs and CBNs are widely distributed contaminants highly present in the environment and there is a considerable concern regarding their ecotoxicity. CBNs interact with PFOS in water and result in different impacts compared with those after single exposures. In this Thesis, the effects of PFASs and of CBNs have been assessed separately (Scientific articles VIII and IX). However, due to the reported evidence of the interaction of CBNs with PFASs, the assessment of their simultaneous effects should be performed in order to assess co-exposure to these xenobiotics. In fact, some recent studies have already started working in that direction. For instance, Li Y. *et al.*[514] have recently evaluated the effect of SWCNTs on bioconcentration and toxicity of PFOS in zebrafish. The results of that study evidenced that the bioaccumulation of PFOS in fish tissues (liver, intestines, gills and brain) decreased with increasing dosage of SWCNT, whereas the opposite trend was found in fish skin, which indicated that the bioavailability of PFOS changed by adsorption on SWCNT. Also, co-exposure induced more ROS than PFOS alone and enhanced the effect of PFOS on the superoxide dismutase, and catalase and AChE activities[514]. Interestingly, this is not the unique study found in the literature that evaluates the differential response of PFASs in the presence of CBNs. Similarly to the previous study mentioned, the authors Wang S. *et al.* found that the presence of MWCNTs reduced the developmental toxicity of PFOS in early life stage (from 3 h post fertilization) of zebrafish[407].

Considering all this, a potential future research line to initiate after the finalization of this Thesis would consist on the evaluation of the co-exposure effects of PFASs and CBNs, two common and widely distributed environmental pollutants.

4.4. CONCLUSIONS

From the scientific research included in this Chapter, the following specific conclusions can be extracted:

Concerning the performance of ATR-FTIR, Raman spectroscopy and mass spectrometry in metabolomic (and lipidomic) studies,

- In this Thesis, the adequacy of both spectroscopic techniques (*i.e.*, IR and Raman) and mass spectrometry techniques (in particular LC-MS) for the analysis of samples generated in metabolomic (and lipidomic) studies is proven.
- It is demonstrated that ATR-FTIR and Raman spectroscopies generally require minimal sample arrangement, compared to LC-MS techniques that necessitate extensive sample preparation (*e.g.*, addition of surrogates and internal standards, preparation of quality control samples). Moreover, the non-destructive nature of the two spectroscopic techniques (*i.e.*, IR and Raman) is proved.
- Regarding the analyses of IR, Raman and LC-MS data sets, in this Thesis it is confirmed that all of them are enhanced by the use of multivariate chemometric tools, due to the vast amount of information that the data sets contain. However, some differences exist concerning data pre-processing steps, since IR and Raman data sets usually require background correction, Amide I normalization, noise reduction and shortening of the spectra into the fingerprint area, while the pre-processing steps of LC-MS data sets generally include data compression, data normalization and resolution.
- Concerning the biological information that can be obtained when using these techniques, it is proved that IR and Raman provide global information of molecular groups of samples (*i.e.*, lipids, proteins, nucleic acids and carbohydrates) whereas LC-MS allows a higher degree of structural information and identification through the elucidation of the molecular formula of potential biomarkers.

Concerning the study of the effects of PFASs on the *Xenopus laevis* A6 kidney epithelial cell line,

- The study the effects of four PFASs (*i.e.*, PFBS, PFOA, PFOS and PFNA) on A6 cells in two physiological status (*i.e.*, monolayers or domes) under an experimental design that

2.4. CONCLUSIONS

From the scientific research included in this chapter, the following specific conclusions can be extracted:

Concerning the adequacy of *Chemometrics* to analyse metabolomic (and lipidomic) data generated by different analytical techniques,

- The use of multivariate data analysis methods has proved to enable the comprehensive analysis of the large complex megavariate data sets (often with incomplete, noisy and non-linear and collinear data structures) generated in metabolomic (and lipidomic) studies.
- Chemometric tools have shown to facilitate the shift from the concept of studying one chemical compound or process at a time to the more comprehensive concept of characterizing the whole biological systems in a single experiment.
- Chemometric tools have proved to be adequate to cover the distinct steps in data analysis, mainly consisting on data pre-processing and pre-treatment, exploratory data analysis by projection methods (*e.g.*, PCA), feature/biomarker detection (*e.g.* PLS-DA), data profiling and resolution by MCR-ALS methods and variance source exploration through the combination of classical ANOVA with multivariate methodologies (*i.e.*, ASCA).

Concerning targeted *vs* untargeted metabolomic (and lipidomic) LC-MS analytical approaches,

- Targeted metabolomic (and lipidomic) approaches only allow the study of a predefined group of metabolites (and lipids) contained in a referential database, which needs to be previously elaborated, whereas untargeted approaches enable extensive analysis of entire metabolomic (and lipidomic) profiles.
- Untargeted approaches involve complex data analysis (including data compression and resolution) since entire data sets (containing massive amount of MS-rich information) need to be processed. However, such analyses can be facilitated with the use of

multivariate chemometric tools. Targeted approaches are generally performed using classical statistical tools and they are usually more tedious and time-consuming.

Concerning the untargeted chemometric methodology for the analysis of LC-MS data sets developed in this Thesis,

- Data conversion of LC-MS files from vendor formats to open data formats (*e.g.*, text or mzXML formats) is required to analyse the data outside the software of the vendor. Among the different ways that exist for data conversion, the external software *ProteoWizard* has showed to enable the conversion of any type of vendor format.
- Compression of LC-MS data sets is necessary to reduce the vast amount of information into more computationally manageable formats and avoid problems related to the limited memory capacity of the computers. Among the distinct data compression strategies (*e.g.*, binning, windowing and ROI), the search of ROIs is proved to be very suitable for the compression (together with data matrix construction) of LC-MS data sets, due to the fact that no loss of spectral accuracy is derived from a ROI compression.
- Three parameters are required to perform a ROI search: signal-to-noise ratio threshold, mass admissible error and minimum number of occurrences. It is proved that the optimum threshold value should be adjusted between 0.1- 1% maximum MS measured intensity. The optimum mass deviation value should be selected halfway between an excessive and an insufficient mass accuracy and should be specifically adjusted for the type of mass spectrometer used. The optimum minimum number of occurrences should be adjusted according to the type of chromatography (*i.e.*, HPLC *vs.* UHPLC) and the corresponding width of the chromatographic peak.
- The developed ROI compression strategy for more than one sample is adapted to augmented data matrices containing relevant information of compressed data of more than one sample (*e.g.*, control and treated samples). In this way the comparison of the peak areas of the resolved elution profiles of the same metabolite in different samples can be performed. Moreover, the pure spectra resolved for the components are more reliable.

- MCR-ALS has shown to be a powerful chemometric method to perform LC-MS data resolution, mainly providing four advantages: i) the possibility of immediate chemical identification of the metabolites thanks to the MS information provided in the analysis; ii) the high degree of direct interpretability of the results; iii) the flexibility in the structure and nature of the data sets that can be potentially analyzed and iv) the added value of not requiring peak shaping nor chromatographic alignment for the simultaneous analysis of multiple samples.
- Among the different feature detection tools, in this Thesis it is demonstrated the adequacy of one-way ANOVA followed by a multiple comparisons test and of PLS-DA analysis through the determination of variables importance for projection (VIPs) for the detection of potential biomarkers for metabolite (and lipid) disruption.

Concerning the identification of potential biomarkers,

- In this Thesis it is demonstrated that proper identification of potential biomarkers requires having precise information about *m/z* values at high resolution. Moreover, it is evidenced that such information is achieved when performing data compression based on the search of ROIs, but it is lost when performing other types of compression, such as binning.
- Recovery of mass at high resolution from low-resolution compressed data can follow two strategies. First strategy consists on extracting MCR-ALS spectra profiles at high resolution (*i.e.*, $\mathbf{S}^T_{HR}$) by a (least-squares) pseudo-inversion of estimated concentration profiles at low resolution ($\mathbf{C}^*$) and LC-MS data at high resolution ($\mathbf{S}^T_{HR}=\mathbf{C}^*\backslash\mathbf{D}_{HR}$). Second strategy consists on using information of MCR-ALS spectra profiles at low resolution to find out the accurate mass when searching in the raw experimental chromatogram (measured at the highest resolution of the instrument), obtaining the isolated ion of interest and further calculating the elemental composition.
- The mode of acquisition of MS data (*i.e.*, profile *versus* centroid) has been proved to have an influence on final identification of metabolites, providing the latter continuous and extensive information of MS spectra profiles. More work is needed to take advantage of this mode.

- Distinct software exist to perform elemental composition determination. Among them, the elemental composition tool provided in the Masslynx software of WATERS corporation, and the software specifically developed for the identification of profile MS data, named MassWorks, have proved to be adequate to perform metabolite (and lipid) identification. Both software (*i.e.*, Masslynx and MassWorks) tools perform the elemental composition search based on the comparative isotopic distribution of the measured ion and that of a theoretical candidate, using the parameters i-FIT and spectral accuracy, respectively. This has been proven in this Thesis in the identification of some lipid species of human placental choriocarcinoma JEG-3 cells, analysed with a Waters/LCT Premier XE TOF analyser.